PhD Thesis

Electron Correlation Effects in Laser-Atom Interactions

M. Makris

University of Crete

Department of Physics

2004

PhD Thesis

Electron Correlation Effects in Laser-Atom Interactions

Thesis author: M. Makris

Thesis supervisor: Prof. P. Lambropoulos

Thesis committee:

P. Lambropoulos — Thesis supervisor

N. Kylafis — Member

T. N. Tomaras — Member

P. Rakintzis — Member

G. P. Tsironis — Member

S. Farantos — Member

D. Charalambidis — Member

Physics Department - University of Crete
Heraklion - Crete

September - 2004

Contents

CHAPTER 1

INTRODUCTION

Current laser systems are capable of developing field strengths comparable to (or greater than) the binding energy of the electron to an atom or molecule. The nonlinear response of the atom on such lasers leads to (among others) the generation of high-order harmonics (HOHG). The superposition of these harmonics has been proposed as an avenue towards ultra-short pulse, which ,when available, will be the fastest probe of light-matter interactions. Although this approach has a significant advantage, i.e. table top setup, there are problems one has to surmount. The temporal characteristics of this superposition are not an easy task to extract. A blind superposition of harmonics will result on loss of all short-time structure of the field. Thus it is vital to have as much information as possible for the harmonics.

In this direction, we used the single active electron approach (SAE), which is widely employed in the study of HOHG from atoms, to explore a method that can be used to indirectly provide the temporal profile of this superposition. This simplification allows the handling of the full time dependent Schrödinger equation, without any further approximations.

The next level of complexity are phenomena where there are more electrons, i.e two, involved in the dynamics of the system. The two-electron atom holds a special place in atomic physics, since it provides the testing ground for the three-body problem. Among the "two-electron" atoms, Helium is the model atom with long range coulomb forces and without the additional complication of a core found in the alkaline earths.

The theoretical framework for the structure of two-electron atoms is built on some zeroth order single electron orbitals, which are then employed in the construction of two-electron states, where the notion of electron correlation (the effect of electron-electron interaction) is inevitably involved. In the discussion of two-electron atoms in strong laser fields, the issue of correlation assumes an equally important role to that of the laser field. With an intense enough source, we can reach states of angular momenta inaccessible to one-photon absorption, which provides extended testing ground for theoretical models of atomic structure. The intensity of the radiation matters only in inducing a higher order transition, and should not be such as to seriously distort the atom. The transition amplitude of the appropriate order, in lowest (non-vanishing) order perturbation theory (LOPT), is what is required for the theoretical description. The latter is the approach we will follow for the two-photon double ionization of He, in the range of 45 eV, a phenomenon which should be observable employing the short-wavelength free electron lasers sources.

This thesis is organized as follows. In the second chapter we present the necessary tools employed to describe a one- and two- electron atom. We show how a discrete basis, formed in terms of B-splines, is used for representing the bound states, the one-electron and the two-electron continuum states. A short discussion about the laser-atom interaction is included together with some remarks for the appropriate gauge selection for this interaction.

This is followed by a presentation of a novel computational technique, developed to provide the equivalent to absorbing boundaries, used in different approaches, for the case of the time-dependent Schrödinger (TDSE) equation formulated on the eigenstates of the field-free atom. We also propose a suitable generalization able to provide absorbing boundaries for all methods involving a discretized energy continuum, based on the spectrum of the discretized states.

The fourth chapter is devoted to the study of the phase characterization of harmonics. The results we obtain are based on the solution of the TDSE for Hydrogen. We examine the interference of the harmonics with the fundamental that produced them and by varying their relative delay, we obtain information about the phase profile of the harmonics. We show where this information is adequate to represent the phase profile of the harmonic.

Finally, the fifth chapter includes our results for the electron angular distribution in the two-photon double ionization of helium in the range of 45 eV. Using lowest order perturbation theory and an approach that allows us to explore the role of correlation, we obtain conditions under which the two electrons have the tendency to be emmited in the same direction.

CHAPTER 2

ATOMIC STRUCTURE

2.1 Atoms and B-splines

2.1.1 Introduction

A primary task of atomic theory is the solution of the Schrödinger equation or its relativistic generalization for atoms and ions. The use of basis sets in the effort to solve the Schrödinger equation has a long history in physics. The basic advantage is that it transforms the solution of a differential equation into an algebraic eigenvalue problem. Of course the later is based on numerical computations of linear algebra, which is one of the best developed areas in modern programming. On the other hand, there are finite-difference methods, where a numerical wavefunction is determined at a limited number of mesh points.

The finite-difference and the basis set methods can be characterized as 'local' and 'global' methods respectively. In local methods the solution depends only on the neighboring points. This means that an initial estimate is necessary to start the algorithm. For global methods the solution at one point is connected to the complete solution making thus an initial estimate unnecessary.

In addition to B-splines, there is a wide variety of finite basis sets used in computational atomic physics, including Gaussian and Slater functions. Nevertheless, the latter present some important difficulties. For example,

Slater type orbital (STO) basis sets require a nonlinear optimization, which is a procces difficult to control. Also the latter basis sets have to be large in order to be complete enough for the solution we seek. Ussualy, linear dependencies effectively restrict the size of the basis

B-splines can form a basis that is complete enough with a relatively small number of basis functions. Also they have a number of advantages making them particularly useful. In their case, linear dependencies are negligible and the matrices one has to diagonalise, as will be shown in more detail in the following, are banded. The latter allows the usage of large basis sets. Another advantage is the inherent flexibility they offer to choose the radial grid points between which the B-splines are defined.

In this chapter, we will show the utility of finite basis sets constructed from piecewise polynomials known as B-splines [1] in solving the Schrödinger equation for one- and two- electron atom.

The first use of splines in atomic physics was made by Shore [2] about 30 years ago. They are used with increasing frequency in the last 15 years or so, and they have proved to be a very valuable tool. We mention the review article by Sapirstein and Johnson ([3]) and [4].

2.1.2 Definition of B-splines

The basis we will use in the following is a set of n B-splines of order k. Following deBoor [1], we divide the interval $[0, R]$, where we want to calculate the atomic eigenstate, into segments, the endpoints of these segments being the knot sequence $\{t_i\}, i = 1, 2, \ldots, n + k$. The B-splines of order k, $B_{i,k}(r)$ are defined recursively by the relations

$$B_{i,k} = \begin{cases} 1 & , t_i \leq r < t_{i+1} \\ 0 & , \text{otherwise} \end{cases} ,$$

and

$$B_{i,k}(r) = \frac{r - t_i}{t_{i+k-1} - t_i} B_{i,k-1}(r) + \frac{t_{i+k} - r}{t_{i+k} - t_{i+1}} 1 B_{i+1,k-1}(r) \qquad (2.1)$$

The function $B_{i,k}(r)$ is a polynomial of degree $k - 1$ inside the interval $t_i \leq r < t_{i+1}$ and vanishes outside this interval. The knots defining our grid have k-fold multiplicity at the endpoints 0 and R; i.e. $t_1 = t_2 = \ldots = t_k = 0$

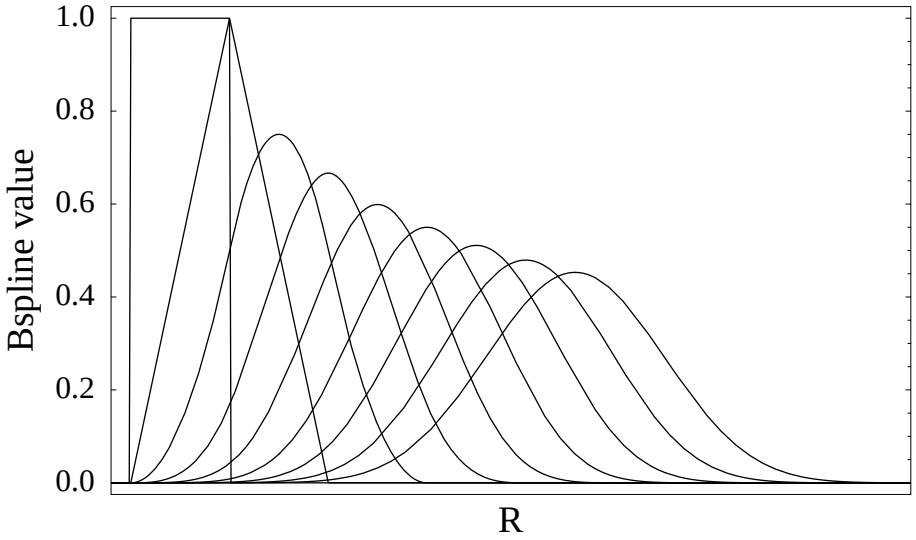

Figure 2.1: B-spline of various orders on a linear knot sequence. Starting from $k = 1$ (left) and ending at $k = 9$ at right. The B-splines were shifted to become more visible.

and $t_{n+1} = t_{n+2} = \ldots = t_{n+k} = R$. When multiple knots are encountered, limiting forms of the recursive definition of the B-splines must be used. For $k > 1$, the B-splines generally vanish at the endpoints: however, at $r = 0$ the first B-spline is equal to 1 (with all others vanishing) and at $r = R$ the same is valid for the last B-spline. This will facilitate the implementation of boundary conditions later on.

For simple equidistant knots, each B_i is just a translation by one interval of the previous one. If the knots are not equidistant, there is a smooth change in shape. Also, because the B-splines are positive functions with a minimal support, the expansion coefficients of an arbitrary function are close to the function values at the knots. This implies that large oscillations of the coefficients are avoided, so numerical errors originating from cancellations are minimal, in contrast to the case of other bases such as STO's.

The knot sequence can be arbitrary, but usually the type of problem plays a decisive role in the form of the sequence. A suitable knot sequence makes calculations feasible, faster and more accurate. For example if one intends to describe a bound state, where most of the variations of the wave-function take place at a domain in space close to origin, it is logical to use a knot distribution more dense close to the origin and provide this way more basis

functions where they are more necessary. On the other hand, the description of a continuum state, which is not limited in space, requires a practically uniform grid distribution able to represent the oscillatory nature of the wave-function. In practice, B-splines of a typical range $k = 6 - 11$ are used in atomic physics.

The main advantage of B-splines, compared to global bases, is that the error introduced in the description of a function is directly controlable by the knot density, in analogy to finite-difference methods, and at the same time they retain all advantages associated with basis set expansions. In the case of atomic physics, since the eigenstates of the Schrödinger equation are smooth oscilating functions, the finite basis used is appropriate as long as the oscillations are longer than the knot density. More details on this issue in the following section.

2.1.3 Single electron atom

We now wish to apply spline basis to the solution of the radial Schrödinger equation. The radial Schrödinger wave-function $P_{nl}(r)$ defined through $\phi_{nlm} = \frac{P_{nl}(r)}{r} Y_{lm}(\theta, \phi)$ satisfies the equation

$$\left[-\frac{1}{2}\left(\frac{d^2}{dr^2} - \frac{l(l+1)}{r^2}\right) - \frac{Z}{r} \right] P_{nl}(r) = \epsilon_{nl} P_{nl}(r), \tag{2.2}$$

where we use atomic units and work with the potential of a point nucleus of charge Z. Rather than work with the radial Schrödinger equation directly, we instead work with the equivalent variational equation $\delta S = 0$, where

$$S = \frac{1}{2}\int_0^R dr \left[\frac{1}{2}\left(\frac{dP_l}{dr}\right)^2 + \left(-\frac{Z}{r} + \frac{l(l+1)}{2r^2}\right) P_l(2)^2 \right] - \frac{1}{2}\epsilon \int_0^R dr P_l(2)^2 \tag{2.3}$$

with ϵ playing the role of a Lagrange multiplier introduced to ensure that the normalization constraint

$$\int_0^R dr P_l(r)^2 = 1 \tag{2.4}$$

is satisfied. The variational principle $\delta S = 0$, together with the constraints $\delta P_l(0) = 0$ and $\delta P_l(R) = 0$, leads to the radial Schrödinger equation for $P_l(r)$.

We now introduce the spline basis set by expanding $P_l(R)$ in terms of B-splines of order k as

$$P_l(r) = \sum_{i=2}^{n-1} p_i B_i(r). \tag{2.5}$$

The subscript k has been ommited from $B_{i,k}(r)$ for notational simplicity. The boundary conditions have been implemented by restricting the above summation not to include $B_1(r)$ and $B_n(r)$, which are the only basis functions that do not vanish at $r = 0$ and $r = R$ respectively.

The action S becomes a quadratic function of the expansion coefficients p_i when the expansions are substituted into the action integral. The variational principle then leads to a system of linear equations for the expansion coefficients,

$$\frac{\partial S}{\partial p_i} = 0, i = 2, \ldots, n-1. \tag{2.6}$$

The resulting equations are written in the form of a $n-2 \times n-2$ eigenvalue equation

$$A\upsilon = \epsilon B\upsilon, \tag{2.7}$$

where υ is the vector of expansion coefficients

$$\upsilon = (p_2, p_3, \ldots, p_{n-1}) \tag{2.8}$$

the matrices A and B are given by

$$A_{ij} = \int_0^R \{\frac{1}{2}\frac{dB_i}{dr}\frac{dB_j}{dr} + B_i(r)(-\frac{Z}{r}) + \frac{l(l+1)}{2r^2})B_j(r)\}dr, \tag{2.9}$$

$$B_{ij} = \int_0^R B_i(r)B_j(r)dr, \tag{2.10}$$

Because the product $B_i(r)B_j(r)$ is not zero only when i and j differ by k or less, the matrices A and B are sparse, diagonally dominant banded matrices. Also, since B-splines are polynomials, a Gaussian integration of order $2k$ allows the evaluation of the matrix elements of A and B to machine accuracy in the case of a point Coulomb potential. For non-Coulomb potentials, an interpolation must be used to calculate part of A, but the error introduced is insignificant.

Solving the generalized eigenvalue equation, one obtains $n-2$ real eigenvalues ϵ^λ and $n-2$ eigenvectors v^λ. The eigenvectors satisfy the orthogonality relations

$$\sum_{i,j} v_i^\lambda B_{ij} v_j^\mu = \delta_{\lambda\mu} \tag{2.11}$$

which leads to the orthogonality relations

$$\int_0^R P_l^\lambda(r) P_l^\mu(r) = \delta_{\lambda\mu} \tag{2.12}$$

for the corresponding radial wave-functions.

These $n-2$ eigenenergies, as a result of a variational method, correspond to the upper bound of the first $n-2$ exact eigenenergies of the system. The difference between the calculated and the real eigenstates/eigenenergies can be seen as a direct consequence of the finite size of the basis, both in space and in the number of B-splines (in this case). This difference depends on the extent the eigenfunctions are subject to the limitations following the finite size of the basis.

The first few eigenvalues (with $\epsilon_n < 0$) and eigenvectors in the box agree precisely with the first few bound state eigenvalues and eigenvectors obtained by numerically integrating the radial Schrödinger equations, or even an analytical solution, but as the principal quantum number increases the spectrum departs more and more from the real spectrum. Since the atom is confined inside a sphere of radius R and as long as the eigenfunction is limited in a smaller region, this eigenstate is not "aware" of the boundaries, so it is in agreement with the actual eigenstate of the system. Rydberg states reaching or surpassing the size of the sphere (their extent scales as $\langle r_{nl} \rangle = \frac{1}{2}[3n^2 - l(l+1)]$ for hydrogen) are not correctly described, or even absent.

The next eigenstates, with positive eigenenergy, represent the continuum part of the spectrum. Formally, the solutions of the Schrödinger equation for positive energy appear as a family of eigenfunctions depending on the continuous parameter ϵ. In our approach the diagonalization provides a discrete set of eigenstates, due to the fact that we have restricted the problem in a finite part of the space. Nevertheless these functions can be used as a representation of the true continuum with a different normalization, as is explained in more detail in the following.

For the continuum eigenstates, the finite basis is not adequate for the last (highest in energy) discrete states. These eigenstates oscillate fast (equivalently they have high kinetic energy) and the density of B-splines is not high enough to describe them. The density of B-splines has to be carefully selected in order to ensure a good description of the continuum eigenstates up to the desirable energy.

Free boundary conditions

The fixed boundary condition (FBC) method we have described selects by construction the eigenstates in the continuum that satisfy the condition $P_l(r = R) = 0$. For different angular momenta l of the electron the resulting energy spectrum is different. Although for bound states this generates no problems, since they are true discrete states, for the continuum states this results to a lack of the inherent degeneracy of the spectrum. Of course in the case the spectrum is dense enough (large R) this deficiency of the FBC is either unimportant or can be circumvented by simple methods (i.e. interpolation of the energy spectrum).

A straightforward generalization is possible for the treatment of a two-electron atom in a strong laser field, as long as the final state of the atom involves single-channel excitations ([5, 6]).In the case though, that the final state of the atom is such that many atomic excitation or ionization channels are available, the FBC method is not suitable since the degeneracy in the final state has a vital role and cannot be easily incorporated in a systematic way [7]. In view of these demands, we will briefly discuss a method that allows one to choose the (discretized) energy spectrum in the continuum [8].

Going one step back, we do not use the boundary condition $P(r = R) = 0$, so the continuous part of the spectrum will not be a result of a variational approach, but rather the solution of the equation

$$\mathbf{A}\upsilon = (\mathbf{h} - \epsilon\mathbf{B})\upsilon = 0 \tag{2.13}$$

with $\mathbf{B}$ the overlap matrix again, ϵ the energy of our choice for which we seek the eigenstate and $\mathbf{h}$ the one electron hamiltonian matrix defined by:

$$\mathbf{h}_{ij} = \langle B_i | h(r, l) | B_j \rangle, \tag{2.14}$$

$$h(r,l) = -\frac{1}{2}\frac{d^2}{dr^2} - \frac{l(l+1)}{2r^2} + V_l(r).$$

The hamiltonian is not hermitian due to the surface term. This is due to the fact that neither the last B-spline nor its derivative nor the second-last B-spline vanish at the end point, which causes the differential operator to be non-symmetric. Using the Bloch operator [9], it is possible to write a new hermitian hamiltonian $\hat{\mathbf{h}}_{\mathbf{ij}} = h_{ij} - \delta_{i,n-1}\delta_{j,n}c_0$ and the continuum eigenstates come from the solution of:

$$(\hat{\mathbf{h}} - \epsilon_i \mathbf{B}) \cdot \mathbf{c_i} = c_0 \tag{2.15}$$

and c_0 is a vector with one non-zero element, to which an arbitrary value is assigned. As long as $(\hat{\mathbf{h}} - \epsilon_i \mathbf{B})$ is not singular, the solution is simply calculated as:

$$\mathbf{c_i} = (\hat{\mathbf{h}} - \epsilon_i \mathbf{B})^{-1}\mathbf{c_0}. \tag{2.16}$$

What remains is the correct normalization of these eigenstates which is discussed for both the cases of free and fixed boundary conditions in the following.

Normalization of continuum eigenstates

The solution of the Schrödinger equation for the atom inside a box instead of the full space limits the eigenfuctions in an artificial way. This is also reflects in their normalization. Although for bound states this is a minor problem, since they are normalized to unit, for the eigenstates belonging to the continuum one has to be more careful.

In general the eigenstates of the atom should be normalized as follows:

$$\langle \phi_m | \phi_n \rangle = \begin{cases} \delta_{mn} & \text{, m,n bound states} \\ \delta(\epsilon_m - \epsilon_n) & \text{, m,n continuum states} \end{cases},$$

and bound states are those with $\epsilon_m \leq 0$.

In the descritized basis we use, the continuum is represented by a set of discrete L^2-integrable wavefunctions [10]. Since the discrete states have different normalization, we have to obtain an effective density of states ρ

so that the continuum eigenfunction $\psi_c(\epsilon_n)$ is related to the discrete state $\psi_n(\epsilon_n)$ at the same energy through

$$\psi_c(\epsilon_n) = \sqrt{\rho(\epsilon_n)}\psi_n(\epsilon_n). \tag{2.17}$$

Assuming that the state density is sufficiently high, the simplest way [11, 12] to approximate ρ is through

$$\rho(\epsilon_n) \cong \frac{\Delta n}{\Delta \epsilon} = \frac{2}{\epsilon_{n+1} - \epsilon_{n-1}} \tag{2.18}$$

An alternative way to obtain the correct normalization is to match at some large r the discrete wavefunction to the asymptotic form

$$\psi_K(r) \sim A\left(\frac{K}{\zeta(r)}\right)^{1/2} sin[\phi(r) + \delta_l] \tag{2.19}$$

where the functions $\phi(r)$ and $\zeta(r)$ are such that for $r \to \infty$, $\zeta(r) \to K$ and $\phi \to [Kr + (q/K)ln(2Kr) - (l\pi/2) + \delta_c]$ with q being the effective charge experienced by the electron in the continuum and δ_c the assymptotic phase shift against the "free Coulomb wave". Thus for sufficiently large r the functional form of the expression is known and A is determined through the matching to $\psi_n(r)$. The effective density of states in this case is just $2/\pi K A^2$.

2.2 Interaction with intense laser fields

The lasers routinely employed in present day laboratories deliver fields whose strength can exceed the Coulomb electric field of the atom. As a consequence, during its interaction with the atomic system, the external laser field can no longer be considered as a perturbation to the internal field. The range of intensities between roughly $10^{12} W/cm^2$ (upper limit of perturbation theory) and $10^{17} W/cm^2$ (lower limit of the relativistic domain) is commonly referred as the nonperturbative regime (the exact range of this regime depend on the atom and the laser frequency).

In this domain various phenomena are observed: To mention a few, above threshold ionization (ATI) [13], high order harmonic generation (HOHG) [14], multiple ionization [15]. In the following, we will briefly present the

method we follow for the solution of the time dependent Schrödinger equation (TDSE), a necessary tool to describe the atom-field interaction in this nonperturbative regime.

2.2.1 Atom-Radiation interaction

We start by a brief semiclassical description of the atom-radiation interaction, where the atom is described quantum mechanically and the radiation field classically. This approximation holds for the interaction of atoms with lasers or other intense sources, where the photon density is high.

We assume an electron bound by a central potential and experiencing the action of an external electromagnetic field. The field is expressed in terms of vector and scalar potentials $\mathbf{A}(\mathbf{r},t)$ and $\phi(\mathbf{r},t)$, respectively. There is an infinite number of gauges that represent the same physical field. We impose the condition $\nabla\cdot\mathbf{A}=0$ on the vector potential and therefore choose to work in the coulomb gauge where the vector potential is transverse with respect to the propagation direction. Even this condition only selects a class of gauges and it is still possible to perform gauge transformations within this class.

The Hamiltonian of the atom in the external electromagnetic field is derived using Lagrangian formalism and results to:

$$H=\frac{1}{2m}(\mathbf{p}-q\mathbf{A}(\mathbf{r},t))^2+V(r)+q\phi(\mathbf{r},t) \tag{2.20}$$

where q and m are respectively the charge and mass of the electron and $V(r)$ is the potential of the nucleus (or an effective one). Using the gauge condition we imposed, leading to $\mathbf{Ap}=\mathbf{pA}$, the Hamiltonian (Eq.2.20) is

$$H=\frac{1}{2m}\mathbf{p}^2+V(r)+\frac{q}{m}\mathbf{pA}(\mathbf{r},t)+\frac{q^2}{2m}\mathbf{A}(\mathbf{r},t)^2+q\phi(\mathbf{r},t) \tag{2.21}$$

Setting now $\phi(\mathbf{r},t)=0$ and ignoring $\mathbf{A}^2$ term, since they both lead to a global phase term, we have:

$$H=H_{atom}+\frac{q}{m}\mathbf{p}\cdot\mathbf{A}(\mathbf{r},t) \tag{2.22}$$

where the second term describes the atom radiation interaction in the velocity gauge. An equivalent description comes out if we use a different gauge. Specifically, if one uses the Göppert-Mayer transformation [16]. In brief the

Hamiltonian can be expressed in another gauge by replacing the operators and the potentials by their equivalent in the new gauge. This result in the "length" gauge formulation of the Hamiltonian [17]:

$$H = H_{atom} + \frac{q}{m}\mathbf{r} \cdot \mathbf{E}(\mathbf{r}, t) \tag{2.23}$$

Since the wavelength of the radiation we consider is much larger than the dimensions of the atomic wavefunction, retardation effects are neglected across the atom. In other words, the spatial modulation of the vector potential $\mathbf{A}$ or that of the electric field $\mathbf{E}$, $e^{ik\cdot r}$, is replaced by unity. This means that we replace $\mathbf{A}$ and $\mathbf{E}$ with their value at the center of mass of the atom.

The total wavefunction of the system satisfies the time-dependent Schrödinger equation:

$$i\hbar\frac{\partial}{\partial t}\Psi(\mathbf{r}, t) = H(\mathbf{r}, t)\Psi(\mathbf{r}, t) \tag{2.24}$$

$$H = H_{atom} + H_I \tag{2.25}$$

$$H_I = \begin{cases} \mathbf{A}(\mathbf{0}, t) \cdot \mathbf{p} & \text{, velocity gauge} \\ \mathbf{E}(\mathbf{0}, t) \cdot \mathbf{r} & \text{, length gauge} \end{cases} .$$

Projecting Eq. 2.24 on the basis of the atomic eigenstates, one obtains the following system of differential equations for the coefficient c_{nl} of the eigenstate ψ_{nl}

$$i\frac{d}{dt}c_{nl} = \sum_{nl}\left[\epsilon_{nl}\delta_{nn'}\delta_{ll'} - \langle\psi_{nl}|H_I|\psi_{n'l'}\rangle\right] \tag{2.26}$$

which with the appropriate initial condition (typically the atom in the ground state of the atomic Hamiltonian, i.e. $c_{nl} = \delta_{n,1}\delta_{l,0}$) can be solved in either gauge.

Dipole matrix elements

The evaluation of the term $\langle\psi_{nl}|H_I|\psi_{n'l'}\rangle$ is simple, since it is just $\mathbf{A}$ or $\mathbf{E}$ times the dipole matrix element calculated in the appropriate gauge. This is straightforward since the radial part of the eigenstates is numerically known, and thus is accomplished by a simple integral. Of course the dipole operator connects only states with $l' = l \pm 1$, otherwise the dipole matrix element is zero.

In addition it is easy to show that $\langle\psi_{nl}|\mathbf{p}|\psi_{n'l'}\rangle = i(\omega_{nl}-\omega_{n'l'})\langle\psi_{nl}|\mathbf{r}|\psi_{n'l'}\rangle$. This enables one to compare the dipole matrix elements between the two gauges. Since the eigenfuctions we obtain are approximations of the exact ones, this is used as a test of the approximation quality.

2.2.2 Gauge Selection

Although both gauges are legitimate in the formulation of the interaction of light with atoms, there are some practical limitations one has to take into account in gauge selection [17]. In perturbation theory, the results should be the same in all gauges provided that the wavefunctions are exact. If this is not the case, different gauges are affected in different ways by inaccuracy of the wave function, and the gauge that is influenced less for the specific problem/method should be employed. The number of angular momenta is determined solely by the final and initial state and the order of the process through simple selection rules, and convergence demands are limited in the convergence of the dipole matrix elements.

On the other hand, for time dependent non-perturbative calculations the situation is more restrictive since additional parameters enter the calculation, like the number of angular momenta and the spatial extent of the wavefunction needed to achieve convergence of the results. The velocity gauge appears to be more suitable for time-dependent calculations [18, 5, 17]. The basis size is substantially smaller compared to the case where the length gauge is employed. A detailed discussion on the physical mechanisms behind this difference is presented in [17].

2.3 Two-electron atom

In quantum theory the two-electron atom offers an ideal combination of simplicity and complexity. It offers a testing ground for the three-body problem where accurate and realistic calculations can be performed leading to a deeper understanding of the fascinating aspects of this fundamental problem.

In the following we describe the configuration interaction (CI) method used to describe the system [19]. Also we present an approach enabling

one to deal with the double-continuum of this system in the framework of R-matrix theory [9].

2.3.1 The CI method

The Hamiltonian of a two-electron atom can be written as the sum of the single electron Hamiltonians and the electrostatic interaction term between the two electrons:

$$H = H_o(\mathbf{r_1}) + H_o(\mathbf{r_2}) + \frac{1}{|\mathbf{r_1} - \mathbf{r_2}|}. \tag{2.27}$$

H_o is the one-electron Hamiltonian, $H_o = \frac{\mathbf{p}^2}{2m} + U(r)$. The central potential is the effective potential experienced by the electron, which includes interaction with all inner-shell electrons and the nucleus, or for an atom with only two electrons it is the Coulombic potential due to the nucleus. The term $\frac{1}{|\mathbf{r_1}-\mathbf{r_2}|}$ stands for the electron electron interaction. the eigenstates of this system can be written as simultaneous eigenstates of the $\mathbf{L}^2, \mathbf{S}^2, L_z$ and S_z operators, In the following Λ will stand for the set of these operators.

The eigenstate equation of the two electron system

$$H\Phi^{\Lambda} = E\Phi^{\Lambda} \tag{2.28}$$

is solved in terms of the single-electron Hamiltonian eigenstates which are obtained through the procedure described in Section 2.1.3. This means that the one-electron eigenstates will be used as the basis on which the two-electron eigenstates will be expressed.

The necessary antisymmetrization of the wavefunction of two electrons is accomplished by using the Slater determinant:

$$\psi^{m,m'}_{nl,nl'}(\mathbf{r_1}, \mathbf{r_2}) = \frac{1}{\sqrt{2}} \begin{vmatrix} \phi_{nlm}(\mathbf{r_1}) & \phi_{n'l'm'}(\mathbf{r_1}) \\ \phi_{nlm}(\mathbf{r_2}) & \phi_{n'l'm'}(\mathbf{r_2}) \end{vmatrix}$$

The two-electron orbitals are a sum of the antisymmetrised product of the one-electron eigenstates over all possible projections m of the orbital angular momentum and the spin:

$$\Psi^{\Lambda}_{nl,nl'}(\mathbf{r_1}, \mathbf{r_2}) = \sum_m (-1)^{l-l'} \Big[(2L+1)(2S+1)\Big]^{1/2} \begin{pmatrix} l & l' & L \\ m_l & m'_l & -M_L \end{pmatrix}$$

$$\begin{pmatrix} 1/2 & 1/2 & S \\ m_s & m'_s & -M_S \end{pmatrix} \psi^{m,m'}_{nl,nl'}(\mathbf{r_1}, \mathbf{r_2})$$

The eigenstate Φ^Λ of the two-electron system is then written as a superposition of the two electron antisymmetrized wavefunction (where of course the electron - electron interaction is not included):

$$\Phi^\Lambda = \sum_{nl,n\prime l'} C^\Lambda(nl, n\prime l') \Psi^\Lambda_{nl,nl'}(\mathbf{r_1}, \mathbf{r_2}) \tag{2.29}$$

The coefficients $C^\Lambda(nl, n'l')$ come from the diagonalization of the resulting eigenvalue equation 2.28. This procedure is independent for every set Λ of operators and it can be repeated for every set we wish.

Although this procedure can eventually lead to an exact two-electron state Φ, the convergence with respect to the number of the configurations $(nl, n'l')$ used is slow. The later is the main disadvantage of the CI method. A part of this drawback is lifted by a careful selection of the configurations used. For example, there are some typical arguments, based on angular momentum and parity conservation that the CI is nonzero between two configurations that belong to the same total angular momentum, have the same total spin and have the same parity. On top of this, there are some qualitative criteria. Since the contribution of every configuration depends on the strength of the $\frac{1}{|r_1 - r_2|}$ matrix element, one expects configurations with high overlap in space to give higher contributions. As far as the angular part of the wavefunctions is concerned, configurations with small (or zero) one-electron angular momentum difference (and projections) are more important. For the radial part, since the term $\frac{1}{|r_1 - r_2|}$ is larger the more concentrated the orbitals are (i.e. $\langle r_1 \rangle \sim \langle r_2 \rangle$), one expects the configurations involving bound states to have higher matrix element values than configurations involving bound-continuum or continuum-continuum states.

Since we are dealing with a two-electron system, the classification of states (bound or free) is not straightforward. In the one electron atom, the electron was either bound, or belonged to the continuum part of the spectrum. For the two-electron atom we can have: both electrons bound, one electron bound and one in a free state (single continuum) and both the electrons free. Since

single and double continuum states largely overlap (in the energy spectrum), the discrimination demands additional information for the states.

2.3.2 Multichannel two-electron states

In low-energy scattering theory, the final-state wavefunction of an $(N+1)$-electron atom, with angular quantum numbers Λ, is expanded as (close-coupling expansion) [9]

$$\Psi^{\Lambda} = A_{\Lambda} \sum\!\!\!\!\!\!\int_i \phi_i(\mathbf{r}_1, \ldots, \mathbf{r}_N, \hat{\mathbf{r}}_{N+1}) F_i(\mathbf{r}_{N+1}) + \sum_i c_i \chi_i(\mathbf{r}_1, \ldots, \mathbf{r}_{N+1}) \quad (2.30)$$

where $\mathbf{r}_i$ includes both space and spin coordinates of the ith electron, while the operator A_{Λ} performs the necessary antisymmetrization, as well as the relevant angular momentum coupling between the individual angular momentum of each electron, resulting to the set of quantum numbers denoted by Λ. The functions ϕ_i, known as target states, are eigenstates of the residual system after one electron has escaped. The index i, in principle, runs over both the bound and continuum eigenstates of the total spectrum of the residual system. As long as these eigenstates are computed in terms of basis functions in a finite radial space, the resulting continuus spectrum is discrete and therefore the index i reduces to a finite set of integers which represents both the negative (bound) and positive (continuus) energy target eigenstates. The χ_i functions are known as correlation function, which allow for a better computation of the short-range electron-electron interactions. Note that these functions are solutions of the total system, core plus outgoing electron.

Specifically, for the case of a two-electron atom we have the matrix equations resulting from the two-electron Hamiltonian [20], using basis states of the type:

$$\Psi^{\Lambda}(r_1 r_2) = \sum_{nll',n'}^{N_c,N_s} c_{nll'n'} \Phi^{\Lambda}_{nln'l'}(r_1, r_2) \quad (2.31)$$

where the basis channel wave functions $\Phi^{\Lambda}_{nln'l'}$ are LS-coupled antisymmetrized products of the one-electron target radial function $P_{nl}(r), n = 1, 2, \ldots, N_c$, constructed in a spherical box of radius R with vanishing asymptotic conditions at the boundaries and the B-spline functions $B_{n'}(r), n' = 1, 2, \ldots, N_s$

of order k, defined in the region $[0, R]$:

$$\Phi^{\Lambda}_{nln'l'}(r_1, r_2) = A_{12}\frac{P_{nl}}{r_1}\frac{B_{n'}}{r_2}Y_{LM_L}(\hat{r_1}, \hat{r_2}; l, l') \tag{2.32}$$

where A_{12} is the two-electron antisymmetrization operator. Classification of the states through the index n, denotes the discretization of the spectrum of the eigenstates of the core (He^+) ϕ_i and should be understood as characterizing both, negative energy states (bound) when $\epsilon_n \to \epsilon < 0$ and positive states (continuum) when $\epsilon_n \to \epsilon > 0$. The two-variable angular function Y_{LM_L} is just the projection of the total angular momentum state $|LM_L\rangle$ onto the independent electron states $|lm, l'm\prime\rangle$, given by:

$$Y_{LM_L} = \sum_{m,m'} \langle lm; l'm'|LM_L\rangle Y_{lm}(\hat{r}_1)Y_{l'm'}(\hat{r}_2) \tag{2.33}$$

with $\langle lm; l'm'|LM_L\rangle$ the proper Glebsch-Gordan coefficient. A similar expression relates the two variable total spin function Y_{SM_S} with the one-electron spin functions $\sigma_{m_s}, \sigma_{m'_s}$

Expanding the Hamiltonian on the basis (2.32), the variational method transforms the coupled-channel Schrödinger equations of the system into a linear algebraic equation problem ([8, 10]), with coefficients depending on the energy of the one-electron core states and interchannel coupling potentials [21],

$$\begin{bmatrix} h_{11} - (\epsilon_1 - E)B_1 & V_{12} & \dots & V_{1N_c} & \chi_1 \\ V_{21} & h_{22} - (\epsilon_2 - E)B_2 & \dots & V_{2N_c} & \chi_2 \\ \dots & \dots & \dots & \dots & \dots \\ V_{N_c1} & V_{N_c2} & \dots & h_{N_cN_c} - (\epsilon_{N_c} - E)B_{N_c} & \chi_{N_c} \\ \chi_1 & \chi_2 & \dots & \chi_{N_c} & \chi_b \end{bmatrix} \cdot c = 0,$$

where h is the one electron Hamiltonian, $\mathbf{V}_{ij}$ is the $N_s \times N_s$ matrix which represents the $i - j$ interchannel couplings, χ_i are $N_b \times N_s$ matrices which couple the short range (correlation) states χ_i with channel i and finally χ_b is the $N_b \times N_b$ bound-bound coupling matrix. The operator that couples the various states to each other is the electrostatic Coulomb interaction $1/|r_1 - r_2|$. The energies $\epsilon_i, i = 1, 2, \dots, N_c$ are the energies of the target eigenstates in increasing order ($\epsilon_1 < \epsilon_2 < \dots < \epsilon_{N_c}$). The vector $\mathbf{c}$ contains N_o, out of $N_c + 1$, undetermined elements, each coming from an open channel ($\epsilon_i < E$),

with E being the total energy of the atom. The solution vector $\mathbf{c}$ has $N_c + 1$ vector components, $\mathbf{c} = [\mathbf{c_1}, \mathbf{c_2}, \ldots, \mathbf{c_{N_c}}, \mathbf{c_{N_b}}]$ where the $\mathbf{c_i} = [c_{i1}, c_{i2}, \ldots, c_{iN}]$ component contains the B-spline expansion coefficient of the channel function i.

For an energy of the whole system E, such that N_o channels are open ($\epsilon_n \leq E, n = 1, 2, \ldots, N_o$), for each channel i, N_o linearly independent vectors result. Physically, this reflects the N_o different asymptotic boundary conditions, corresponding to each channel. The discretized channel vectors we obtain in this procedure are not normalized, thus satisfying arbitrary boundary conditions. Recalling the correct boundary conditions, which continuum channels resulting from a photoionization process should satisfy, allows us to normalize the discrete states of positive energy in order to properly represent the physical states of the system. Then the dipole matrix elements can be correctly calculated. A detailed description of this procedure can be found in [20].

When calculating the transition matrix elements, one has to take into account the approximation due to the finite radius R up to which the dipole matrix elements are calculated. The contribution from the outer region ($r > R$) is not important in the case of bound-bound or bound-free transitions, since in these cases at least one wavefunction is limited in space. On the contrary, for free-free transitions it is important, and provided that the asymptotic region has been reached, the matrix element involving two oscilating functions are evaluated as follows:

$$\langle \epsilon l | d | \epsilon' l' \rangle = \int_0^R dr P_{\epsilon l} P_{\epsilon' l'} + I(R) \tag{2.34}$$

where $I(R)$ is given in [22].

In the case of single electron ejection, the effective charge experienced assymptotically by the ionized electron is $z_{eff} = 1$, and this is used for normalization, through the use of the assymptotic Coulomb functions $P(r), Q(r)$. For double-electron ejection this no longer holds. Since both electrons are allowed to escape, they should see the same effective charge. We expect the effective charge seen by the ionized electron to depend on the final ionization stage of the core. A quantitative estimate of the effective charge [23, 24] can

be obtained through the equation

$$z_{eff}(nl;\epsilon l) = 1 + \int_{\langle r\rangle_{\epsilon l}}^{\inf} dr \left[1 - \frac{\langle r\rangle_{\epsilon l}}{r}\right] |P_{nl}(r)|^2 \tag{2.35}$$

where $|nl\rangle$ is the state of the "inner" electron and $|\epsilon; l\rangle$ of the outer, obtained as a coulomb function with $z_{eff} = 2$. The quantity $\langle r\rangle_{\epsilon l}$ is the average position corresponding to that state. Note tha for $nl \equiv 1s$ we have $z_{eff} \to 1$ and for $nl \equiv \epsilon s$ we have $z_{eff} \to 2$, while for other states of nl, z_{eff} varies from 1 to 2. In the present case, the effective charge used for normalizing the states corresponding to double ejection is $z_{eff} = 2$ while for all other states is $z_{eff} = 1$.

CHAPTER 3

ABSORBING BOUNDARIES IN A SPECTRAL METHOD

3.1 Introduction

The advantages of the solution of the TDSE on the basis of the eigenstates of the free system include smaller computational effort, higher flexibility (one can limit the time propagation in the first n levels or equivalently up to a certain energy level) and the final state of the atom (populations of bound states, photoelectron spectrum) is directly calculated without the need to project the final wave-function of the atom on the eigenstates. On the other hand there is an important drawback, directly related to the discritisation of the continuum and the artificial limitations it poses to the system.

In the simplest case, the construction of the atomic basis, as explained in detail in the previous section, is accomplished by 'confining' the atom in a sphere of radius R (case of fixed boundary conditions). Physically this is equivalent to a potential that is infinite at the surface of the sphere. This means that the wavepacket of the electron ejected from the atom by the radiation, after some time ($t \sim \frac{R}{\sqrt{E}}$) will arrive at the boundary of the sphere and will be reflected by the infinite potential barrier. Once this reflected wavepacket approaches the atom, artifacts of the calculation will come up (to mention some: higher harmonics emmited, more ATI peaks, distorted harmonics and photoelectron spectra). Fortunately, this problem can be circumvented by removing the wavepacket that is escaping the atom (better:

the nucleus). This part of the wavefunction is far enough to be equivalent, in its evolution, to a free electron and thus does not interact with light anymore. In any case the above can be tested by varying the radius in which the wavefunction remains intact until the results converge.

This technique has been already employed with success in other computational approaches, either by employing an imaginary potential to imitate absorption or by continuously multiplying the wavefunction with a function that goes smoothly to zero at the boundary for distances higher than a certain radius. In this case, the Schrödinger equation is solved directly in the space where the wavefunction is known at a sequence of grid points [25–30].

In the following we will propose an algorithm to apply this technique in our approach, where the wavefunction is not directly known in space, but only its coefficients on the eigenstates of the system. We will also discuss an extension, appropriate to handle problems involving discritised continua where the actual form of the wavefunction (or of other physical quantitities discritized, like the electric field for example) need not to be known. Finnaly, we will briefly show the capacity of the method to deal with multiple continua.

3.2 Application to an atomic system

3.2.1 Theory

As explained in more detail in the previous sections, the eigenfunctions of the electron are expressed on a B-spline basis, the n-th radial eigenfunction being:

$$P_n(r) = \sum_i c_{in} B_i(r) \tag{3.1}$$

so the radial part of the wavefunction of the electron is:

$$\Psi(r) = \sum_n a_n P_n(r) = \sum_n \sum_i a_n c_{in} B_i(r) \tag{3.2}$$

Equivalently, if A_n is a vector, whose n-th element is the amplitude of the n-th eigenstate (a_n) and Cmn is the matrix of the coefficients of the expansion of every eigenstate in terms of B-splines, then the radial wavefunction is just $W = C \cdot A$. Of course W is a vector, the i-th element of which (w_i) is the

weight of the i-th B-spline on the wavefunction. In other words $\Psi(r)$ is now:

$$\Psi(r) = \sum_i w_i B_i(r) \tag{3.3}$$

Considering now that the i-th B-spline is localized around the i-th grid point (the extent of the B-spline is analogous to its order), if one wishes to multiply the wavefunction with a mask function, it is sufficient to multiply the W vector with a diagonal matrix M, the elements of which are equal to 1 up to the (k_m, k_m) element and smoothly go to zero onward. The new radial wavefunction would be:

$$\Psi'(r) = \sum_i w'_i B_i(r) \tag{3.4}$$

where

$$W' = M \cdot W \tag{3.5}$$

Finding the new coefficient vector A' is easy, since

$$W' = C \cdot A' \Rightarrow C \cdot A' = M \cdot C \cdot A \Rightarrow A' = C^{-1} \cdot M \cdot C \cdot A \tag{3.6}$$

This result means that for a given state vector A, its multiplication with the matrix $B = C^{-1} \cdot M \cdot C$, will result to a new state vector which stands for a new wavefunction unaltered in the region $0 < r < R_m$ and smoothly attenuated to 0 in the region $R_m < r < R$. Once the B matrix is calculated, which it depends only on the basis and the form of the absorbing boundaries, the application of absorbing boundaries on the TDSE is just a matter of vector-matrix multiplication.

In "reality" the electron wavefunction is the sum of the wavefunctions for each l. Since for every l we have a different set of eigenstates, a different B matrix has to be calculated for every l, and applied only to the eigenstate coefficient of this specific l.

One should also note that the frequency of the application of the absorbing boundaries on the coefficients depends on its width and on the fastest wavepacket we want to absorb. A wavepacket with average velocity v would stay inside the absorbing boundary for a time interval $2\frac{R-R_m}{v}$, in which time it should attenuate, so the absorbing boundary should be applied many times. A question deserving further investigation is if the absorbing boundaries can be applied at any time or only at $A(t) = 0$.

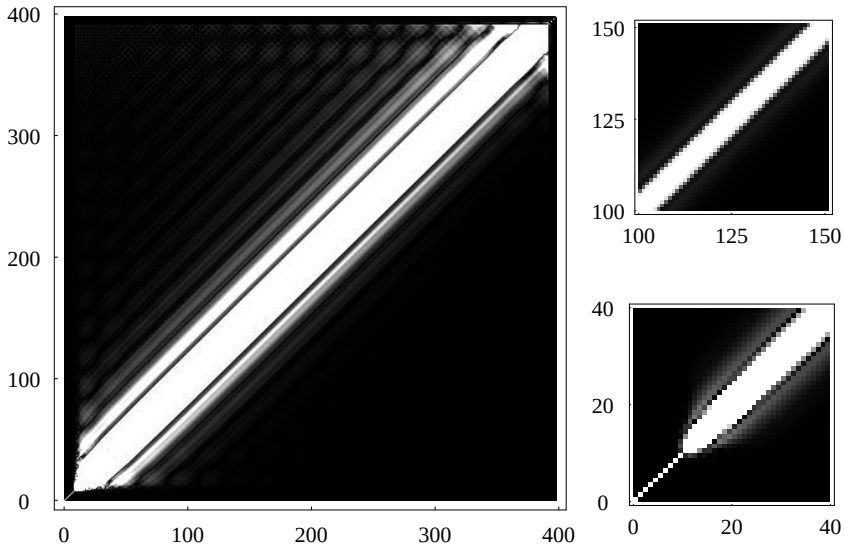

Figure 3.1: A density plot of the absolute value of the absorbing boundary matrix calculated for hydrogen atom in a box of 400 a.u. using 400 B-splines on a uniform knot sequence, resulting to approximately 400 eigenstates (for $l = 0$). The smaller plots on the right are magnified parts of the same matrix.

Since the coefficients of all eigenstates included in the solution of the TDSE are known in every step, it is an easy task to keep track of the population changes after the application of the absorbing boundary matrix. This provides additional information that energetically characterizes the part of the wavefunction that is absorbed/removed. Following this idea we sum for every eigenstate the population change occurring in every mask application. If one wishes to calculate the PES, the population of every eigenstate that has remained (i.e., not absorbed) can be added to the total population removed from this eigenstate by absorption.

3.2.2 Results

In Figure 3.1 we present a typical form of the absorbing boundary matrix calculated for Hydrogen atom inside a box of $R = 400$ a.u. using 400 B-spline. Since we used fixed boundary conditions, this results to 400 discrete eigenstates of the system. It is evident that the elements of the matrix take important values close to its diagonal. Actually, the matrix elements

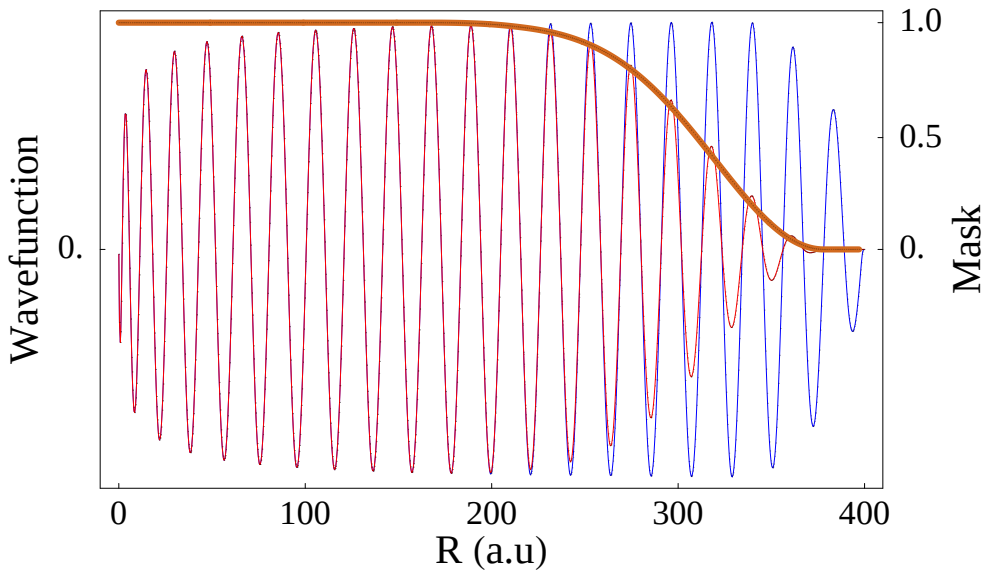

Figure 3.2: The wavefunction of a continuum eigenstate of Hydrogen atom (of about 1 eV energy) before applying the absorbing boundaries (blue), the wavefunction after applying the absorbing boundaries (red) and the form of the absorbing boundaries used (dark red).

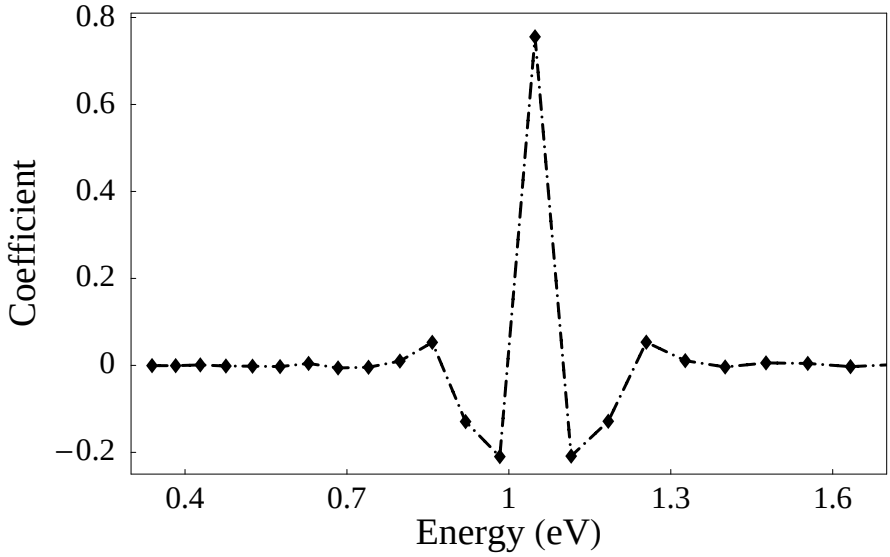

Figure 3.3: Coefficients of the wavefunction (on the basis of the eigenstates) after applying absorbing boundaries on the eigenfunction (with a coefficient 1) of Figure 3.2. Dots point the discrete eigenstates of the atom, dashed line is used only to help visualization.

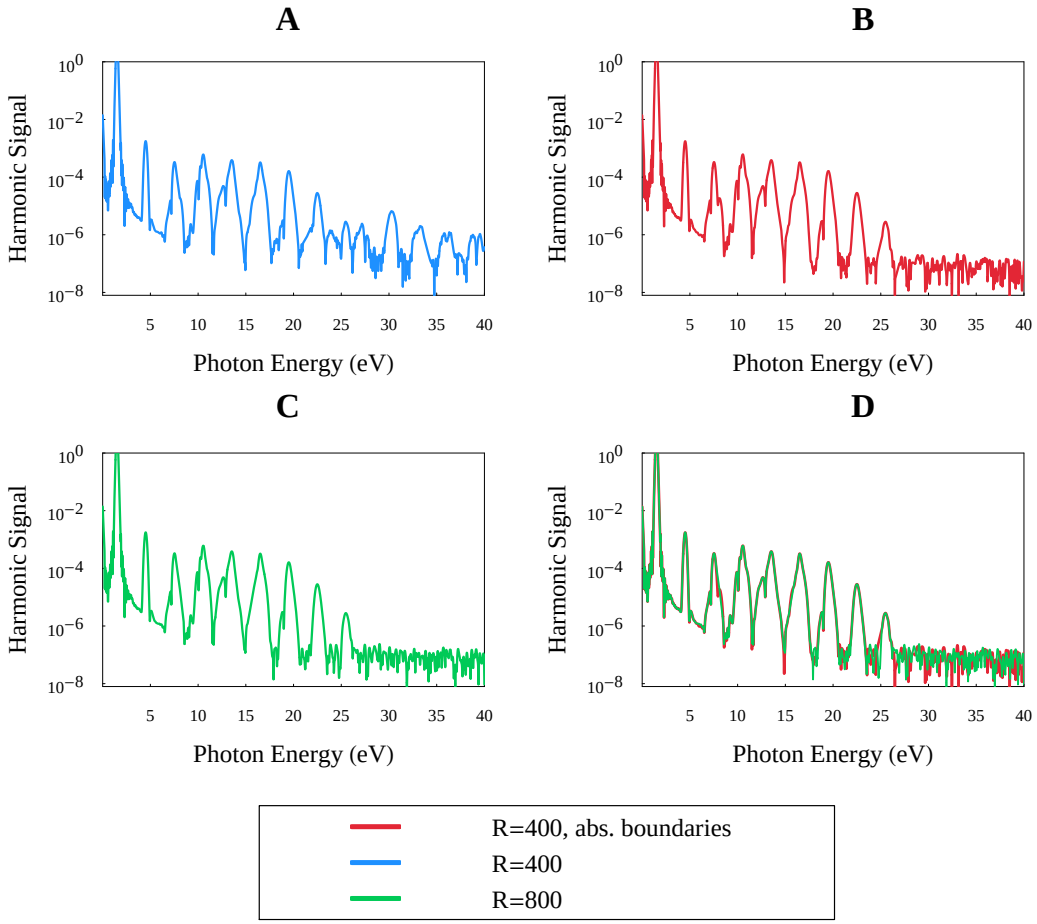

Figure 3.4: Common parameters for all plots: A laser pulse of sin^2 shape, photon energy 1.5 eV, total duration of 20 cycles and maximum intensity $2 \times 10^{13} W/cm^2$.
A. Harmonic emmition spectra calculated in a box of $R = 400$ a.u. without using absorbing boundaries.
B. Harmonic emmition spectra calculated in a box of $R = 400$ a.u. using absorbing boundaries.
C. Harmonic emmition spectra calculated in a box of $R = 800$ a.u. without using absorbing boundaries. In this case the box is large enough so that the electron wavepacket is not reflected,
D. Comparisson of the harmonic emmition of cases **A** and **B**

oscillate, which is better shown in Figure 3.3 where the coefficients are given and not their absolute value. This is natural, since the result of the absorbing boundary matrix on the state vector should be sensitive on the relative phase (sign) of its coefficients, as explained in more detail in the following Section

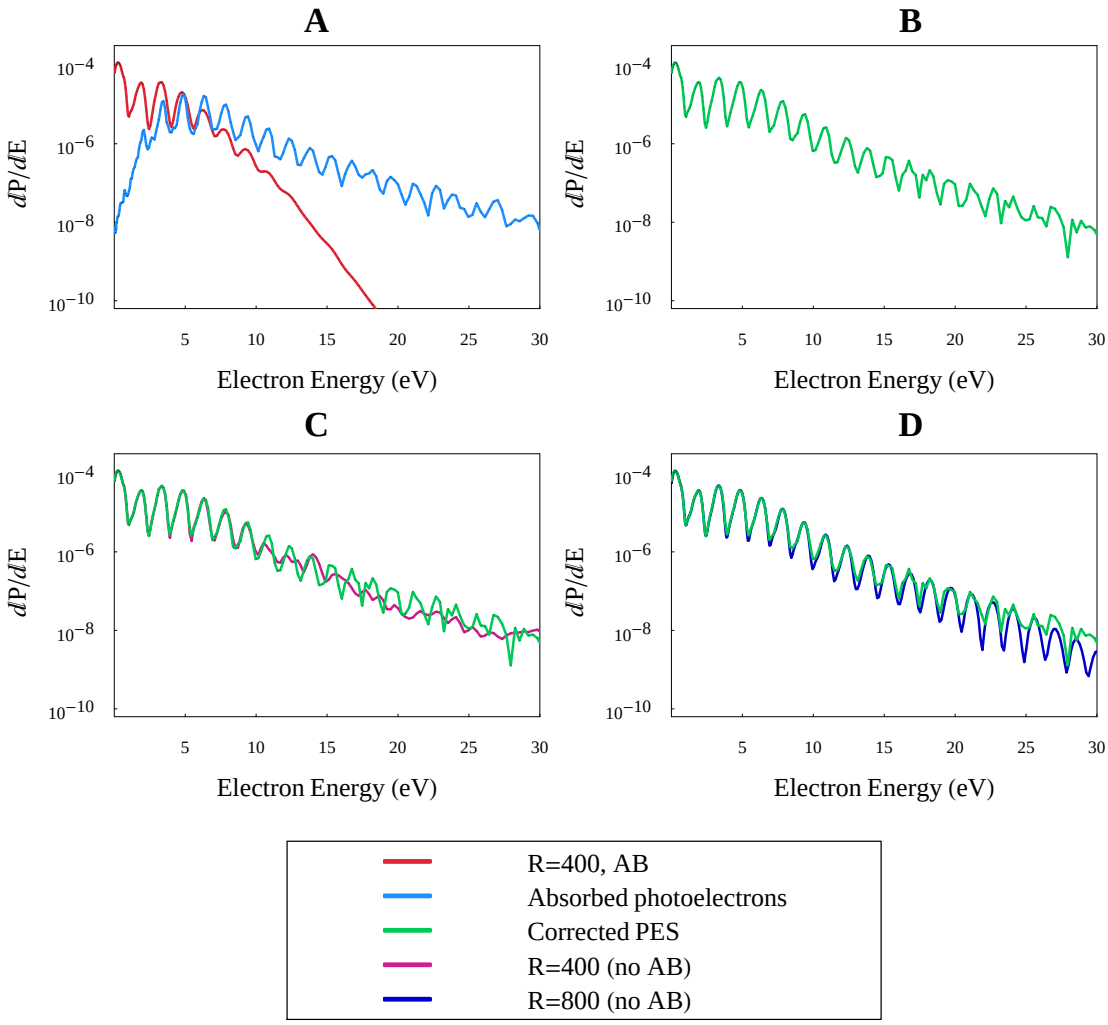

Figure 3.5: Common parameters for all plots: A laser pulse of sin^2 shape, photon energy 1.5 eV, total duration of 10 cycles and maximum intensity $4 \times 10^{13} W/cm^2$.
A. Photolelecton spectra calculated in a box of $R = 400$ a.u. using absorbing boundaries. The remaining PES together with the spectrum of the absorbed electrons is given.
B. Corrected PES, calculated by adding the retained photoelectron spectra with the absorbed.
C. Comparison of the corrected PES with the PES calculated in a same box (i.e., same eigenstate basis) but without use of absorbing boundaries.
D. Comparison of the corrected PES with the PES calculated in a larger box of $R = 800$ a.u..

(3.4)

The first eigenstates of the system are of course the bound ones. A part of the matrix in the region of the bound states is shown at the right bottom part of Figure 3.1. For the first bound states the matrix is practically identical to a unitary matrix, leaving them unaffected, a consequence of their limited extent in space. A smooth transition to the typical form of the matrix in the continuum area occurs at the higher bound states, which reach the absorbing boundary. For the parameters used, the system has 16 bound states, compatible with what is shown in Figure 3.1.

A final remark concerning the general form of the matrix: Parralel to the diagonal there appear "satellite" lines, whose magnitude increases for the last eigenstates of the system. We attribute this to the deficiency of the last eigenstates to faithfully represent continuum eigenstates of the system (the density of B-splines is not high enough to describe them). The same is visible, to a smaller extent though, but of a different origin, for the first continuum states. Due to the small wavelength, the boundaries affect the eigenstates (note the smaller oscillation amplitude of the low energy eigenstate as it approaches the boundary, Figure 3.2). The other way around, an inspection of the matrix can reveal the problematic areas.

As a first check, we show in Figure 3.2 the wavefunction of a continuum eigenstate of Hydrogen atom together with the result of the absorbing boundaries transform on this eigenstate. The result is of course a superposition of eigenstates, with weights as presented in Figure 3.3. The typical width of the weights distribution is related to the width of the mask function. Steeper mask functions result to broader distribution, to provide the required bandwidth.

In Figure 3.4 we show the harmonics emmition spectra calculated in a box of $R = 400$ a.u. with and without absorbing boundaries, together with the results for a bigger box ($R = 800$ a.u.). The later represents the converged results for the laser duration and intensity used. As shown in **A**, due to the small size of the box, the reflected part of the wavefunction interacts again with the nucleus, absorbing more photons resulting to an extended harmonic signal. In **B** we used absorbing boundaries, eliminating thus the reflected part of the wavefunction, so the spectrum has fewer harmonics, and as shown in **D**, it is indistinguishable from the converged spectrum obtained

using a bigger box (**C**).

In Figure 3.5 we present the PES spectra calculated for hydrogen atom exposed in a laser pulse of sin^2 shape, photon energy 1.5 eV, total duration of 10 cycles and maximum intensity $4 \times 10^{13} W/cm^2$. In **A**, we used absorbing boundaries in a box of $R = 400$ a.u. and the PES obtained shows a decrease for photoelectron energies higher than 5 eV due to the absorption of fast electrons at the boundaries. All structure in this spectrum is lost for energies higher than 10 eV. Together we show the spectrum of the absorbed photoelectrons, which is very small for low energy electrons (not enough velocity to reach the boundary and be absorbed). For a region of energies it is comparable to the population of the electrons not absorbed, and for higher energies it dominates absolutely. Adding together the populations of the remained and the absorbed photoelectrons we obtain the PES of part **B**. We compare this corrected PES with PES obtained in calculations without the use of absorbing boundaries. In **C** we used the same box size, and we see that the spectrums are in perfect agreement up to about 10 eV. In this energy, the ratio retained to absorbed population is about 1/10. For higher energies they differ, and the PES calculated without absorbing boundaries loses the typical structure of successive peaks differing by a photon energy. The later is of course due to reflection of the faster electrons by the boundaries and their artificial re-interaction with the nucleus.

To compare the extended part of the corrected PES, we calculated the PES for a larger box, namely $R = 800$ a.u.. The results are shown in part **D** of the figure. The PES spectra are in good agreement for photoelectron energies up to 20 eV, above which they start to have an important difference. Since we used fixed boundary conditions in the construction of the eigenstates, the density of eigenstates in the continuum drops fast with energy (actually energy goes approximately as n^2,with n the discrete eigenstate index). The distance between two successive peaks in the PES is the photon energy. If in this energy region there are not enough discrete eigenstates, the spectrum is not described well. Absorbing boundaries work in this case as well, but the reconstruction of the PES is not satisfactory.

3.2.3 Conclusions

We presented the construction of a linear transform on the state vector of an atomic system, equivalent to the absorbing boundaries employed in the direct solution of the Schrödinger equation in space. The algorithm to construct this transform is simple, involving standard matrix manipulation. The results enable one to perform time dependent calculations on a smaller basis, using thus smaller computational resources both in time and space. We demonstrated the use of this technique in the case of Hydrogen atom. The harmonic spectrum of the atom calculated is free of artifacts due to reflection. The ionization yields were practically identical. In the case of the PES, one can use the additional information of the populations absorbed during the time propagation to obtain a PES that compares well with the converged PES.

3.3 A simpler problem: Infinite well

We will briefly present the case of a particle trapped in an infinite well potential. The same procedure is directly applicable in the case of the electric field in a infinite Q cavity. The interesting part in this case is that, since the eigenstates of the system ($\psi_i(x)$) are simple analytic functions, the absorbing boundary matrix could be analytically evaluated, if we use a simple analytic form for the mask function.

The main argument, in this case, is as follows. The set of the eigenstates of the system form a complete basis so every function can be expressed in this bases using appropriate coefficients. This holds naturally for an eigenstate after the application of the mask function. The elements of the mask matrix are simply these coefficients, the ith column of the matrix are the coefficients for the ith eigenstate.

We can use a simple analytic form for the mask function, well localized in space:

$$M(x) = 1 - e^{\frac{(x-L)^2}{L_w^2}} \tag{3.7}$$

where L is the length of the well, and L_w is used to control the width of the mask function. The eigenstate coefficients are calculated by a simple

projection:

$$C_{mn} = \int_0^L \psi_m(x) M(x) \psi_n(x) dx \tag{3.8}$$
$$\psi_n(x) = \sqrt{\frac{2}{L}} sin(\frac{n\pi x}{L}), 0 \leq x \leq L$$

The integral is evaluated analytically,

$$\boldsymbol{C_{mn}} = \frac{1}{4\,L\,(m-n)\,(m+n)\,\pi}$$
$$\left(e^{-\frac{(m+n)^2\,\pi^2\,L_w^2}{4L^2}}\left(8\,e^{\frac{(m+n)^2\,\pi^2\,L_w^2}{4L^2}}\,L\,(n\cos(n\,\pi)\sin(m\,\pi) - m\cos(m\,\pi)\sin(n\,\pi)) + e^{-i\,(m+n)\,\pi}\,(m-n)\right.\right.$$
$$(m+n)\,\pi^{3/2}\left(\mathrm{erf}\left(\frac{L}{L_w} - \frac{i\,(m+n)\,\pi\,L_w}{2\,L}\right) - e^{n\,\pi\left(\frac{m\,\pi\,L_w^2}{L^2}+2\,i\right)}\left(\mathrm{erf}\left(\frac{L}{L_w} - \frac{i\,(m-n)\,\pi\,L_w}{2\,L}\right) + \right.\right.$$
$$\left.\left.e^{2\,i\,(m-n)\,\pi}\,\mathrm{erf}\left(\frac{L}{L_w} + \frac{i\,(m-n)\,\pi\,L_w}{2\,L}\right) - i\,(-1+e^{2\,i\,(m-n)\,\pi})\,\mathrm{erfi}\left(\frac{(m-n)\,\pi\,L_w}{2\,L}\right)\right) + \right.$$
$$\left.\left.e^{2\,i\,(m+n)\,\pi}\left(\mathrm{erf}\left(\frac{L}{L_w} + \frac{i\,(m+n)\,\pi\,L_w}{2\,L}\right) - i\,\mathrm{erfi}\left(\frac{(m+n)\,\pi\,L_w}{2\,L}\right)\right) + i\,\mathrm{erfi}\left(\frac{(m+n)\,\pi\,L_w}{2\,L}\right)\right)L_w\right)\right), \boldsymbol{m \neq n}$$

$$\boldsymbol{C_{mm}} = \frac{1}{4\,L\,\pi}\left(-\frac{2\sin(2\,n\,\pi)\,L}{n} + 4\,\pi\,L - 2\,\pi^{3/2}\,\mathrm{erf}\left(\frac{L}{L_w}\right)L_w + e^{-n\,\pi\left(\frac{n\,\pi\,L_w^2}{L^2}+2\,i\right)}\,\pi^{3/2}\right.$$
$$\left.\left(e^{4\,i\,n\,\pi}\,\mathrm{erf}\left(\frac{L}{L_w} + \frac{i\,n\,\pi\,L_w}{L}\right) - i\,(-1+e^{4\,i\,n\,\pi})\,\mathrm{erfi}\left(\frac{n\,\pi\,L_w}{L}\right) + i\,\mathrm{erfi}\left(-\frac{i\,L}{L_w} - \frac{n\,\pi\,L_w}{L}\right)\right)L_w\right), \quad \boldsymbol{m = n}$$

with erf the standard error function and $erfi$ the imaginary error function defined as $\frac{erf(iz)}{i}$. In Figure 3.6 we show the value of C_{mn} for different values of L_w and fixed m. Increasing L_w results in a more narrow distribution of coefficients, since a wider variation is associated with a narrower spectrum. This simple case was used to show the more general way to calculate the absorbing boundary matrix, in the case the form of the eigenstates is known, and to show that there is also the possibility of a complicated yet analytic form of this matrix.

3.4 General Case

3.4.1 Introduction

In the previous sections, absorbing boundaries were imposed on a atomic system by using information of the form of the eigenstates in space. Stepping back, we can see that the TDSE is solved on the eigenstates basis of the system, so the only quantities, except for the external field that interfere in

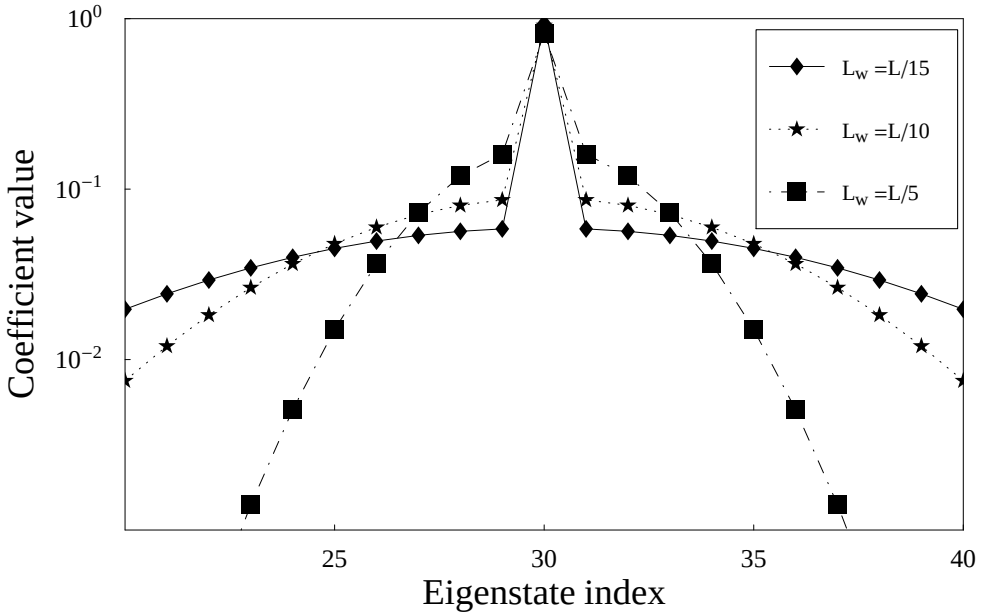

Figure 3.6: Absolute value of the coefficients of the wavefunction (on the basis of the eigenstates) after applying absorbing boundaries on the 30th eigenfunction (with a coefficient 1) in logarithmic scale. The horizontal axes is the number of eigenstate. The L_w parameter, which controls the width of the mask, is shown in the legend.

the solution are the energy levels (which represent both the bound and the continuum part of the spectrum) and the dipole matrix elements between the eigenstates. It is therefore reasonable to assume that the linear transformation that is equivalent to absorbing boundaries can be calculated based only on the above input.

Physically, the dipole matrix elements are irrelevant to the artificial reflection from the boundaries, since they affect only the amplitude transfer between the eigenstates via the external field and not with the propagation of the wavepacket in space. Concerning the energy levels, the critical parameter is naturally the energy level spacing, which is directly connected with the radius of the sphere (fixed boundary conditions). On the other hand, the energy range depends only on the number of B-splines (for a given radius) and one could hardly expect the reflection of a wavepacket energy centered around 2 eV to depend upon the discritisation in the neighborhood of 10 eV.

The preceding discussion, through some intuitive arguments, should pre-

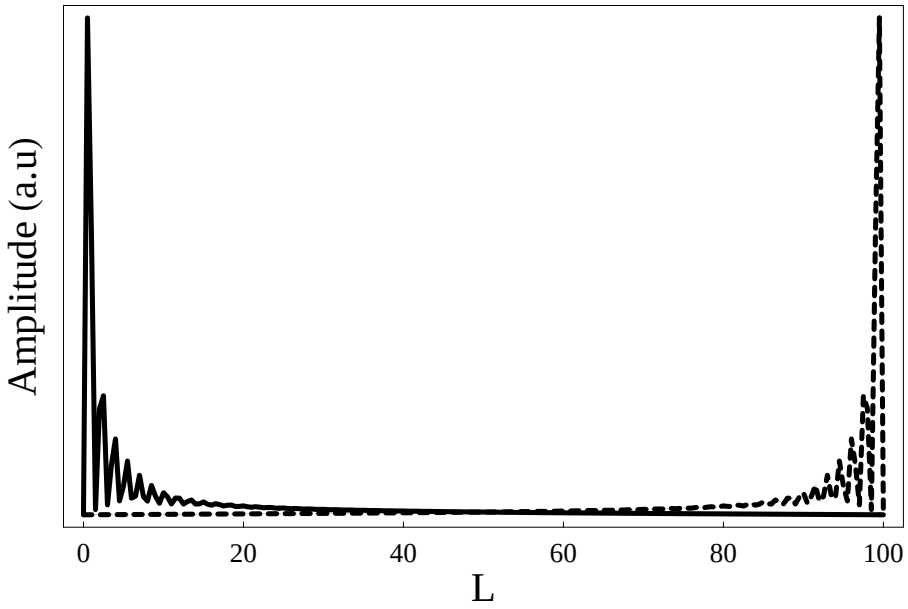

Figure 3.7: The wavefunction for the C_i coefficients (heavy line) and for the C_r coefficients (dashed line) for a infinite well of length L in arbitrary units. We took into account only the first 150 eigenstates, enough to show the localization of the wavefunction in space

pare the ground for the following simple example in which we demonstrate that the only information necessary to calculate the absorbing boundary matrix is the energy levels.

Consider an electron trapped inside an infinite well potential in one dimension. The eigenfunctions of the electron take the simple analytical form:

$$\psi_n = \sqrt{\frac{2}{L}} \sin(\frac{n\pi x}{L}) \tag{3.9}$$

satisfying immediately the Schrödinger equation and the appropriate boundary conditions ($\psi_n(0) = \psi_n(L) = 0$). In this simple system, consider an initial form of the eigenfunction localized close to zero, the left wall of the well, resembling photoelectrons just emmited from an atom. This wavefunction expressed on the eigenstate basis would give a coefficient vector (as usually the i-th element of the vector stands for the coefficient of the i-th eigenstate) that would resemble $C_i = (1, 1, 1, \ldots, 1, 1, \ldots)$. Note that the value "1" is only for illustration, more physical would be a $\frac{1}{\sqrt{N}}$ value, or even a Gaussian distribution. Nevertheless the main idea remains unaltered.

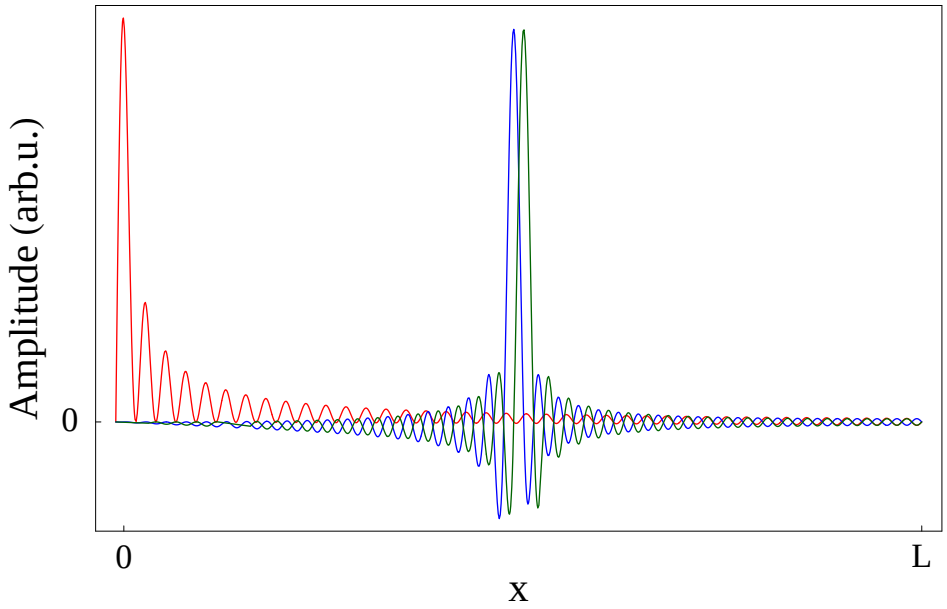

Figure 3.8: Few states of the new bases used. A state at time $t = 0$ (red line) and two consecutive states in the middle of the time interval (green and blue line).

Keeping in mind the symmetry of the eigenstates with respect to the center of the well ($\frac{L}{2}$) (in the case of even n they are antisymmetric and in the case of odd n they are symmetric) it is straight forward to calculate the coefficients of a wavefunction being the image of the initial with respect to the center of the well. It would just be $C_r = (1, -1, 1, \ldots, 1, -1, \ldots)$. This represents practically (letting dispersion aside for the time being) the form of the wavefunction when it is reflected by the right wall. In Fig. 3.7 we plot the wavefunction for the C_i coefficients and the reflected (C_r coefficients).

Considering the simple form of the time evolution of the eigenstates

$$\psi_n(x,t) = \sqrt{\frac{2}{L}} \sin(\frac{n\pi x}{L}) e^{-i\omega_n t} \tag{3.10}$$

it is easy to estimate the time of reflection by calculating the necessary time for this sign change. At time $t = 0$ the coefficients c_1 and c_2 are $c_1 = c_2 = 1$. Their time evolution is thus $c_1(t) = e^{-i\omega_1 t}$,$c_2(t) = e^{-i\omega_2 t}$. At $t = t_{ref}$: $c_1 = 1$,$c_2 = -1$ so $e^{-i\omega_1 t_{ref}} = 1$ and $e^{-i\omega_1 t_{ref}} = -1$ leading to $\omega_1 t_{ref} = 2\pi k_1$ and $\omega_2 t_{ref} = 2\pi k_2 + \pi$. Since we are interested in the first reflection $k_1 = k_2$, which means that $t_{ref} = \frac{\pi}{\omega_2 - \omega_1}$ or $t_{ref} = \frac{\pi}{\Delta\omega}$. In our case, $\Delta\omega$ is not constant

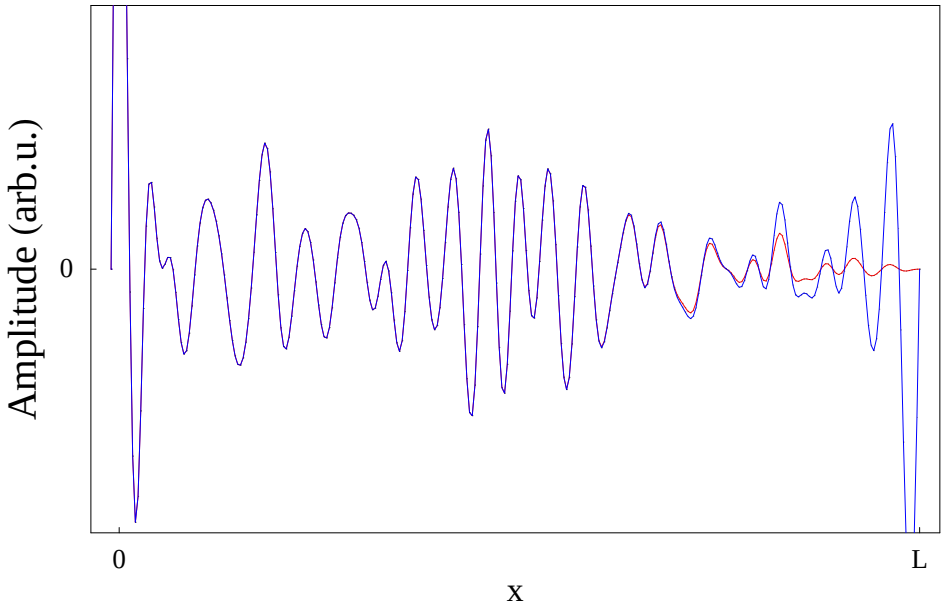

Figure 3.9: Real part of the wavefunction of an electron inside an infinite well constructed by a random distribution of eigenstate coefficients (blue line) together with the real part of the wavefunction after applying absorbing boundaries (red line).

(due to dispersion) so the reflection time for every ω depends on the local density of states.

The key idea is that we can project the coefficient vector at any time on a state like the one that is reflected and subtract this part from the initial coefficient vector. This would remove the part of the wavefunction that is reflected. Of course, absorbing boundaries should be smooth and have a controllable extent. To accomplish this, it is sufficient to construct a new basis consisting of N states that correspond to a different evolution time and gradually remove the last states from the wavefunction,in accordance with the form of the absorbing boundary we want to use. Few representative states of this type are shown in Figure 3.8. The limited size of the bases causes these states not to be completely localized, having long tails. Nevertheless, this did not cause any problems, since it should affect only the states close to the energy boundaries of the discretised spectrum.

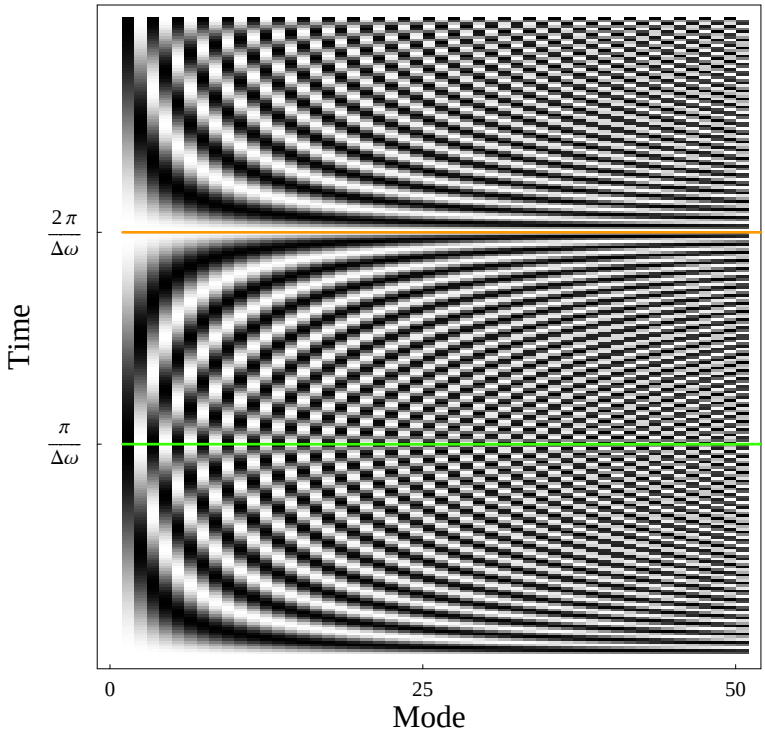

Figure 3.10: The real part of the time evolution of the coefficients of an initial state of the form C_i. The color varies from black to white with the coefficient value varying from -1 to $+1$. The time interval is long enough to observe the reflection at the right wall (at $t = \frac{\pi}{\Delta\omega}$, observe the reflection symmetry of the plot with respect to the $t = \frac{\pi}{\Delta\omega}$ axis and the coefficients that are like C_r) and the next reflection at the left wall (at $t = \frac{2\pi}{\Delta\omega}$, observe again the reflection symmetry with respect to the $t = \frac{2\pi}{\Delta\omega}$ axis and the coefficient that are like the C_i we started with). For this plot the energy level spacing was constant.

3.4.2 Equidistant spectrum

The new basis is constructed as follows[1]. We start by forming a set of vectors describing different evolution times of the system, starting from a initial state close to the origin ($t = 0$), like C_i, and ending with a state close to the box boundary,($t = \pi/\omega$), like C_f. Since we want to form a basis for N

[1] Of course the electron dispersion ($\omega \sim k^2$) and the fixed boundary conditions (infinite well) do not give an equidistant spectrum. Nevertheless, it is the simplest case, so for this part we can either forget this concern (consider an ultra-relativistic electron) or consider a system with the same eigenmodes but with ($\omega \sim k$), like the electric field inside an infinite Q cavity of length L

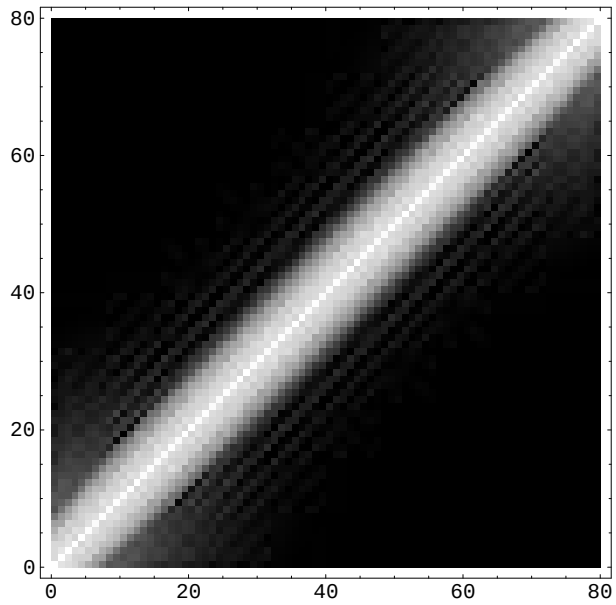

Figure 3.11: The absorbing boundary matrix for a system with $N = 80$, based only on the discrete energy levels describing the continuum. The absolute value of the elements is shown in logarithmic scale, with lighter color for higher values.

independent modes, we split the time interval in N parts. Using a standard Gram-Schmidt procedure, we take this set of N vectors and generate an orthonormal set of basis vectors.

In brief, the new basis comes from the orthonormalization of a $N \times N$ matrix with elements

$$T_{ij} = cos\left(i\Delta\omega \times (j-1)\frac{t_r}{(N-1)}\right) \tag{3.11}$$

where $t_r = \frac{\pi}{\Delta\omega}$ is the reflection time, $i\Delta\omega$ gives the frequency of the i-th level and $(j-1)\frac{t_r}{(N-1)}$ gives the time.

The matrix must have N independent eigenvectors so that, after the orthonormalization, to give a complete basis for the state vector. This is the case due to the fact that the columns of the matrix are almost orthogonal. The inner product of two rows would be:

$$\begin{aligned}\sum_j T_{mj}T_{nj} &= \sum_j cos\left(m\Delta\omega \times (j-1)\tfrac{t_r}{(N-1)}\right)cos\left(n\Delta\omega \times (j-1)\tfrac{t_r}{(N-1)}\right) \\ &\simeq \int_0^{\pi/\Delta\Omega} cos\Big(m\Delta\omega \times t\Big)cos\Big(n\Delta\omega \times t\Big) = \delta_{mn}.\end{aligned}$$

The inner product is not exactly zero because it is a finite representation of the integral. This provides confidence that there are indeed N independent eigenvectors and verified by the observation that the changes from the orthonormalisation to the vectors (columns) were very small.

Then the absorbing boundary matrix is constructed as explained in more detail in Section 3.2. Since the eigenvectors of this basis is time-ordered, the mask now removes gradually the last. The T_{ij} is shown as a part of Figure 3.10, which extends from $t = 0$ $t = 3\frac{\pi}{\Delta\omega}$ and not $t = \frac{\pi}{\Delta\omega}$ as the T_{ij} matrix. In this Figure, it is also easy to observe the reflection at times $t = \frac{\pi}{\Delta\omega}$ and $t = 2\frac{\pi}{\Delta\omega}$, the first at the boundary, the second at the origin. The constructed absorbing boundary matrix is shown in Figure 3.11, and the results of this matrix on a randomly selected wavefunction are presented in Figure 3.9, where the part of the wavefunction approaching $x = L$ is removed.

Special attention has to be paid to the possibility the discrete energy levels not to have the same initial phase. In the previous we dealed with the real part only, where different phase means different sign. The form of the eigenfunctions was such that all of them had the same sign. In the case the form of the eigenfunctions is not known, one has to ascertain that all of them have the same sign, or to incorporate this information in the construction of the absorbing boundary matrix. The method to determine this sign probably depends on the problem at hand. For example in the case of the solution of the TDSE, a good candidate would be the sign of the dipole matrix elements connecting a set of states to a common state.

3.4.3 Free boundary conditions

The case of dispersion or of free boundary conditions requires a slightly different approach. The reflection time is not the same for all the levels. On the contrary, it depends for each level on the density of modes in the vicinity of the corresponding level. This is circumvented by creating a T_{ij} matrix, in which the propagation time (previously just $(j-1)\frac{t_r}{(N-1)}$) is not common for all modes. Instead we use for each level the same fraction of the local reflection time.

The local reflection time is calculated by a simple physical analogy with an equivalent problem. We want to imitate a given discrete spectrum with the

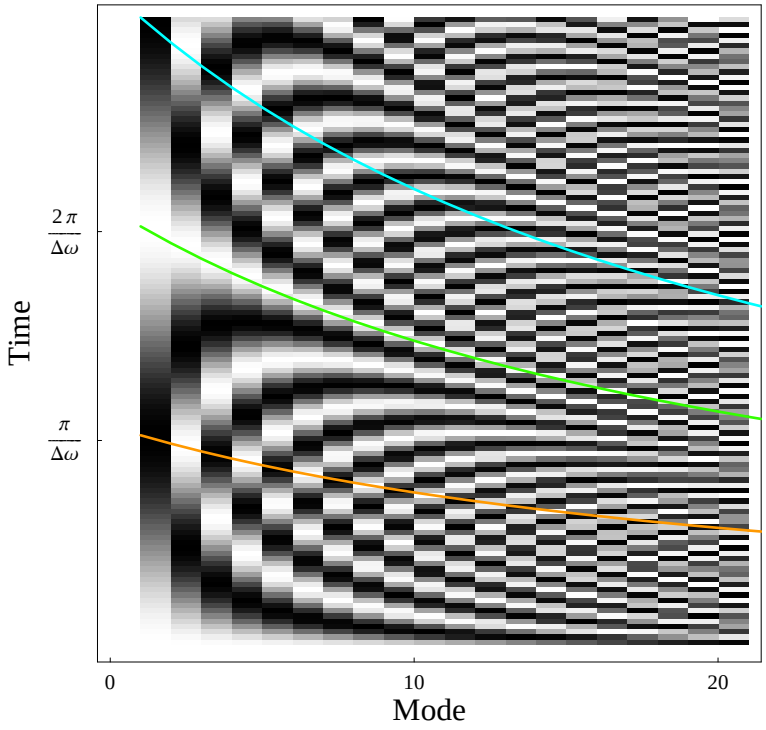

Figure 3.12: Same as in Figure 3.10. In this case the energy levels are not equidistant, following a relation $\omega(n) = \omega(n-1) + \Delta\omega(1+2a(n-1))$ and $\omega(0) = 0$. The colored lines show the estimated reflection times for every mode, $t_r(i)$

spectrum of a, more or less, easily understood system. Consider the electric field in a one dimensional cavity with perfectly reflecting boundaries. If we assume the position of the boundaries fixed, the resulting discrete spectrum is equidistant. If on the other hand we assume that the boundary position depends on frequency, using for example a multilayer mirror, this dependence will shape the spectrum (Figure 3.13). Working the other way round, a given spectrum determines the boundary positions,(i.e. reflection positions for every frequency), so the cavity length for every mode is known. So is the reflection time, which is just L_i, $c = 1$. We will use $\omega(0) = 0$ as the reference for all frequencies. Then $\omega(1)$ is the frequency of the photon of the first mode of the cavity, and $\omega(2)$ of the second mode and so on. Since $\omega = k$ we have $\frac{i\pi}{L_i} = \omega_i$ so $L_i = \frac{i\pi}{\omega(i)}$. Thus the reflection time for each mode is $t_r(i) = L_i = \frac{i\pi}{\omega(i)}$ with only parameters the frequency and the index of the mode.

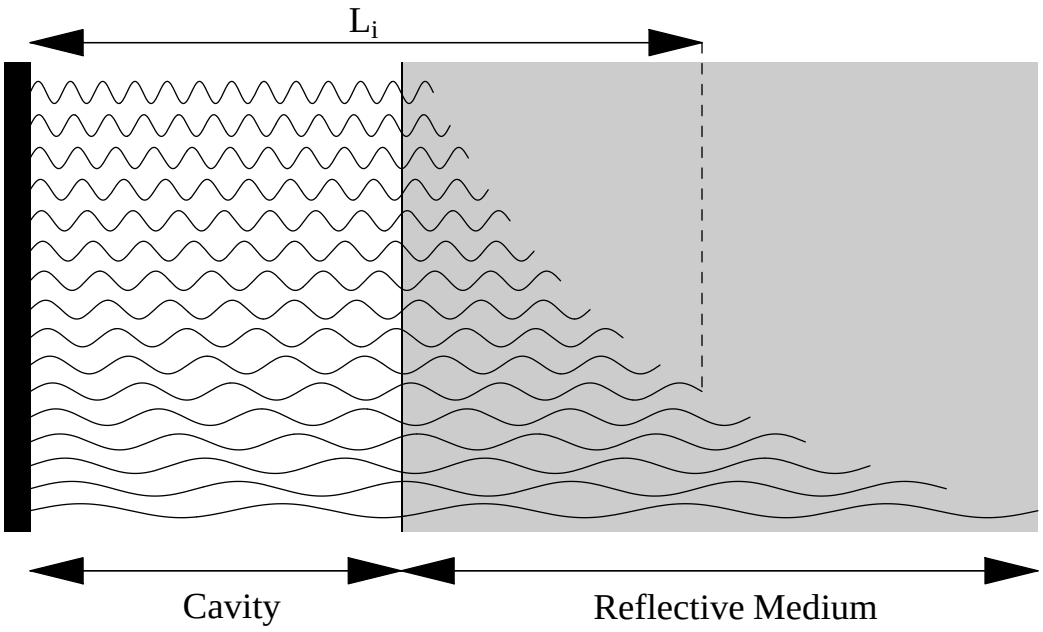

Figure 3.13: For a spectrum as in Figure 3.12 we show the equivalent cavity that imitates this spectrum. The left wall reflects all frequencies at the same point while the right wall reflects every frequency at a different depth. So every mode sees a cavity with different dimensions (L_i) enabling as to shape the spectrum.

So in the case of free boundary conditions or of dispersion, we can use

$$T_{ij} = cos\left(\omega(i) \times (j-1)\frac{t_r(i)}{(N-1)}\right) \tag{3.12}$$

with a rescaled time coordinate different for every mode. This simple transformation converts Figure 3.12 to Figure 3.10, and then it is sufficient to follow the same procedure as in the case of a spectrum with constant energy difference.

3.5 Handling multiple continua

3.5.1 A bit of theory

In the case of multiple discritized continua, the same method is applicable with minor extensions. For example, assume a double continuum, the eigenstates of which are a product of single continuum eigenstates. For sim-

plicity, consider we use n eigenstates of the first and m eigenstates of the second single continuum. There are $n \times m$ combinations, so the coefficient vector has $n \times m$ elements that form the finite basis of the double continuum. By suitable permutations, the coefficient vector can be ordered like: $(c_{11}, c_{12}, c_{13}, \ldots, c_{1m}, c_{21}, c_{22}, \ldots)$. The first m states are composed of the first state of continuum "1" and all the states of continuum "2",the next m are composed from the second state of continuum "1" and all the states of continuum "2" and so on. We construct the absorbing boundary matrix for the first block of m-states using their energy levels, then for the following blocks of m-states it is the same since it depends only on the spacing of the energy levels and not on their value. Then the complete absorbing boundary matrix for continuum "2" is a block diagonal consisting of the previous matrix. Then we employ another set of permutations to order the coefficient vector like: $(c_{11}, c_{21}, c_{31}, \ldots, c_{n1}, c_{21}, c_{22}, \ldots)$ and construct in the same way the block diagonal absorbing boundary matrix for the continuum "1". The complete transformation can thus be included in a matrix being the product of the above transformations, with a general form:

$$D = P_1^{-1} \cdot B_1 \cdot P_1 \cdot P_2^{-1} \cdot B_2 \cdot P_2 \tag{3.13}$$

where $P_{1,2}$ is a suitable permutation matrix used to reorder the coefficient vector as described, $B_{1,2}$ is the block diagonal absorbing boundary matrix for continuum "1" or "2".

3.5.2 Example

Consider now the simple case of a double continuum, that is composed by a small number of single continuum eigenstates. For example, the eigenstates of a free electron in two dimensions are the product of the eigenstates of the electron in the "x" and "y" direction. Limiting the system in a rectangle and taking 30 eigenstates in both single continua would result in $30 \times 30 = 900$ double continuum eigenstates. For simplicity we choose the eigenstates to have constant energy difference, thus the spectrum consists of equally spaced energy levels.

Ordering the state vector in a way that the first permutation is useless, we proceed with the construction of the single continuum absorbing boundary

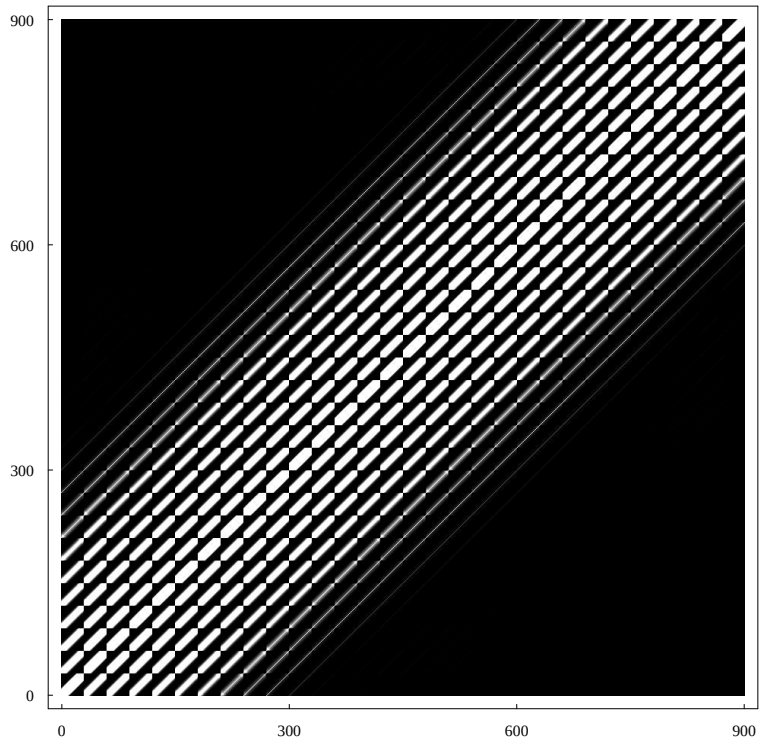

Figure 3.14: Double continuum absorbing boundary matrix. The shading varies from black to white with increasing absolute value of the matrix elements. The structure of the matrix shows how the eigenstates are mixed to imitate absorbing boundaries and at the same time the limitations due to the finite bases (see text for details).

matrix $B_{1,2}$ and then of the double continuum matrix D which is shown in Figure 3.14. Because of the simple ordering of the coefficient vector we chose, there is a similarity of the structure of the D matrix with its single continuum analog. In addition, it becomes clear how this transformation actually works, by combining eigenstates within a block (i.e. with one continuum eigenstate common) and at the same time combining neighboring blocks in an analog way (satellites of the diagonal of the matrix).

Constructing now an initial state composed of a few random eigenstates we can easily create the wavefunction in space and at the same time test the D matrix. In Figure 3.15 we show the initial wavefunction and the wavefunction after applying absorbing boundaries, where it is obvious that it works also in this case. This was also verified in a more quantitative way.

One should note again that the D matrix is affected by the boundaries,

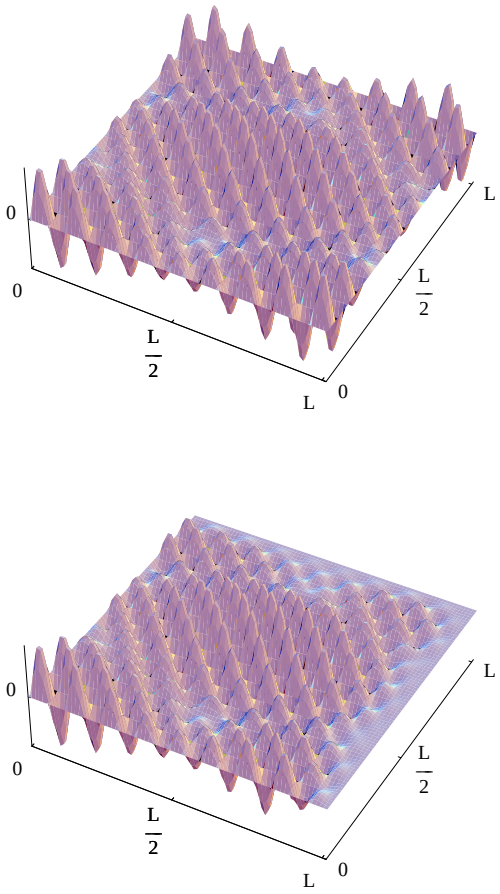

Figure 3.15: Top: the real part of an initial trial wavefunction in two dimensions. Bottom: the real part of the same wavefunction after applying the absorbing boundary transform.

i.e. close to an energy level that has no neighbors (upwards or downwards) for which the transformation does not work well. In this case this applies for double continuum states that include the lowest or the highest eigenstates of any of the two single continua. How many fall in this category exactly depends on the form of the absorbing boundaries. For example a sharp absorbing boundary makes the situation more difficult, since it results to a more "diffused" matrix, that means that many neighboring levels should interfere in this process (equivalently higher bandwidth is needed to describe something steeper).

3.6 Summary

We have shown that it is possible to apply absorbing boundaries on the time propagation of the Schrödinger equation for a real atomic system on the basis of its field-free eigenstates by using a simple linear transform. This means that the artificial reflection of the wavepacket at the boundaries is remedied, so the calculations can be performed on a smaller basis (in space extent) and thus faster. Also, since information about which part of the wavefunction (energy resolved) is removed or modified during the time propagation is easily available, one can use this additional information to reconstruct the final state of the atom (regarding populations, not amplitudes, since phase information is lost), in the case that nothing was absorbed or reflected.

An extension of this method is proposed to handle the general problem of a discritized continuum, based only on the energy spectrum used to approximate the continuum. The calculation of the linear transform can be accomplished numerically or even analytically. Also, we showed that it presents no further difficulties to apply this method to double or multiple continua.

The main limitation is inevitably encountered at the edge(s) of the discrete energy spectrum used to describe the continuum due to the lack of neighboring levels, so one has to ascertain that these states do not play a significant role in the phenomenon examined. In that case, an attenuation in time of these states by a simple exponential decay could remove the problem.

CHAPTER 4

CHARACTERIZATION OF HARMONICS

4.1 Introduction

Harmonic generation is the result of the nonlinear response of matter to radiation. A laser induces a time-varying dipole moment in an atom or molecule. In the weak field regime, the induced dipole moment oscillation, following the laser field, is dominated by the laser frequency ω_0. On the other hand, in a strong field, frequency components of the dipole moment appear at multiples (harmonics) of the laser frequency, $q\omega$, acting as a source of radiation. The even harmonics are forbidden by parity conservation in a medium with inversion symmetry, so the harmonic spectrum consists of a series of peaks centered at odd multiples of the laser frequency.

A multiphoton transition returning to the ground state from a virtual state bellow the ionization threshold (IP) of the atom is the source of the low order harmonics. The higher part of the spectrum results from photon absorption above the ionization threshold and again deexcitation of the (virtual) continuum states to the ground, or other low-energy, states.

The spectrum of the harmonics presents a characteristic shape. The first few harmonics show a rapid decrease of intensity with increasing harmonic order, followed by a region where the intensity remains practically constant, terminated by a cut-off where the intensity falls rapidly to zero. The highest observable harmonic is directly related to the intensity of the fundamental and the atom used. The single atom cut-off scales as $I_p + 3U_p$, where I_p is

the ionization potential and $U_p = I/(4\omega^2)$ is the ponderomotive potential, equal to the average quiver energy of a free electron in the field.

Among other applications of high-order harmonic generation (HHG), they offer the possibility of producing attosecond (as) pulse trains, or even single as pulses. The coherent superposition of harmonics offers the necessary bandwidth for producing such a short pulse. For example a 400 as pulse has a minimum bandwidth of about 10 eV easily accessible using few consecutive harmonics produced simultaneously by a laser with $\omega = 1.5$ eV.

Key role in this application plays the correct superposition of the different harmonics. A random phase for the various harmonics can result to a superposition with much longer time extent, possibly ruining any short-time structure. So it is necessary to characterize the harmonics in order to be superimposed in a controllable way. Due to the low intensity of the harmonics, that does not permit a second or higher order autocorrelation, and to the dispersion introduced by beam splitters, recent efforts are directed towards cross correlations between the harmonic and a correlated infared (IR) field. These approaches rely upon the dynamics of the ionization caused by the harmonics in the presence of the IR field or on phase-sensitive interference effects. Although these methods provide information on the relative phase between the harmonics, they do not account for chirp inside the bandwidth of each harmonic. In case this chirp is small, it should not play an important role on the superposition of harmonics. In the opposite case it should be taken into account and eliminated if possible (using appropriate reflective mirrors).

In the following we will briefly present a method proposed in [31], formulated in terms of perturbation theory, which motivated our work, followed by a study of this proposal based on the numerical solution of the TDSE. This approach is based on phase control of excitation processes and is capable of mapping out the relative phases of the modes of superimposed or individual harmonics.

4.2 Perturbation Theory

The excitation of the atomic system occurs through different coherent pathways, e.g. single-photon excitation through the nth harmonic of the laser

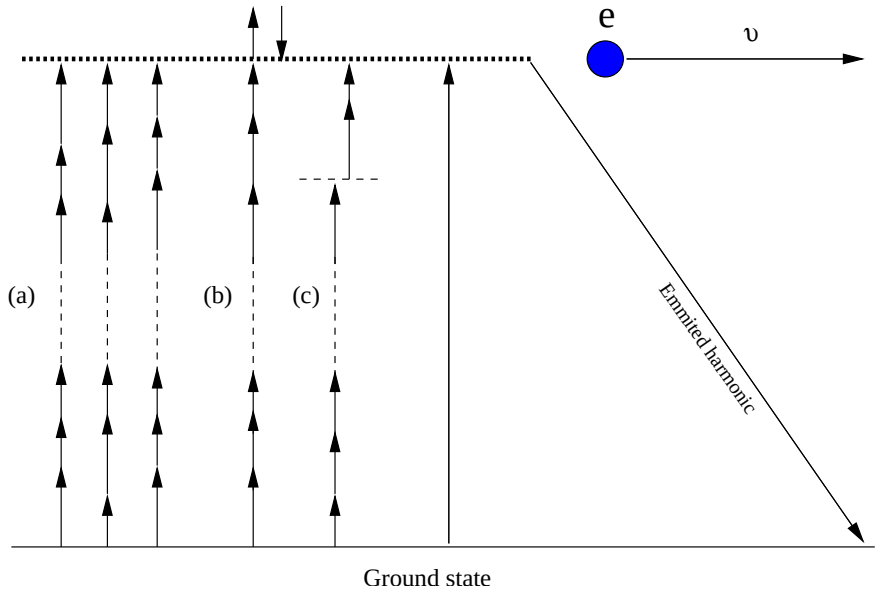

Figure 4.1: Some of the interfering channels leading to an excitation probability that depends on the relative phase between the corresponding fundamental and harmonic modes. In (a) combinations of different modes interfere. In (b) extra photons absorbed or emmited, and in (c) a resonance takes part in the process.

field and n-photon excitation through the fundamental. Variation of the relative phase between the fundamental and the harmonic, assuming both being monochromatic waves, results in a variation of the excitation probability as $cos(\phi_n - n\phi_1)$, where ϕ_n, ϕ_1 are the initial phases of the fundamental and the harmonic.

This variation can be probed through ionization (in case the final state is in the continuum) or through harmonic generation. The latter allows the study of interference below the ionization threshold; so it is applicable for low harmonics as well.

Phase control experiments control the final products of the interaction, but at the same time they probe the relative phase between the fundamental and the harmonic(s). If instead of one harmonic a coherent superposition of harmonics or several individual harmonics are used, the method can be employed to determine the relative harmonic phases and subsequently measure the temporal profiles of the superposition of the harmonic fields.

Since the measured quantity (photoelectrons or photons) depends on the relative phases between each harmonic and the corresponding fundamental

modes and since the phase of all fundamental modes are assumed to be zero for a transform limited pulse, the measured quantity will finally depend on the relative phase between harmonic modes, including thus phase variations introduced through chirp. This relative phase relation is directly related to the time profile of the field, permitting thus to accurately reconstruct it and check for short-time structure, such as *as* beating.

Let the superposition of the electric field of the laser fundamental and that of its harmonics of interest be:

$$\vec{E}_{tot} = \hat{x} \int_0^{\infty} (E_{01}(\omega) e^{i(\omega t - \phi_1(\omega))} + \sum_{n=2k+1}^{2k'+1} E_{0n}(\omega) e^{i(\omega t - \phi_n(\omega))}) d\omega \tag{4.1}$$

where $\hat{x}$ is the polarization unit vector, n denotes each harmonic, k and k' are integer numbers, and $n = 1$ stands for the fundamental. E_{01} and E_{0n} are the spectral amplitudes, ϕ_1 and ϕ_n correspond to the phases of different spectral components and we assume transform limited fundamental pulses, i.e., initial phase $\phi_0(\omega) = 0$ or equivalent (see discussion in 4.4). Thus the bandwidth and the chirp of every harmonic are accounted for.

When this superposition interacts with an atomic system, excitation takes place from a common initial state $|0\rangle$ to a continuum of final states $|f\rangle$. Using lowest order perturbation theory (taking into account procedures of (a) kind), the excitation probability, is proportional to the expression

$$\sum_{n=2k+1}^{2k'+1} \int_{\omega_f} \left| \int_{\omega_{11}} \cdots \int_{\omega_1 n} \mu^{(n)}_{0-f(\omega_{11},\cdots,\omega_{1n})} \times \prod_{j=1}^{n} E_{01}(\omega_1 j) e^{i\phi_1(\omega_{1j})} d\omega_{1n} + \mu^{(1)}_{0-f} E_{0n}(\omega_f) e^{i\phi_n(\omega_f)} \right|^2 d\omega_f \tag{4.2}$$

and thus to

$$C + \sum_{n=2k+1}^{2k'+1} \int_{\omega_f} \left(\int_{\omega_{11}} \cdots \int_{\omega_1 n} \mu^{(n)}_{0-f(\omega_{11},\cdots,\omega_{1n})} \times \prod_{j=1}^{n} E_{01} d\omega_{1j} \mu^{(1)}_{0-f} E_{0n}(\omega_f) \right) \times \cos\left(\phi_n(\omega_f) - \sum_{j=1}^{n} \phi(\omega_{1j})\right) d\omega_f, \tag{4.3}$$

with C a constant. The products $E_{01}(\omega_{11})E_{01}(\omega_{12})E_{01}\ldots(\omega_{1n})$ refer to the n photons of the fundamental that couple the same initial and final state

as the harmonic photon does, i.e., $\sum_{j=1}^{n} \omega_{1j} = \omega_f$ with $\hbar\omega_f$ the energy for the transition $|0\rangle \longrightarrow |f\rangle$

Considering a fundamental pulse Fourier-transform limited, the phase difference for one given final state ω_f is $\phi_n(\omega_f) - \sum_{j=1}^{n} \phi_1(\omega_{1j} = \phi_n(\omega_f) - \omega_f\tau$ with τ the variable delay between the fundamental and the harmonics. $\mu_{0-f}^{(1)}$ and $\mu_{0-f(\omega_{11},\cdots,\omega_{1n})}^{(n)}$ are the corresponding n-photon and single-photon dipole moments induced by each combination of modes of the fundamental and the harmonic radiation, respectively, for each pair of interfering channels $(|0\rangle + \hbar\omega_{11} + \hbar\omega_{12} \ldots + \hbar\omega_{1n} \rightarrow |f\rangle,\ |0\rangle + \hbar\omega_f \rightarrow |f\rangle)$. Since interference occurs in channels coupling the same initial and final state, the result is the coherent summation of the transition amplitudes for the single photon (through the harmonic) and the corresponding n-photon (through the appropriate combination of n modes of the fundamental) excitation channels. The resulting total excitation probability is then the incoherent sum of the contributions of all interfering pairs. For a transform limited fundamental, the oscillations of the probability probe the relative phase between the fundamental and the harmonic modes (and hence between the corresponding modes of the harmonics) and thus the temporal characteristics of their superposition.

Because of the different amplitude factors in the relations given by eqs.(4.1) and (4.3), the variations of the measured quantity will not reflect the total field as far as amplitudes are concerned. Since the harmonic mode phases are extracted, amplitudes may be separately measured through conventional frequency domain spectroscopy.

4.3 Solving the TDSE

Given that the argument in [31] is based on perturbation theory, while from a practical standpoint the question is most interesting in the context of non-perturbative behavior, which is where high order harmonics are produced, we have undertaken the exploration of the scheme in that regime. Since the usefulness of the scheme should not depend on the particular atom employed in its implementation, we have chosen to study the process through the nonperturbative solution of the time-dependent Schrödinger equation (TDSE) for atomic hydrogen, for which rather accurate calculations can be

performed, dispensing thus with the need to speculate on the possible effect of parameters necessary in constructing effective one-electron potentials for more complex atoms. If and when the need arises to interpret experimental results obtained in atoms other than hydrogen, the calculation can be extended accordingly, through a variety of approaches.

The TDSE for the atom in an external laser field is written as

$$\mathrm{i}\hbar\partial_t\psi(t) = [H_0 + V(t)]\ \psi(t), \tag{4.4}$$

with H_0 the field-free atomic Hamiltonian and V the time-dependent interaction between the atom and the laser fields. In the velocity gauge and within the dipole approximation, the interaction operator is

$$V(t) = \frac{-\mathrm{i}\hbar e}{\mu c}\mathbf{A}(t)\nabla, \tag{4.5}$$

with $\mathbf{A}(t)$ being the vector potential connected with the electric field through $E(t) = -c^{-1}\partial_t\mathbf{A}(t)$. In our calculations we assume both laser fields linearly polarized along the z-axis which means that:

$$\mathbf{A}{=}e_z[\mathbf{A}_f p_f(t) + \mathbf{A}_h p_h(t)], \tag{4.6}$$

where indices f, h refer to the fundamental and the harmonic, respectively. The form of p_f is

$$p_f = \sin^2\left(\frac{\pi t}{T_f}\right) \tag{4.7}$$

with T_f being the total duration of the pulse.

This particular envelope form of the fundamental is used for computational convenience since, despite its finite time extent, it is known to provide results similar to those obtained with a more realistic Gaussian envelope. For p_h we use two different envelope forms, a $\sin^2$ and a gaussian, constructed as:

$$g_h(t) = \sin^2\left(\frac{\pi(t - t_c + d)}{T_h}\right), \tag{4.8}$$

and

$$g_h(t) = mask(t)\frac{1}{2\sqrt{\pi}}\int_0^\infty \left(e^{-\frac{1}{4}T_g^2(\omega+\omega_h)} + e^{-\frac{1}{4}T_g^2(\omega-\omega_h)}\right) \times \cos\left(\omega(t - t_c + d) + \phi(\omega)\right) d\omega, \tag{4.9}$$

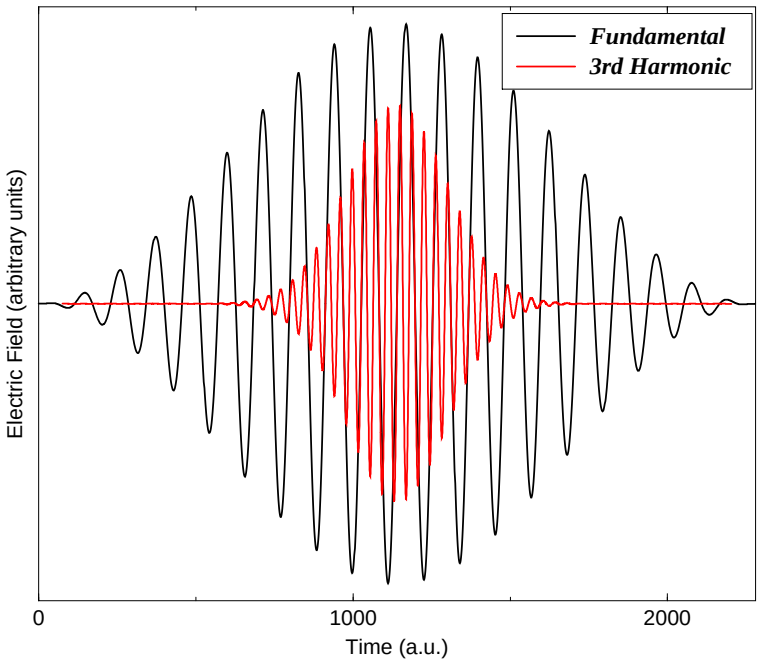

Figure 4.2: The electric field of the fundamental and the (third) harmonic pulse. The fundamental has a $\sin^2$ envelope, while the harmonic has a gaussian. The delay between the two pulses is zero.

with $t_c = \pi/(2T_f)$. For delay d=0, both pulses are centered. The gaussian is used because of the simpler way to incorporate an ω dependent phase of the pulse. Typically, the integral is converted to a summation, limited around the central frequency ω_h, including few hundreds of frequencies, which is more than enough for our purposes. To create a gaussian that resembles the $\sin^2$ pulse as much as possible we have used a $T_g = 0.3T_h$ and to avoid any effects due to the long tails of the gaussian, we employed a $mask(t)$ function :

$$mask(t) = \begin{cases} 1 & , |t - t_c + d| < t_1 \\ \sin^2(\frac{t-t_c+d-t_1}{t_2-t_1}\frac{\pi}{2}) & , t_1 < |t - t_c + d| < t_2 \\ 0 & , |t - t_c + d| > t_2 \end{cases} ,$$

where t_2 is chosen such that the second pulse ends before the first and t_1 is usually around $0.8t_2$, in order to avoid a sharp cut-off of the tail. Depending on the $\phi(\omega)$ function used (e.g. a very sharp one), t_2 can be very limiting causing a significant part of the pulse tail to be missed, which makes trial and error checks obligatory. The above is not the case for the $\phi(\omega)$ we have

used (a gaussian) and under any circumstances it is sufficient to obtain the phase of the created pulse by a simple Fourier transform, and in this way include all effects caused by the mask.

Since the TD-Hamiltonian is invariant with respect to rotations about the z-axis, the magnetic quantum number is conserved, so the expansion of the TD wave function in the basis ϕ_{nl} becomes:

$$\psi(r,t) = \sum_{n,l} b_{n,l}(t)\phi_{nl}(r). \tag{4.10}$$

Substitution into equation (4.4) provides a system of coupled first-order differential equations for the unknown coefficients $b_{nl}(t)$:

$$\mathrm{i}\hbar\partial_t b_{n,l} = \sum_{n',l'}(E_{n,l}\delta_{nn'}\delta_{ll'} + \langle\phi_{n,l}|V(t)|\phi_{n',l'}\rangle)b_{n',l'}, \tag{4.11}$$

with initial condition the atom in the ground state.

Harmonic emmition

The one-atom emission spectrum is calculated as the square of the Fourier transform of the dipole moment, obtained by

$$D(t) = \langle\psi(r,t)|d_g|\psi(r,t)\rangle = \langle\sum_{n,l} b_{n,l}\phi_{n,l}|d_g|\sum_{n',l'} b_{n',l'}\phi_{n',l'}\rangle, \tag{4.12}$$

Note that although the b_n are calculated by propagating the TDSE in velocity gauge, d_g can be in any gauge (length,velocity or acceleration). Everything presented here is in the velocity gauge.

Due to the short duration of the pulse we use (10 to 20 cycles total, not full width at half maximum (FWHM)) and its shape, the system lacks a steady state. Thus, to obtain the harmonic spectra, we perform a Fourier transform of the dipole moment of the atom over the full pulse duration. Also, there is a very small dipole moment, still remaining when the pulse is over and which is due to excitation of bound states and low energy continuum states which have no time to get away from the atom. A direct Fourier transform of this dipole moment would lead to a high noise level which can overshadow the

weakest harmonics. To overcome this problem, we apply a $\sin^2$ filter over the full time range of the dipole moment. We checked that this form of filter is free of side effects by observing the time profile of the harmonics generated [32]. It is worth mentioning that, since we do not take propagation effects into account, it is preferable to use the Fourier transform of the dipole moment instead of its correlation function [33]. For better frequency resolution, we expand the time range by assuming that the dipole moment is zero before and after the pulse. All spectra presented here are the absolute square of the Fourier transform and do not include any ω dependent prefactor.

Typical checks for convergence of the calculation where carried out (upper limit of the energy in the continuum and the number of angular momenta used to describe the atom, the sampling rate of dipole moment and the time step of the TDSE propagation). In addition, the above threshold ionization (ATI) spectra with the same pulse are in good agreement with those provided by Cormier and the harmonic spectrum compares well with the one given by Cormier and also with [26, 34].

4.4 Extracting the phase profile

To measure the phase of a harmonic through its interference with the fundamental, we have to ascertain first that the interference effects are as clear as possible. We have to select the intensities of both fundamental and harmonic so that their contribution to the generated radiation is of comparable magnitude.

A simple approach to determine approximately this region of intensities is to first ensure that we obtain a clear harmonic signal with the intensity of the fundamental we use. Then, we follow the change of the signal, as we gradually increase the intensity of the second pulse. In the beginning, when the intensity of the second laser is very low, harmonic production is dominated by the fundamental and the modulation of the harmonic signal is unimportant. As we approach the range of intensities where both channels are comparable, we will notice a modulation of the harmonic signal; which is attenuated if we further increase the intensity of the second laser, in which case the harmonic signal shows a steady increase, indicating that we have reached the regime where the generation of the harmonic is dominated by

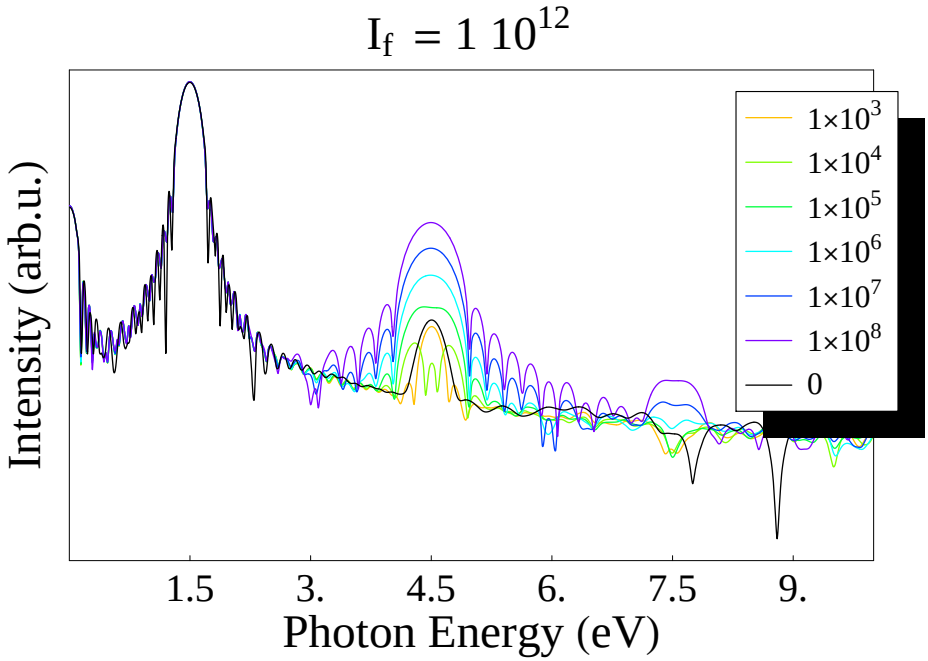

Figure 4.3: The intensity of the emmited radiation for various combinations of intensities of the fundamental and the third harmonic . The fundamental has a maximum intensity of 1×10^{12} W/cm^2 and the intensity of the third harmonic is shown in the legend

scattering of the second pulse. This procedure is shown in Figure 4.3 where we present the intensity of the harmonics emmited by the atom when it is exposed to both pulses at the same time, as we vary the intensity of the harmonic (shown in the legend).

For constant intensities of the fundamental and the harmonic, we solve the TDSE for the atom for a broad enough range of time delay between them. The delay of the two pulses affects the harmonic signal (and PES). The harmonic signal at a specific frequency as a function of the delay is very close to sinusoidal (as anticipated by [31]),so extracting the phase (and frequency) is both easy and well defined. In Figure 4.4 we show a typical modulation of the harmonic signal as a function of the delay for a specific frequency. Through a fit of the form $(a + b\ t) + c\ \sin(\omega t + \phi)$,with a minimal set of parameters,we determine the phase ϕ for zero delay. Parameter b is used to account for a possible drift of the oscillation. Typically, we find that it is sufficient to limit ourselves to 2 periods of the harmonic, split in more

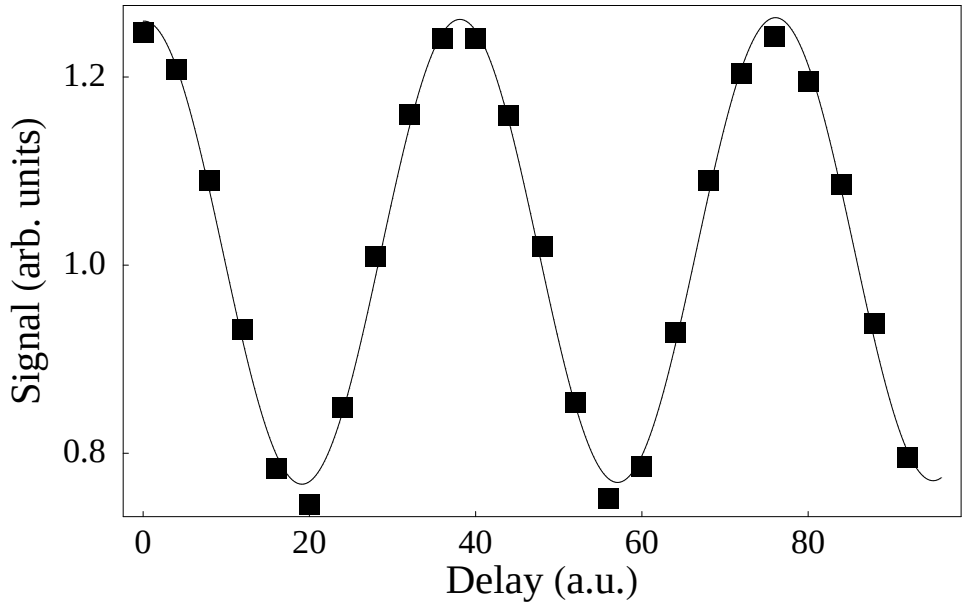

Figure 4.4: Modulation of the 3rd harmonic signal (at 4.5 eV) as a function of the delay between the fundamental and the harmonic pulse. Fundamental is a $\sin^2$ laser pulse of maximum intensity of 1×10^{12} W/cm^2, $\omega = 1.5$ eV and total duration of 10 cycles. The third harmonic laser pulse has a gaussian envelope, maximum intensity of 1×10^3 W/cm^2 and total duration 10 cycles. Note that the period of the modulation is the same as the period of the 3rd harmonic pulse.

than 20 intervals. This procedure is repeated in the desired frequency range for many different frequencies and results to the phase profile of the harmonic with a resolution depending on the number of frequencies used.

Of course the choice of zero delay has no importance; we can determine the phase ϕ for whichever delay (common for all frequencies). Note that what is meaningful is the variation of the phase, and not its magnitude, since the latter depends on the arbitrarily chosen time.

In order to perform a phase shift, if we want to compare two phase profiles, we have to take into account that the modulation frequency is not constant (it is ω) and to add a phase shift in every frequency analogous to ω (since a $\Delta\phi$ at a frequency ω corresponds to a $\omega\ \Delta t$). Also, since the phase is determined modulus 2π, the addition of a factor $2n\pi$, n integer, does not affect the results.

Obtaining the phase profile of a harmonic is a two-step procedure. First, we calculate the reference phase, which is the phase of the modulation in the

case the harmonic has a $\phi(\omega) = 0$. Then we subtract the reference phase from the phase of the modulation of the pulse we want to characterize, for every ω. It is clear from the above that a reference phase of the form $a\omega + 2n\pi$ is equivalent to 0 and need not be calculated or determined.

4.5 Results

4.5.1 Third Harmonic

As a first approach and test, we consider the simplest case, namely the third harmonic. The reason for this, is that the lower the harmonic, the easier it is to observe an interference between the harmonic and the fundamental. A low harmonic can be produced with low fundamental intensity, so non-perturbative effects play the smallest possible part. In other words, this setup (low intensity - low harmonic) allows us to study the problem as clearly as possible.

The fundamental is a $\sin^2$ pulse of maximum intensity of 1×10^{12} W/cm^2 and frequency 1.5 eV, with a total duration of 10 or 20 cycles (28 or 56 fs, equivalent FWHM 14 and 28 fs respectively). The third harmonic has a gaussian envelope and its duration is taken approximately a third of that of the fundamental.

The harmonic signal produced by exposing the H atom to a 10 and 20 cycle fundamental (Figure 4.5) demonstrates a clear third harmonic peak in both cases, together with a peak around 10.2 eV corresponding to excitation of the $2p$ state by the laser.

The intensity of the laser is low, and harmonics higher than the third are not observed. The phase of the produced harmonic is more "stable" for the longer pulse, as expected, and very close to zero (less than a tenth of a rad). Next we add the second source, and gradually increase its intensity which leads to a first estimate of the appropriate range of intensities of the third harmonic in the region of $10^3 - 10^4$ W/cm^2 (shown in Figure 4.3).

The next task is to obtain harmonic spectra as a function of the delay between the two pulses. In general, the overall modulation of the radiation is smoother and weaker if we are in a region where one channel dominates. In the opposite case, where both channels are comparable, the modulation is

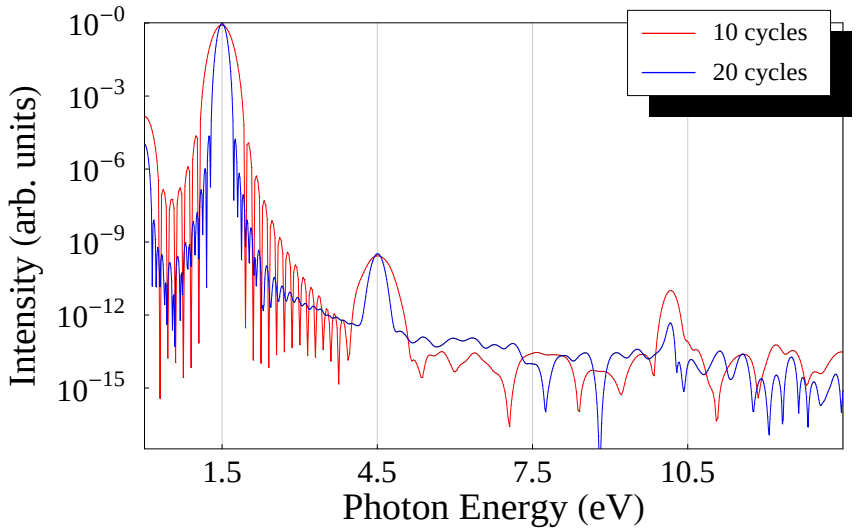

Figure 4.5: Radiation intensity produced by exposing the H atom to a 10 and 20 cycle laser pulse as shown in the legend. The fundamental has again a maximum intensity of 1×10^{12} W/cm^2 and $\omega = 1.5$ eV. The spectrum is normalized at the fundamental intensity.

stronger and has rapid variations in magnitude.

The reference phase is very close to the phase of the harmonic produced by the fundamental only, compatible with the Fourier limited pulse we used ($\phi(\omega) = 0$). Note again that the absolute value of the phase cannot be determined by interference, only differences are meaningful (for the same frequency).

Using now a gaussian pulse for the harmonic, and choosing its $\phi(\omega)$ to be a gaussian centered at the maximum of $I(\omega)$ (4.5 eV) we obtain the reconstructed phase of the pulse for various intensities of the harmonic as seen in Fig. 4.6. We subtracted the reference phase from the phase measured using the pulse with chirp. The phase measured for a pulse with chirp, without this subtraction is, in this case, very close to the previous, because the reference phase is linear with ω. Increasing now the fundamental duration to 20 cycles and following the same steps we obtain the phase profile for the pulse used (Fig. 4.7). In both cases, the results we obtain do not change significantly as we vary the intensity of the harmonic.

Note that the subtraction of phases has meaning only for the same frequency. So, in this case we do not determine the frequency of the modulation

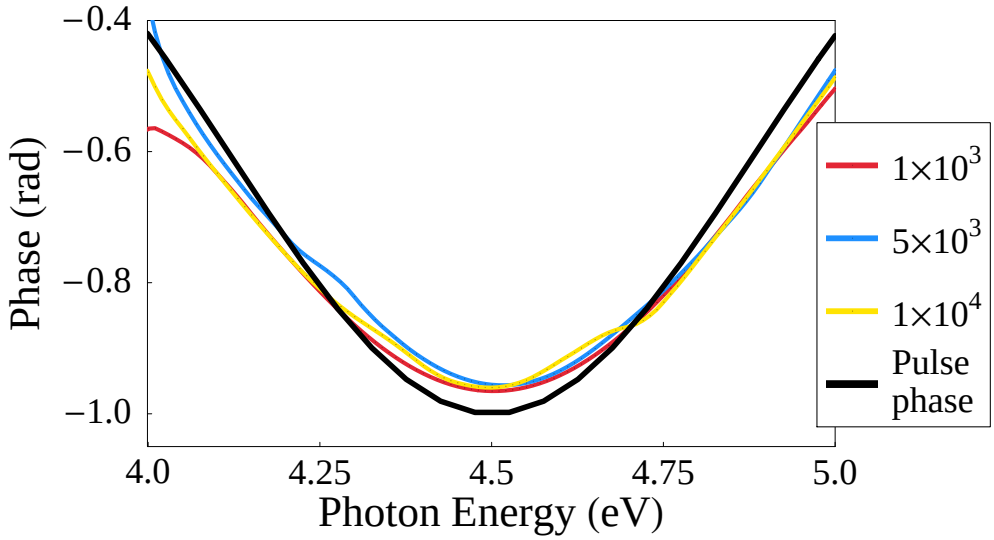

Figure 4.6: With conditions as in Fig. 4.4, we show the difference of the phase measured by the interference of the fundamental and the harmonic with a gaussian $\phi(\omega)$ (shown in the figure) and with $\phi(\omega) = 0$. The harmonic pulse has intensity as shown in the legend, and the modulation frequency is set equal to the frequency of the photon.

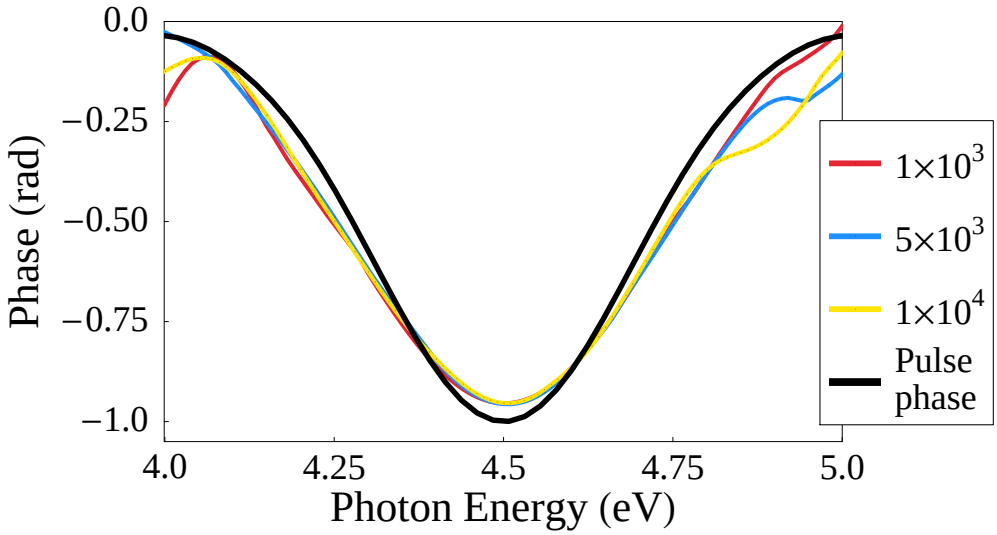

Figure 4.7: Same as Fig. 4.6, but now the duration of the fundamental and the harmonic pulse is increased to 20 cycles for both.

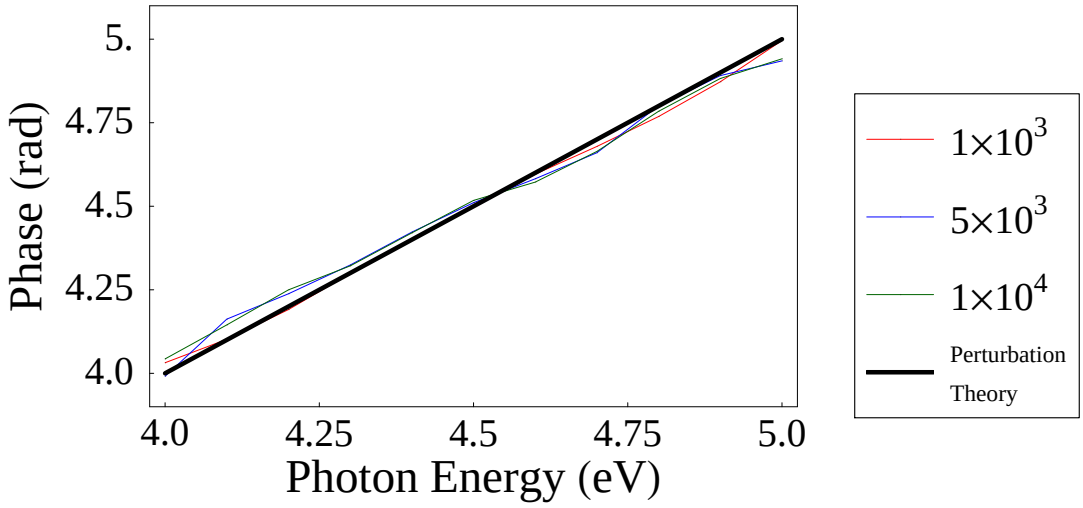

Figure 4.8: Frequency of the modulation as a function of the photon energy for various intensities of the third harmonic. The maximum intensity of the fundamental is 1×10^{12} W/cm^2, and its duration is 20 cycles. The duration of the third harmonic is a third of the duration of the fundamental, i.e. 20 cycles. We also show the modulation frequency expected by perturbation theory for comparison.

through the fit, since it leads to slightly different frequencies for different conditions, but we assume a modulation frequency equal to the frequency of the photon emmited. This is what perturbation theory predicts and its difference from the frequency we obtain from the intensity modulation is at most a few percent. In any case, the main point is to have a common modulation frequency. Figure 4.8 shows the modulation frequency for the case of a 20-cycle fundamental together with the (linear with photon energy) modulation frequency expected by perturbation theory.

It is worth mentioning that there is a systematic tendency for the extracted $\phi(\omega)$ to be slightly flattened, resembling a moving average of the original. This effect is found to be insensitive to variations of the intensity of the fundamental (Figure 4.9) and the harmonic (Figures 4.7 and 4.6). Increasing the duration of the fundamental but keeping the duration of the harmonic constant showed a small decrease of this tendency, as shown in Figure 4.10. On the other hand, these results imply that the reconstruction of the harmonic phase profile for the third harmonic is not sensitive to the duration and intensity of the fundamental and harmonic used. Nevertheless, an experiment would face different problems, since the modulation of the

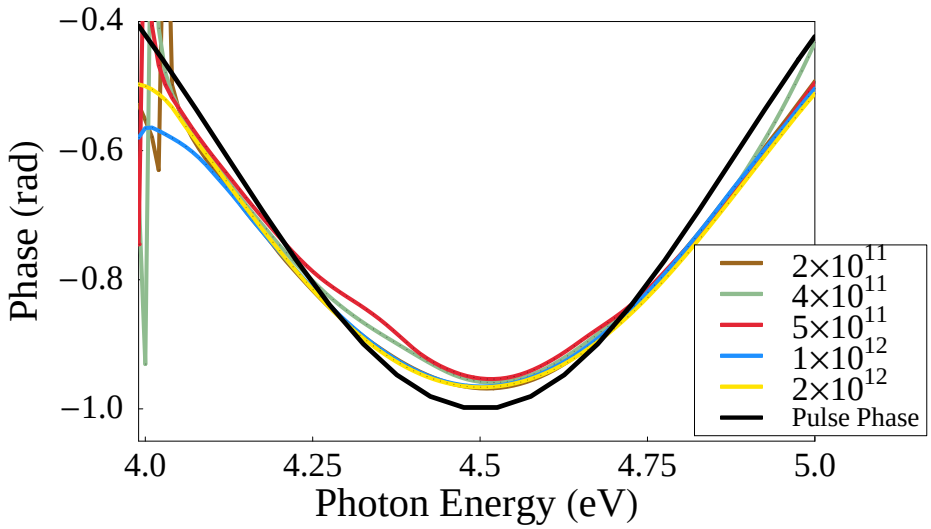

Figure 4.9: The difference of the phase measured by the interference of the fundamental and the harmonic with a gaussian $\phi(\omega)$ (shown in the figure) and with $\phi(\omega) = 0$. The maximum intensity of the harmonic pulse is constant and the maximum intensity of the fundamental pulse harmonic is shown in the legend. Duration of both pulses is kept constant (10 cycles for both).

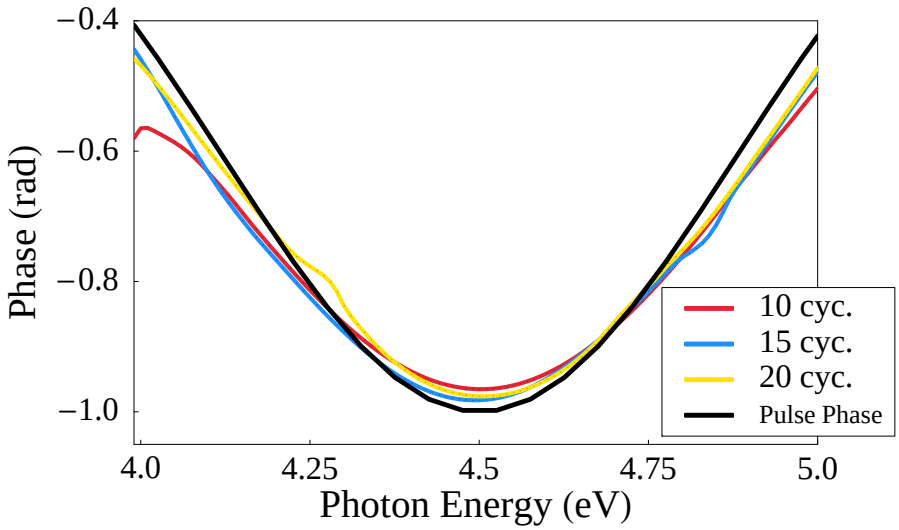

Figure 4.10: Same as in Figure 4.9, bu in this case we kept constant the intensity of both pulses, and increased the duration of the fundamental (shown in the legend).

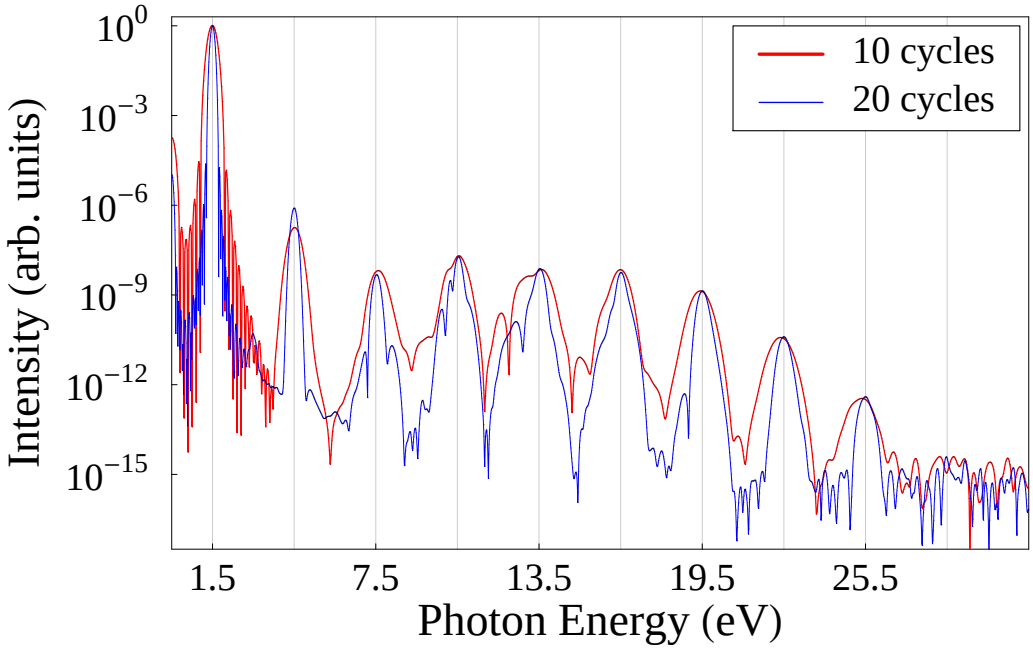

Figure 4.11: The harmonic signal generated by a $\sin^2$ laser pulse of maximum intensity of 2×10^{13} W/cm^2 and $\omega = 1.5$ eV and total duration of 10 and 20 cycles. The spectrum is normalized at the fundamental frequency.

signal should be strong enough, in order not to be overshadowed by noise (fluctuation of laser intensity,...). This requires a careful selection of the two pulses in the spirit described in the begining of the previous section.

4.5.2 Eleventh Harmonic

Considering now a more complicated and interesting case, we study the eleventh harmonic, which for the particular atom and laser frequency under consideration has the additional complication that it is the first harmonic produced in the continuum of the atom. Again we keep the duration of the 11th harmonic pulse close to a third of the duration of the fundamental. In Fig. 4.11 we show the harmonic signal produced by exposing the H atom to 10 and 20 cycle fundamental of 2×10^{13} W/cm^2. With this intensity we are able to obtain clear harmonic signal up to the 17th harmonic. We can create the time profile of the generated harmonics by inverse Fourier transform in the bandwidth of each harmonic.

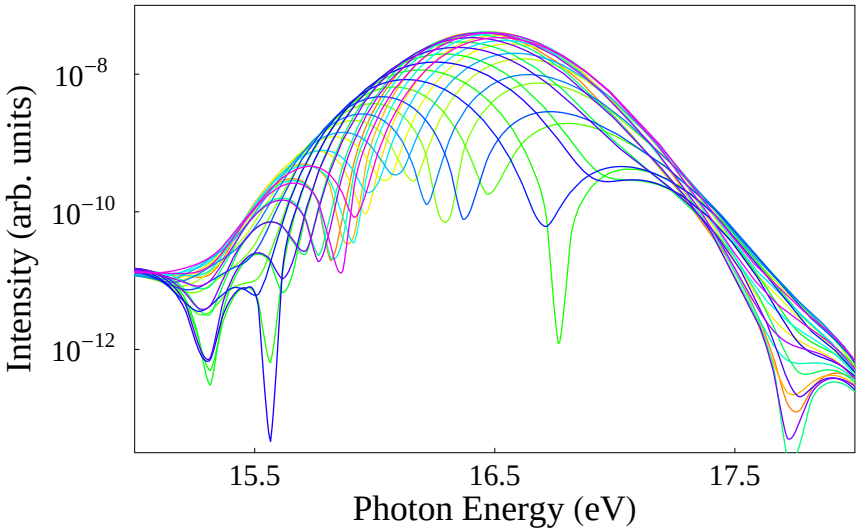

Figure 4.12: The modulation of the harmonic signal when Hydrogen atom is exposed to two laser pulses, a fundamental of maximum intensity of 2×10^{13} W/cm^2, $\omega = 1.5$ eV and total duration of 10 cycles, and a 11th harmonic pulse of 1×10^8 W/cm^2, $\omega = 16.5$ and total duration of 30 cycles. We vary the delay between the two pulses from 0 to 22 a.u.. Colors vary from red to blue with increasing delay.

We found the maximum amplitude for the 11th harmonic to be shifted by a cycle of the fundamental after the maximum of the fundamental for a 10-cycle fundamental, while, in the case of 20 cycle fundamental the maximum was retarded by only half a cycle.

Applying now together with the fundamental the 11th harmonic pulse, and gradually increasing its intensity, we estimate the intensity of the harmonic pulse, needed for the harmonic production through the fundamental and the harmonic to be comparable, to be around 10^8 W/cm^2.

The next step is to obtain harmonic spectra as a function of the delay between the two pulses, resulting to modulations of the spectra as shown in Fig. 4.12 and 4.13. In the latter figure, the distortion caused by the chirp is visible.

In Figs. 4.14 and 4.15 we show the phase resulting by applying a pulse with a $\phi(\omega) = 0$ (reference phase) and one with a gaussian $\phi(\omega)$. By subtracting the reference phase from the phase measured with a pulse with a chirp, we obtain Fig. 4.16; so even for a fundamental pulse as short as 10 cycles we can retrieve the chirp of the harmonic with an error of less than

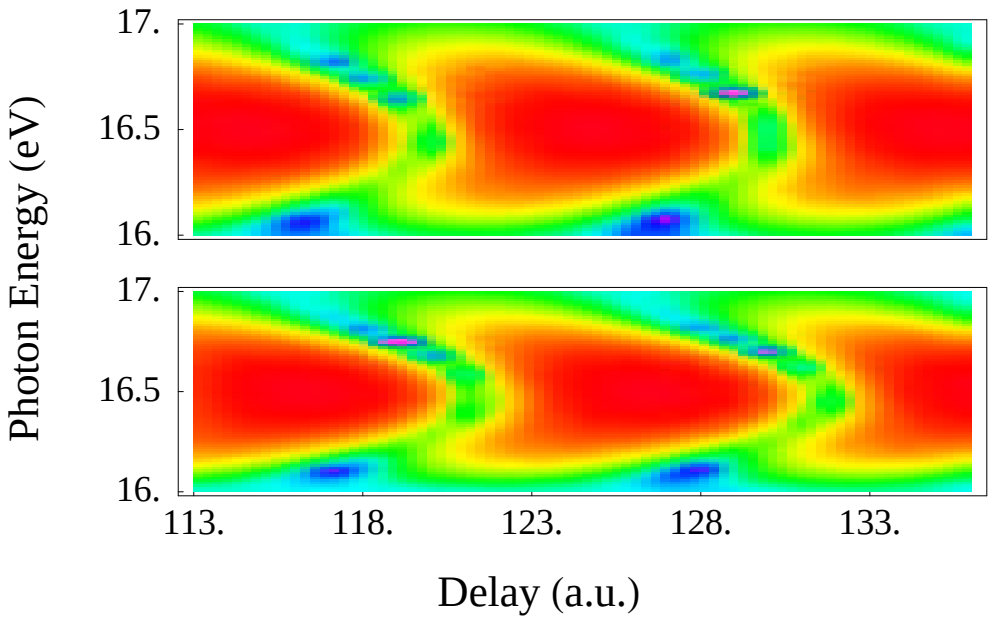

Figure 4.13: As in Fig. 4.12, but now the duration of the fundamental and the harmonic is 20 and 60 cycles respectively. The top figure shows the case of a 11th harmonic pulse having no chirp while for the bottom figure, a gaussian chirp is used. Colors vary from purple to red with increasing intensity.

10%. To subtract the phases we assumed, as in the previous section, a linear modulation frequency. Also in this case the difference of this frequency from the frequency determined by fit is very low ($< 2\%$) and better for the retarded pulses. Following the same procedure for a 20-cycle fundamental pulse, we obtain the phase shown in Fig. 4.17, which resembles the results for the 10-cycle case.

Contrary to the third harmonic case, the subtraction of the reference phase, obtained with a $\phi(\omega) = 0$ pulse, is vital to obtain the complete phase profile of the pulse. Nevertheless the reference phase is smooth and in addition has an almost linear dependence on frequency (equivalently is almost steady within tenths of a rad) for frequencies from 16.5 to 17.2 eV (10 cycle case), which implies that in this range the reference phase is not important. The role of the energy distance from the ionization threshold, in this case practically one fundamental photon, on the harmonic spectra was recently investigated in [35]. The way it affects the reference phase is not clear yet.

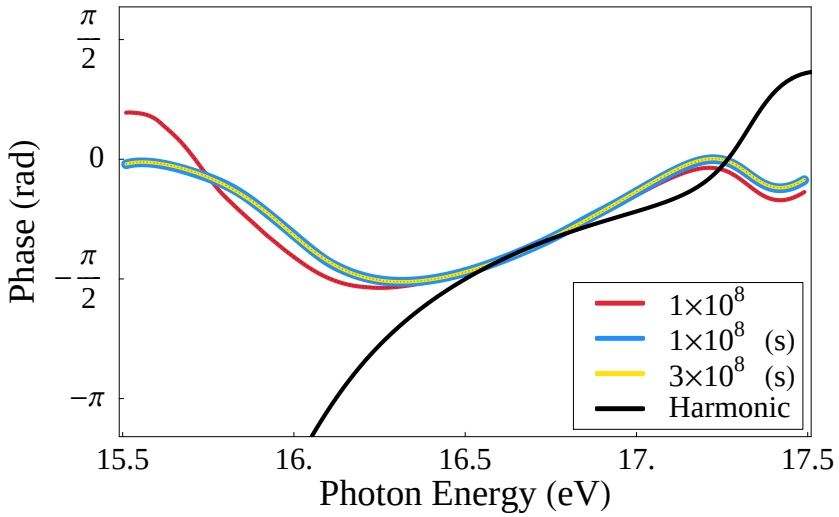

Figure 4.14: The phase measured via the interference of a laser pulse of 2×10^{13} W/cm^2 and $\omega = 1.5$ eV of total duration 10 cycles together with a sin^2 pulse of $\omega = 16.5$ eV duration 10 cycles and intensity as shown in the legend. We also show the phase of the generated harmonic by the fundamental itself. The frequency of the modulation is assumed linear. In all figures (s) means the interference region is shifted by a fundamental cycle after the fundamental maximum.

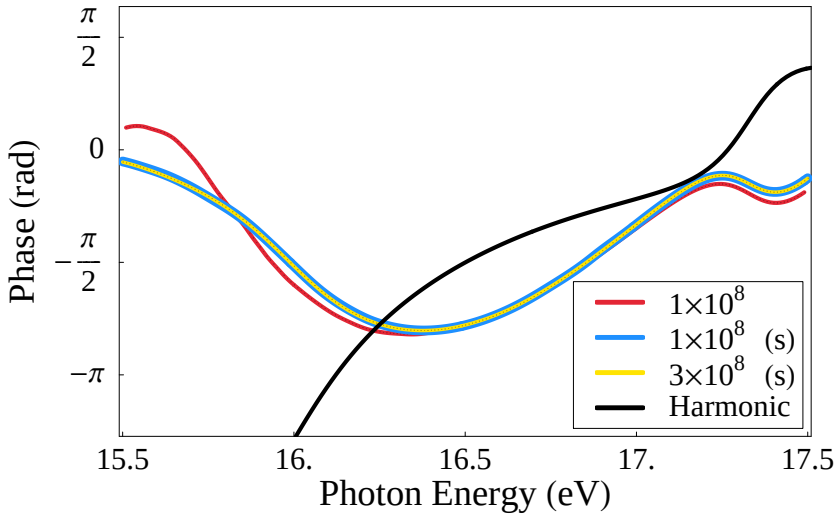

Figure 4.15: Same as Fig. 4.14, but now the 11th harmonic pulse has a gaussian $\phi(\omega)$ as shown in Fig. 4.16.

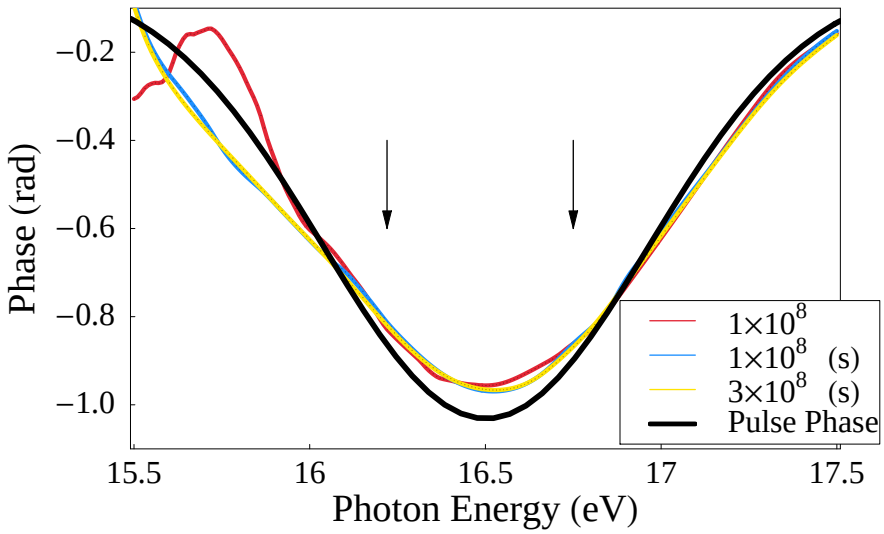

Figure 4.16: The harmonic pulse phase measured by the interference of a 10-cycle laser pulse of 2×10^{13} W/cm^2 and $\omega = 1.5$ eV together with a 30-cycle pulse of $\omega = 16.5$ eV and intensity as shown in the legend, having a gaussian $\phi(\omega)$ dependence as shown. Vertical arrows indicate FWHM of the harmonic pulse.

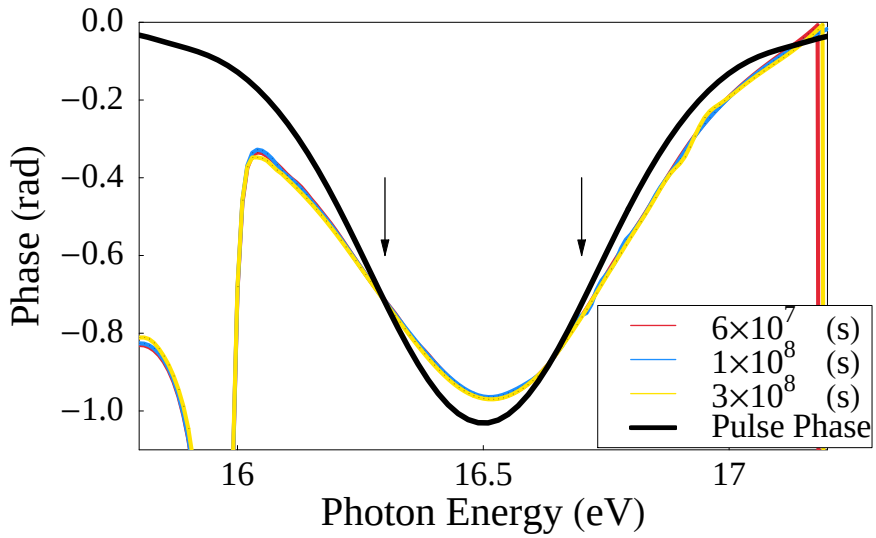

Figure 4.17: Same as in Fig. 4.16, but in this case the duration of the fundamental and the harmonic is 20 and 60 cycles respectively.

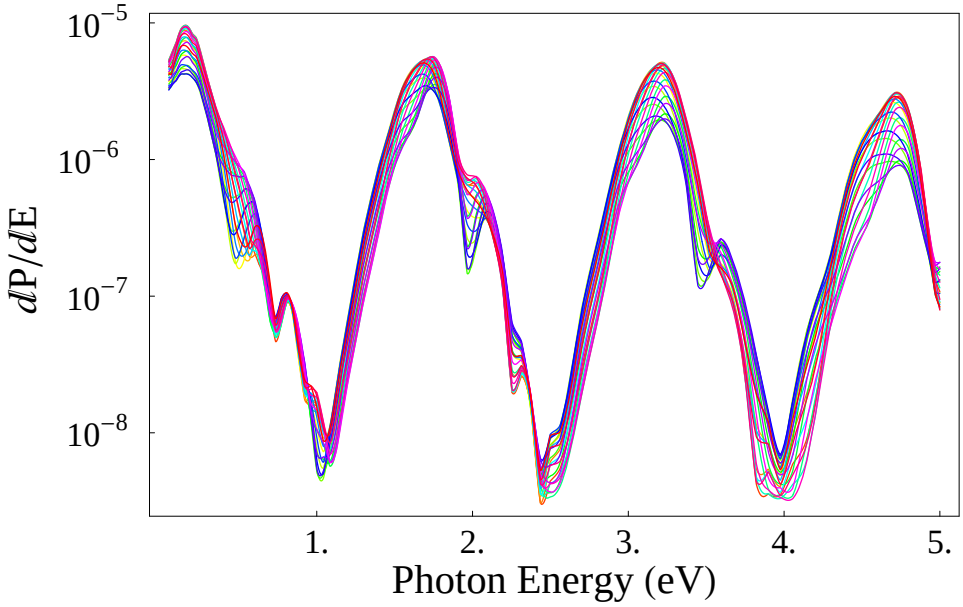

Figure 4.18: The photoelectron spectrum for a laser pulse of 2×10^{13} W/cm^2 and $\omega = 1.5$ and total duration of 20 cycles, together with a eleventh harmonic pulse of intensity 3×10^8 and total duration of 60 cycles. Colors vary from red to blue as the delay between the two pulses increases. The part of the PES spectrum shown corresponds to absorption of $10, 11, 12$ and 13 fundamental photons

PES modulation

The harmonic we consider, is high enough to enable us to look at another aspect of its interference with the fundamental, namely the photoelectron production. An important difference in this approach is that we cannot use information during the ionization process, only the final PES. The harmonic pulse ends before the fundamental pulse, so we look at the results of the interference a few cycles of the fundamental after it is over. The ponderomotive shift is practically due to the fundamental and is $I/(4\omega^2) = 1.3$ eV, so the 11th harmonic produces the peak of the PES centered at 1.7 eV (higher by 0.1 eV due to pulse shape and duration).

In Fig. 4.19 we show a typical PES for the atom subject to a 10-cycle fundamental and the 11th harmonic, together with the difference of the phase of the modulation of the ATI for a harmonic pulse with chirp and the reference phase. The results appear sensitive to the time domain we interfere the two pulses. When the maximum intensities of the two pulses nearly coincide, the pulse phase we obtain is as good as when we rely on the modulation of

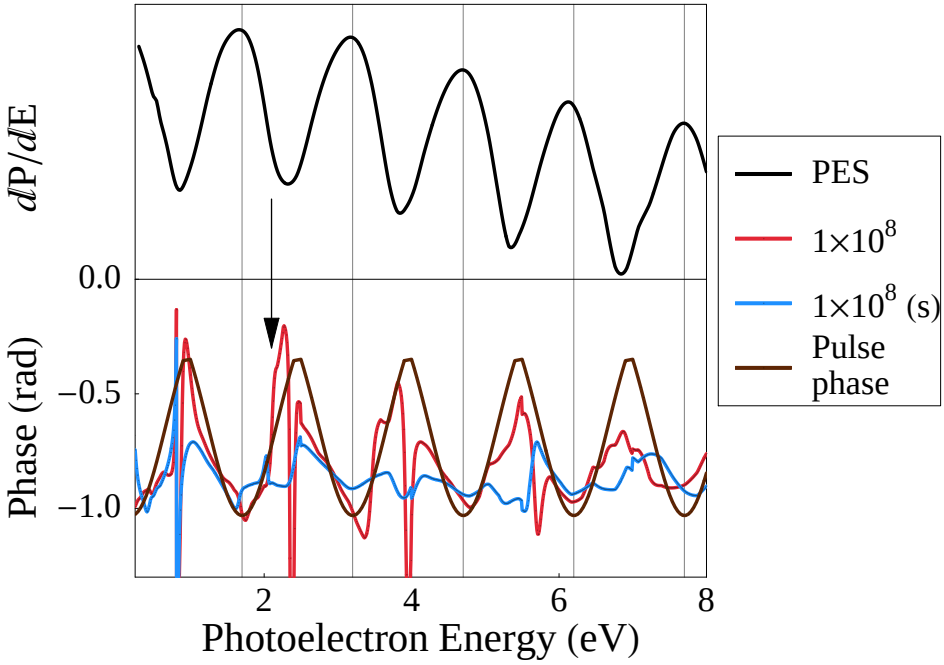

Figure 4.19: We show the PES for a laser pulse of 2×10^{13} W/cm^2 and $\omega = 1.5$ eV of total duration 10 cycles together with a pulse of $\omega = 16.5$ eV duration 30 cycles and intensity as shown in the legend (upper part, logarithmic scale, arbitrary units). The lower part is the reconstructed phase profile of the pulse, together with the actual phase profile. We plot also the phase of the harmonic pulse shifted by n photon energy. In this figure and the following, the vertical lines show the photoelectron energy that corresponds to absorption of 11,12,13 ... photons.

the harmonic signal. This is not the case when the maximum intensity of the harmonic pulse is approximately a fundamental cycle after the maximum intensity of the fundamental.

There is another interesting feature, visualized clearly in Fig. 4.20 where we show the modulation frequency of the PES. The first straight line on the left is the modulation frequency predicted by perturbation theory, and the following lines are displaced by a photon energy. The regions where the modulation frequency is close to the frequency expected by perturbation theory, as can be seen by comparing Figs. 4.20 and 4.19, reproduce better the phase profile of the pulse, so modulation frequency can be used as a

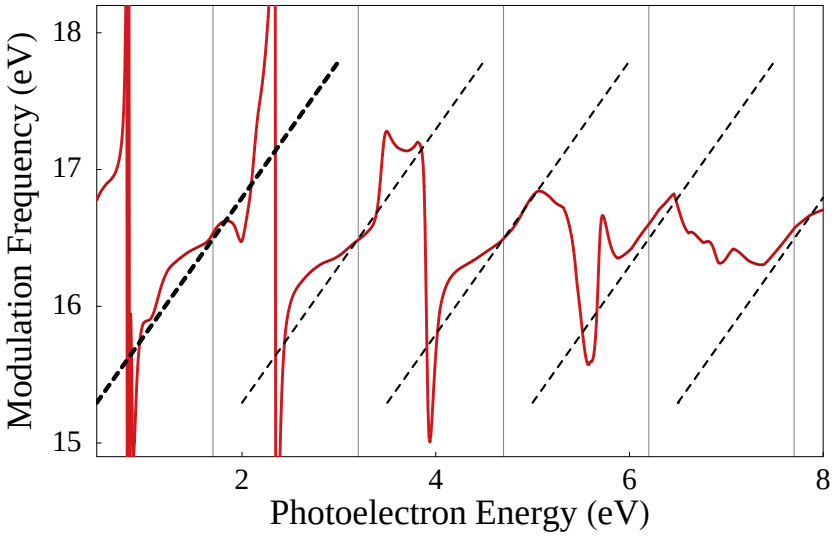

Figure 4.20: With conditions as the above figure, we show frequency determined by the PES modulation, together is the modulation frequency expected by perturbation theory (heavy dashed straight line). The following straight lines have the same slope and are displaced by a photon energy.

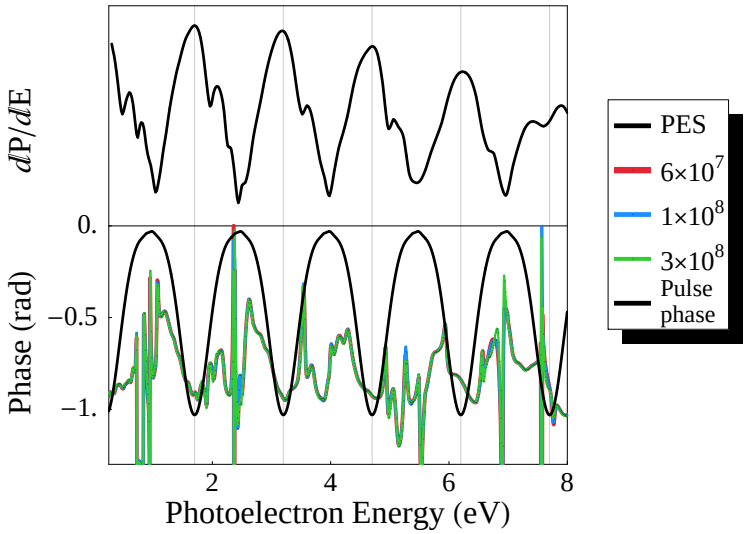

Figure 4.21: Same as in figure 4.19 but now the fundamental and the harmonic have a duration of 20 and 60 cycles respectively. In this case the substructures following the photoelectron peak are visible.

criterion for the quality of the phase. We also examined the case of a 20-cycle fundamental which presents similar features.

Another aspect is the influence of the substructures following the photoelectron peak on the phase profile we obtain. In the case of a 20-cycle pulse, two sub-peaks are visible , with a separation of 0.26 eV, close to the 0.31 eV predicted by the 1D model in [36]. For the 10-cycle case, such substructures are not visible in the PES, but their expected separation of around 0.4 eV, obtained by scaling the separation for the 20-cycle case, is compatible with the energy where the phase begins to differ strongly (indicated by arrow in Fig. 4.19). This appears also in the case of a 20-cycle fundamental, and poses a limit to the extent of the phase profile we can extract, which depends on the characteristics of the fundamental pulse.

4.5.3 Reference phase

From the previous discussion it is clear that the sole limitation is the reference phase. It is not easy to be determined experimentally, since it would require a chirp free harmonic, which is not available at the time. On the other hand, this one-atom study can give some indications on the extent this parameter influences the results, and could point regions (of laser intensity, duration ...) where it can be neglected.

A first step in this direction is to calculate the reference phase for a series of harmonics produced from the same fundamental. For every harmonic we followed the same procedure as in the previous sections. The intensity of the harmonic was chosen to maximize the interference effects employing the same "algorithm" described in the beggining. Also we were careful in the choice of the interference region in space, where we chose the maximum of the produced harmonic to coincide (within few harmonic cycles) with the maximum of the harmonic we used for the interference and the duration of the harmonic pulse. This was done by inspecting the time profile of the produced harmonics, obtained by an inverse Fourier transform of the harmonic signal, as shown in Figure 4.22. For the latter, we use a simple window function to take the part of the spectrum ($\pm$ a photon energy) close to the harmonic we want. The extended tail following the maximum observed in seventh and ninth harmonics is an effect of the bound states in this energy range.

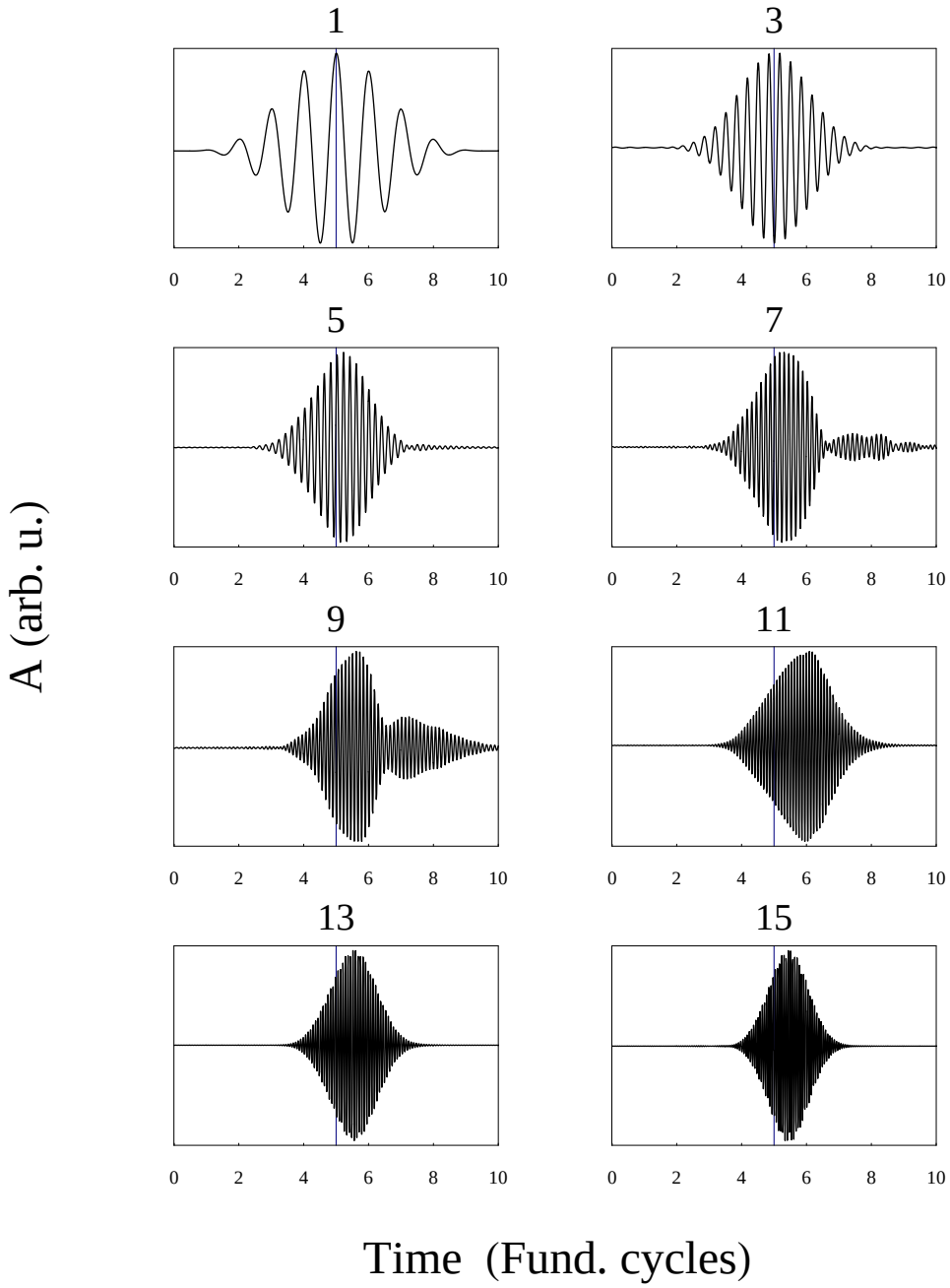

Figure 4.22: Time profile of the emmited harmonics from hydrogen atom radiated by a laser pulse of 2×10^{13} W/cm^2 with $\omega = 1.5$ eV and 10 cycle duration. The label of every plot indicates the harmonic order, the thin vertical line points the maximum intensity of the laser (at $t = 5$ cycles)

For direct comparison, all phase profiles calculated where shifted to be zero at odd multiples off the fundamental frequency, and a linear slope was subtracted to make them as flat as possible, through a subjective algorithm.

We performed this calculations for fundamental intensities of 1×10^{13},2×10^{13},4×10^{13} W/cm^2, photon energy $\omega = 1.5$ eV and total duration 10 cycles. In the case the fundamental intensity was 1×10^{13} W/cm^2, a part of the spectrum was influenced by the bound states of the system, because of the low intensity (namely seventh and ninth harmonics). The rest of the harmonics (third, fifth, eleventh and thirteenth) showed a behaviour resembling the behaviour at higher intensities, with the last two having a relatively high FWHM of about 0.7 eV.

The case of 2×10^{13} W/cm^2 fundamental is presented in Figure 4.23, where we show the reference phase for harmonics observable in this intensity. The seventh and the ninth harmonic again show signs of influence of the bound states of the atom in this region (10 to 14 eV). The lowest harmonics (third and fifth) have a reference phase that is practically constant, with a smooth variation of less than 0.05 of a rad inside the FWHM of the harmonic. The highest harmonics (eleventh, thirteenth and fifteenth) show a phase variation that is smaller for higher orders, starting from about 0.2 rad in the case of the eleventh and ending at about 0.1 rad for the fifteenth (always inside the FWHM).

Another point of view is to look at the modulation frequency, and its relation to the simple linear prediction of the perturbation theory. This has the additional advantage of potentially serving as an independent diagnostic tool for the importance of the reference phase, since it is a direct outcome of an experimental measurement. In Figure 4.24 we show the difference of the modulation frequency of each harmonic to the frequency expected by perturbation theory (ν_p) as a fraction of (ν_p). The seventh and the ninth harmonic, that are close to bound states, show the highest deviation from the simple linear expectations of perturbation theory. As is the case for the reference phase, the situation gets "better" with increasing harmonic order, and for the fifteenth harmonic the modulation frequency is practically identical to the perturbation theory results.

Performing the same study for a higher intensity, 4×10^{13} W/cm^2, we obtain the results summarized in Figures 4.25 and 4.26. The reference phase

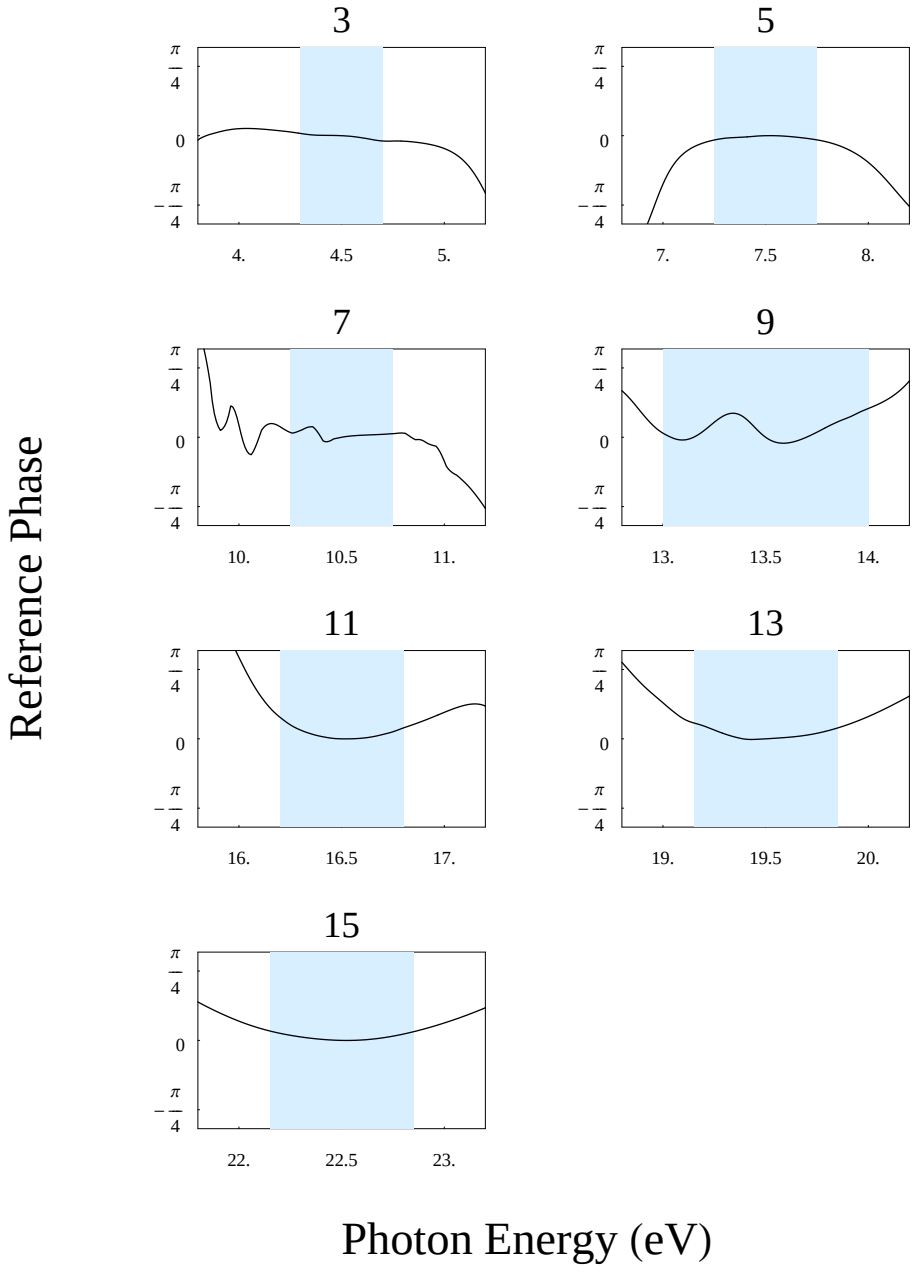

Figure 4.23: The reference phase for harmonic orders three to fifteen produced by a 10-cycle fundamental of 2×10^{13} W/cm^2 and $\omega = 1.5$ eV. The order of the harmonic is shown on the top of each plot. The shaded region marks the full width half maximum of the harmonic intensity.

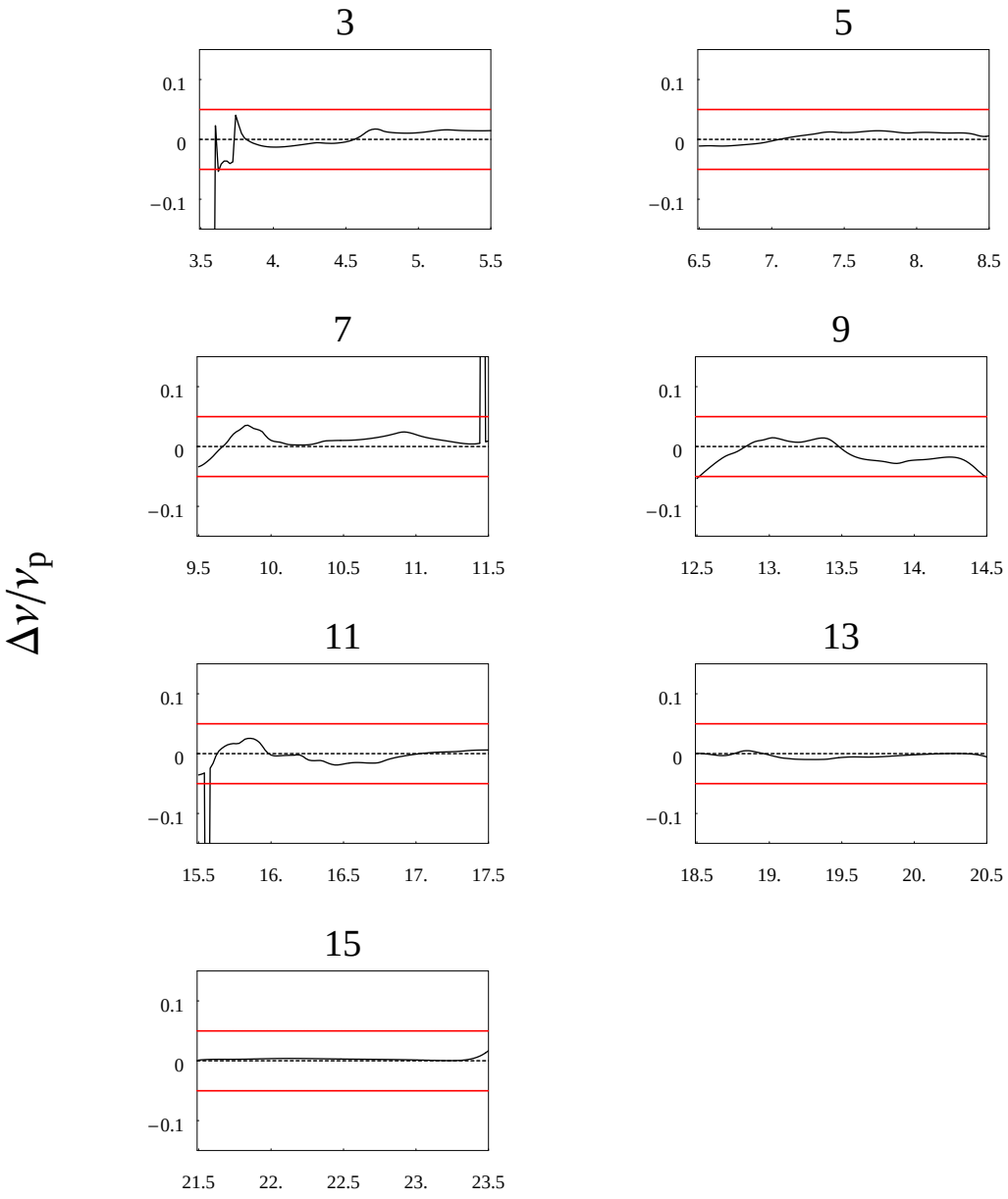

Figure 4.24: For conditions as in figure 4.23 we show the difference of the modulation frequency of the radiation intensity of each harmonic to the frequency expected by perturbation theory (ν_p) over ν_p. The horizontal red lines indicate $\pm 5\%$ difference from ν_p.

appears slightly worst for the lowest harmonics (third anf fifth), but is improved in the case of the seventh, where it fluctuates less than a tenth of a rad, and the ninth. For the eleventh, the phase is constant for an extent bigger than its FWHM. The following harmonics have a fluctuation of at most few tenths of a radian. The modulation frequency indicates some problems for the third harmonic, but for the higher ones is in good agreement with perturbation theory. The highest harmonics, appear to have a high bandwidth, a FWHM increasing from 0.7 (15th) to 1.0 (21st) eV, and their reference phase is not better than the case of lower fundamental intensity (2×10^{13} W/cm^2).

4.6 Conclusions

We have been able ([37]) to retrieve the phase profile of a harmonic through its interference with the fundamental on the harmonic radiation produced, for short pulses (10 and 20 fundamental cycles). We observe a systematic tendency for the phase profile to be flattened in all the cases we examined, the cause of which remains an open question. Nevertheless the discrepancies are small.

In the case of the third harmonic, the phase determined solely by the modulation is very close to the actual phase of the harmonic, without the need for a subtraction of a reference phase, since the later is practically zero.

On the contrary, for the 11th harmonic this is not the case, because the reference phase is not linear with ω, so it is important to be taken into account. If we calculate this reference phase, by interference with a pulse without a chirp, we are able to create the phase profile of the pulse, with good accuracy. An important point for the 11th-harmonic case is that the results of the interference, when the maximum of the harmonic pulse is close to the maximum of the harmonic produced by the fundamental, are found to be better.

We have also used the PES modulation, in the case of the 11th harmonic, and reconstructed the phase using the same procedure. The results appear to be more sensitive and limited by the structure following a PES peak. Nevertheless, the extracted phase profile can be of the same quality with those based on harmonic modulation. Also, an interesting feature is that

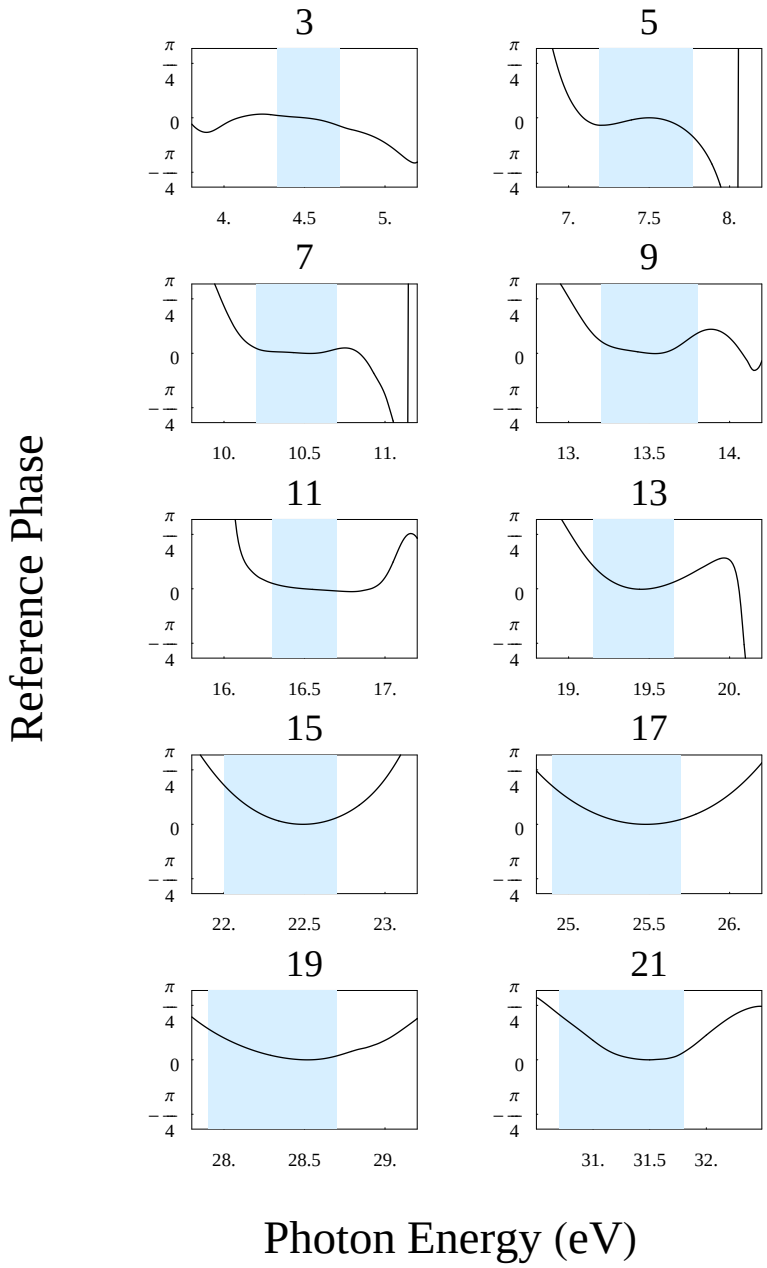

Figure 4.25: The reference phase for harmonic orders three to twenty one produced by a 10-cycle fundamental of 4×10^{13} W/cm^2 and $\omega = 1.5$ eV. The order of the harmonic is shown on the top of each plot. The shaded region marks the full width half maximum of the harmonic intensity.

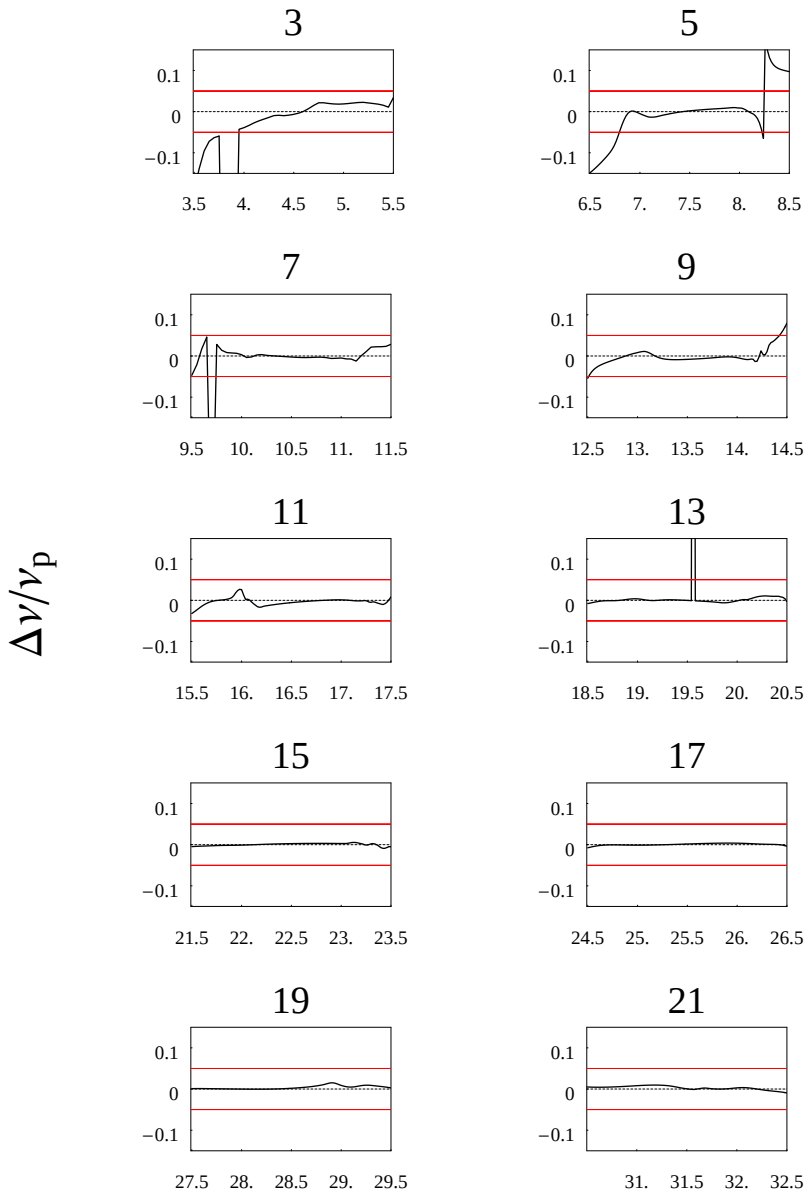

Figure 4.26: For conditions as in figure 4.25 we show the difference of the modulation frequency of the radiation intensity of each harmonic to the frequency expected by perturbation theory (ν_p) over ν_p. The horizontal red lines indicate $\pm 5\%$ difference from ν_p.

phase information is found also in the peaks that follow.

We performed a study of the importance of the reference phase. The results show that the intensity of the fundamental influences the reference phase especially for energies close to bound states. Higher intensities make bound states less important in the dynamics of the atom.

CHAPTER 5

ELECTRON ANGULAR DISTRIBUTIONS IN TWO-PHOTON DOUBLE-IONIZATION OF HELIUM

5.1 Introduction

Although single-photon double ionization can only be direct, requiring correlation in either the initial or the final state (and in reality in both) multiphoton double ionization is considerably more complex. Under most circumstances, it is dominated by sequential single-ejection processes and it is only under special conditions that direct multi-photon double ionization can be identified and studied. After the unequivocal detection of the process by Walker et al. [15], in the strong field long-wavelength multiphoton (high order, non-linear) regime, it is only quite recently that the angular distribution of the emitted electrons was explored by Weber et al. [38, 39] through a novel technique (COLTRIMS). Much insight into the underlying mechanism has been provided by Becker and Faisal [40, 41] who have pointed out the dominant influence on the correlation that is responsible for the behaviour.

Yet, processes in which direct double ejection can be dominant and/or unequivocally separable from the sequential are rare, and to the best of our knowledge at this point it is only in two-photon double ionization of He that a clear signature of double ejection has been identified by Kornberg and Lambropoulos [42] for photon energies around 45 eV. What makes this photon

energy special is the energetically impossible single-photon ionization of the ion, making thus the sequential process of third order, while the direct is one order lower (Figures 5.1,5.2). In addition, the photoelectron energy spectrum is such that all electrons of kinetic energy below 10 eV represent direct double ejection, while the energy peaks corresponding to single-photon ionization of the neutral and two-photon ionization of the ion (sequential) appear at 20.5 eV and 36 eV, respectively; well separated from the direct-double-ejection signal, whose continuous energy spectrum extends from zero to 10 eV (Figures 5.3,5.4). Given that the ionization potential of any neutral two-electron atom is smaller than that of the ion, it is always possible to find a photon energy range in which the above conditions are satisfied. This provides a rather unique context for the study of correlation on the two-photon double ejection, because this process unlike its single-photon counterpart can also take place without any correlation. It can, in fact, do so even in the limit of non-interacting electrons. Taking advantage of recent progress in ab initio quantitative theory of multiphoton double ejection, we have explored the photoelectron angular distribution of the direct two-photon process and it is the purpose of this chapter to report the main features, emphasizing certain somewhat surprising results, such as the tendency of the two electrons to be emitted in the same direction with higher probability when correlation is included than when it is not. The possibility of including correlation to the desired degree is one of the advantages of the approach, which in many ways is complementary to that of Taylor and collaborators [43, 44].

5.2 Atomic basis

Specifically [1] , for the case of helium, we derive the matrix equations resulting from the two-electron Hamiltonian using basis states of the type

$$\Psi_E^{\Lambda}(r_1 r_2) = \sum_{nll',n'}^{N_c,N_s} c_{nll'n'}(E)\Phi_{nln'l'}^{\Lambda}(r_1,r_2) \tag{5.1}$$

where the basis channel wave functions $\Phi_{nln'l'}^{\Lambda}$ are LS-coupled antisymmetrized products of the one-electron target radial function $P_{nl}(r), n = 1, 2, \ldots, N_c$,

[1] The method is presented in more detail in the last part of Chapter 1

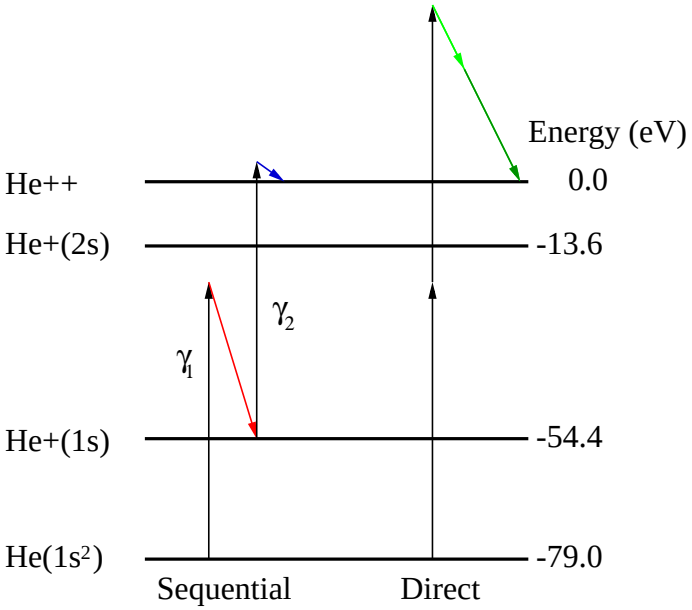

Figure 5.1: (I) Sequential versus Direct double Ionization of He. For photon energies higher than 54.4 eV sequential ionization happens by absorption of $(1+1)$ photons. Direct requires 2 photons.

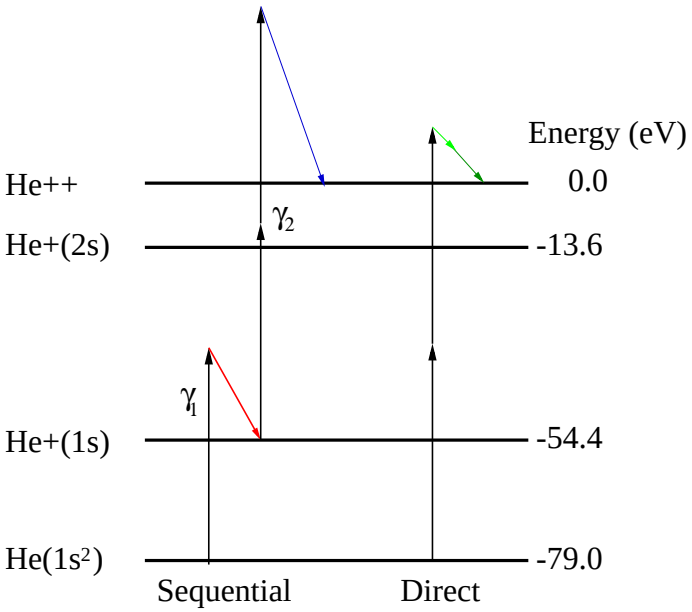

Figure 5.2: (II) Sequential versus Direct double Ionization of He. For photon energies lower than 54.4 eV and higher than 44.5 sequential ionization happens by absorption of $(1+2)$ photons. Direct still requires 2 photons.

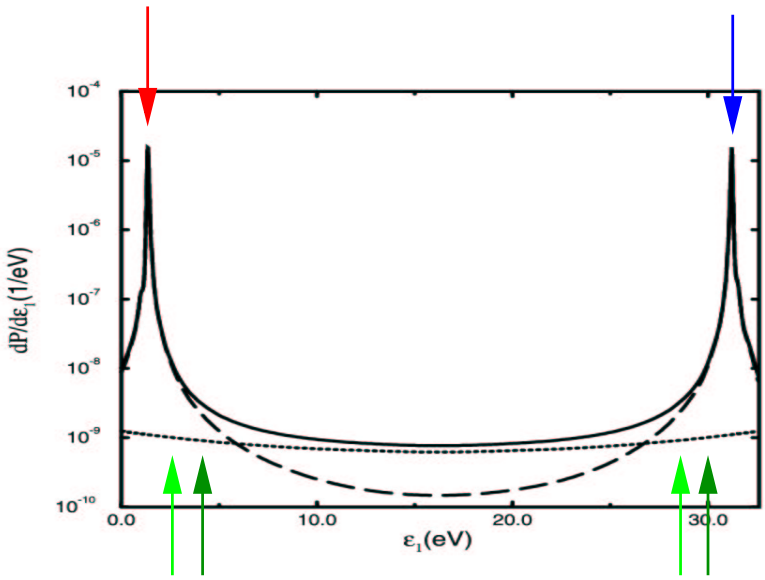

Figure 5.3: The photoelectron energy spectrum of He for the photon energy $\omega = 1.65$ a.u. (55.8 eV). The laser pulse has duration $\tau = 50$ fs and intensity 10^{11} W/cm^2. Broken curve, sequential contribution; dotted curve, direct contribution; full curve, total contribution. Figure taken from [42].

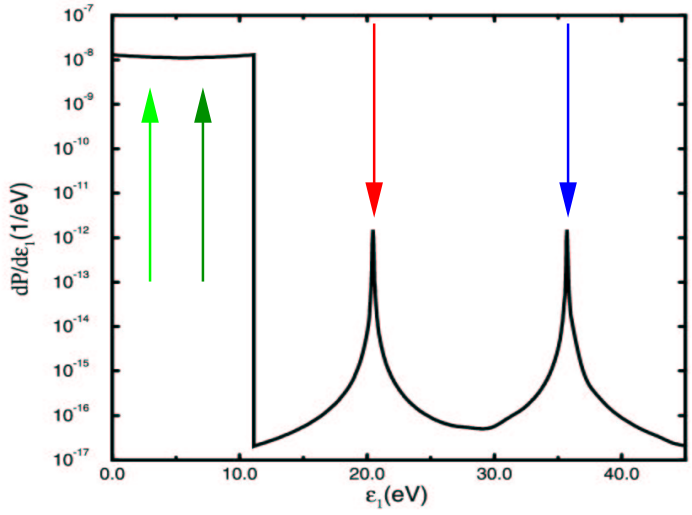

Figure 5.4: The photoelectron energy spectrum of He for the photon energy $\omega = 2.05$ a.u. (44.9 eV). The laser pulse has duration $\tau = 50$ fs and intensity 10^{11} W/cm^2. Below 11 eV the contribution comes from the direct channel, whereas above 11 eV it comes from the sequential channel. Figure taken from [42].

constructed in a spherical box of radius R with vanishing asymptotic conditions at the boundaries and the B-spline functions $B_{n'}(r), n' = 1, 2, \ldots, N_s$ of order k, defined in the region $[0, R]$:

$$\Phi^{\Lambda}_{nln'l'}(r_1, r_2) = A_{12}\frac{P_{nl}}{r_1}\frac{B_{n'}}{r_2}Y_{LM_L}(\hat{r_1}, \hat{r_2}; l, l') \tag{5.2}$$

where A_{12} is the two-electron antisymmetrization operator. Classification of the states through the index n, denotes the discretization of the spectrum of the eigenstates of the core (He^+) ϕ_i and should be understood as characterizing both negative energy states (bound) when $\epsilon_n \to \epsilon < 0$ and positive states (continuum) when $\epsilon_n \to \epsilon > 0$. The two-variable angular function Y_{LM_L} is just the projection of the total angular momentum state $|LM_L\rangle$ onto the independent electron states $|lm, l'm\prime\rangle$ [20].

Expanding now the field-free Hamiltonian of helium H_0 on the basis (2), the variational method transforms the coupled-channel Schrödinger equations of the system to a linear algebraic equation problem [8, 10], with coeficients depending on the energy of the one-electron core states and interchannel coupling potentials (configuration interaction) [20]. For an energy of the whole system E, such that N_o channels are open ($\epsilon_n \leq E, n = 1, 2, \ldots, N_0$), for each channel i, N_0 linearly independent vectors result. Physically, this reflects the N_0 different asymptotic boundary conditions, corresponding to each channel. The discretized channel wave functions we obtain in this procedure are not normalized, thus satisfying arbitrary boundary conditions. Recalling the correct boundary conditions, which continuum channels resulting from a photoionization process should satisfy, allows us to normalize the discrete states of positive energy in order to properly represent the physical states of the system.

The channels $\psi^i_E \equiv |ELSM_LM_S; \epsilon l l'\rangle$ contributing to the final state are characterized by the quantum number of the core target state $(\epsilon; l)$ (electron "1") and the quantum numbers $(\epsilon'; l')$ of the other electron (electron "2"), subject to the relation $\epsilon + \epsilon' = E$, and with $l$and l' restricted by angular and parity addition rules so as to result in a state with L, S angular and spin momentum. We separate single- from double-ejection final states as follows: Final channel states with one-electron core states (He^+) of ϵ negative ($\epsilon < 0$) contribute to single ejection (He^+), while all of the rest ($\epsilon > 0$) contribute to double ejection. With the above in mind, the procedure for calculating

the above formula is the following: We first construct the bound states of the system using fixed boundary conditions (FBC), namely, the two-electron wave functions assumed confined in a spherical box of radius R = 40 a.u. with nodes at the two edges $\psi(0,0) = \psi(0,R) = \psi(R,R) = 0$. For the ground-state energy, we obtain $E_g = 78.467$ eV to be compared with the exact value $E = 79.002$ eV calculated by Pekeris [45]. Next, the multichannel continuum states are calculated with no assumed boundary conditions for the symmetries up to $L < 7$. For this, we allow only channels with $l, l' < 4$ and energies corresponding to the bound and continuum spectrum of He^+.

Having obtained the above two-electron field-free LS-uncoupled states, we are in the position to calculate the corresponding dipole matrix elements between those states. These dipole matrix elements and the energies of the two-electron states are the only dynamical quantities that enter the two-photon cross-section (see the explicit form below).

5.3 Photoelecron angular distributions

The N-photon transition amplitude, in the context of lowest-order perturbation theory, from the initial state $|g\rangle$ to the final continuum $|f\rangle$ is given by

$$\begin{aligned} M_{fg}^{(N)} &= \sum\!\!\!\!\!\!\int_{\nu_1} \cdots \sum\!\!\!\!\!\!\int_{\nu_{N-1}} \frac{\langle f|\mathbf{D}\hat{\mathbf{e}}|\nu_{N-1}\rangle \cdots \langle \nu_1|\mathbf{D}\hat{\mathbf{e}}|g\rangle}{\Delta\omega(\nu)}, \\ \Delta\omega(\nu) &= [\omega_g + (N-1)\omega - \omega_{\nu_{(N-1)}}] \cdots [\omega_g + \omega - \omega_{\nu_1}]. \end{aligned} \tag{5.3}$$

The two-electron continuum final state in an LS-coupling scheme is expressed as [20]

$$|\mathbf{k}, m_s; \mathbf{k}', m_s'\rangle = \sum_{\Lambda} \sum_{lm} \sum_{l'm'} i^{l+l'} e^{-i\delta_l - i\delta_{l'}} Y_{lm}^{\star}(\hat{k}) Y_{l'm'}^{\star}(\hat{k}') C_{LM_L} |\Lambda; \epsilon l l'\rangle, \tag{5.4}$$

where C_{LM}, C_{SM_S} (Glebsch-Gordan coefficients) project the total orbital and spin angular momenta $|LM\rangle$,$|SM_S\rangle$ onto the independent electron states $|lmm_s; l'm'm_s'\rangle$. The channel functions $|\Lambda; \epsilon l l'\rangle$ should be understood as $|E\Lambda; \epsilon l l'\rangle \equiv |ELSM_LM_S; \epsilon l l'\rangle$. The sum over$\Lambda$ should be understood as the sum over the angular quantum numbers LM_LSM_S. The long-range phase shifts for a Coulomb potential with $z = 2$ are given by $\delta_l = arg[\Gamma(l + 1 +$

$i/\sqrt{2\epsilon})]$. It should be emphasized, however, that the final state employed in the calculation is correlated and not a product of two Coulomb functions. The above equations lead to a two-photon cross-section of the form

$$\frac{d\hat{\sigma}_2^{++}(E)}{d\epsilon d\Omega d\Omega_{k'}} = 2\pi(2\pi\alpha)^2\omega^2 \left| M^{(2)}(\hat{k},\hat{k}') \right|^2, \tag{5.5}$$

with

$$M^{(2)}(\hat{k};\hat{k}') = \sum_{\Lambda;lm,l'm'} i^{l+l'} e^{-i\delta_l - i\delta_l'} C_{LM_L} Y^{\star}_{lm}(\hat{k})\, Y^{\star}_{l'm'}(\hat{k}') D^{(2)}(\Lambda;\epsilon l l'). \tag{5.6}$$

For a two-photon transition, starting from the ground state of He, the only final states allowed are those with $L = 0, 2$ and assuming the light to be linearly polarized, only states with $M_L = 0, L = 0, 2$ need be considered:

5.4 Results and discussion

First, we would like to point out some important differences from the case of single-photon double ejection.

Single-photon double ejection is impossible without any correlation between the two electrons. Electron-electron interaction (or correlation) must be included either in the ground or in the final state, and strictly speaking in both. This is in contrast to the two-photon (or multiphoton, more generally) case where interaction between the two electrons is not necessary for double election to be possible. One of the electrons can, in that case, interact with the field independently of the other, with the two-photon amplitude factoring into a product of two amplitudes; provided of course the sum of the energies of the two photons is suficient to eject two electrons. But for interacting electrons and hence correlation, the two-photon process presents a rich structure, since in addition to the initial and final state, we have the virtual intermediate states whose correlation can be as important. We should further note that, in the two-photon double ejection, we can have equivalent electrons $(\epsilon l \epsilon' l'; s^2, p^2, d^2)$ in the final state while for single photon we have $(\epsilon l \epsilon' l'; l \neq l')$. This feature, especially when the two electrons share the excess energy almost equally, makes their interaction more significant, since the angular correlation in that case is stronger compared to that of non-equivalent configurations.

In the case of equal energy sharing between the two electrons, Maulbetcsh and Briggs [46] have pointed out that from symmetry reasons of the final state ($^1P^o$), the transition amplitude ($M^{(1)}(\mathbf{k};-\mathbf{k})$) of the single-photon absorption when the electrons have opposite directions vanishes (selection rule C in the review by Briggs and Schmidt) [47]. In the two-photon process, however, where the symmetry of the final state is S and D (within dipole approximation as in our case) the previous conclusion is no longer true. This can be seen from the following argument: From inversion symmetry the two-photon transition amplitude is (eq. (6)) $M^{(2)} = (\mathbf{k}_1, \mathbf{k}_2) = (-1)^{P_i}(-1)^{P_f} M^{(2)}(-\mathbf{k}_1, -\mathbf{k}_2)$, with P_i, P_f the parities of the initial and final symmetry, respectively. Therefore, since $P_i = P_f$ and for $\mathbf{k}_1 = -\mathbf{k}_2$, we see that, in principle, from symmetry reasons there is no vanishing probability for the two electrons to leave the core in opposite directions. We should also note that it is not the multiphoton nature of the process that makes this difference, but basic symmetry requirements of the final wave function. Thus, in coincidence experiments with more than one photon, it is possible to distinguish an even or odd process (in number of photons) by exploiting this simple basic principle.

Our approach enables us to include in the final state as many partial waves as desired, investigating thus the role of correlation. For example, keeping only the p^2 component of the final state gives the shape (but not the magnitude) corresponding to non-interacting electrons. In Figures 5.5 and 5.6, keeping fixed the emission angle of one electron ($\theta = 0^o$) parallel to the polarization axis of the laser, we plot the angular distribution dependence of the second one (θ') on the relative energy sharing, using two different total energies corresponding to photon energy of 44.3 and 44.9 eV. In those figures we see that there is a clear tendency of the two electrons to eject in the same direction, around the angle $\theta_{12} \equiv \theta' - \theta = 0$ when sharing almost equal energy. When the two electrons have a rather large difference in energy (a) it is as if one of the electrons absorbed all of the two-photon energy and then, making a "soft" collision with the electron in the core, caused it to escape (shake-off mechanism). In this case configurations of the type "$sd + pf + \ldots$" are expected to dominate in the angular distribution leading thus to significant probability for angles other than the preferred angles $\theta_{12} = 0, \pi$. In both figures a lobe is apparent at about $\theta_{12} = 135^o$ characteristic of configurations with angular momentum larger than one. For almost equal energy sharing

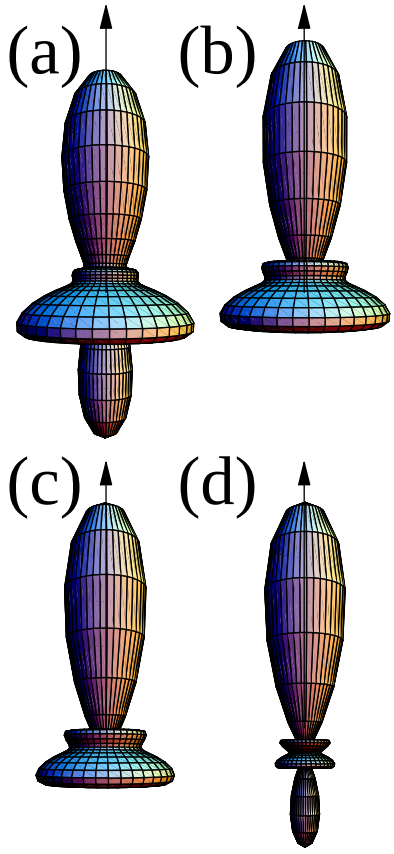

Figure 5.5: Angular distribution of the second electron assuming the first was emmited at $\theta = 0$, as pointed by the arrow, coinciding with the polarization of the laser. The plot is in spherical coordinates, i.e the probability to find the electron as a function of θ' and ϕ'. For these plots: photon energy is $\omega = 44.9$ eV and energy shared as: (a) $\epsilon = 9.52$ eV, $\epsilon' = 1.63$ eV, (b) $\epsilon = 7.89$ eV, $\epsilon' = 3.26$ eV, (c) $\epsilon = 7.34$ eV, $\epsilon' = 3.81$ eV, (d) $\epsilon = 5.71$ eV, $\epsilon' = 5.44$ eV.

(d), it appears that p^2 (predominantly) configurations contribute more significantly overwhelming the influence of $''sd + pf \ldots''$ configurations, thus giving an angular distribution which has a maximum at value $\theta_{12} = 0^o$ and small probability for the two electrons to eject in opposite directions. The lobes at relative angle $\theta_{12} = 135^o$ now have smaller relative amplitude than the lobe in $\theta_{12} = 0^o$.

Assume for the moment that each of the electrons interacts with the field (absorbing one photon) independently of each other and then evolves in time. Then, the two electrons would tend to leave with equal probability in

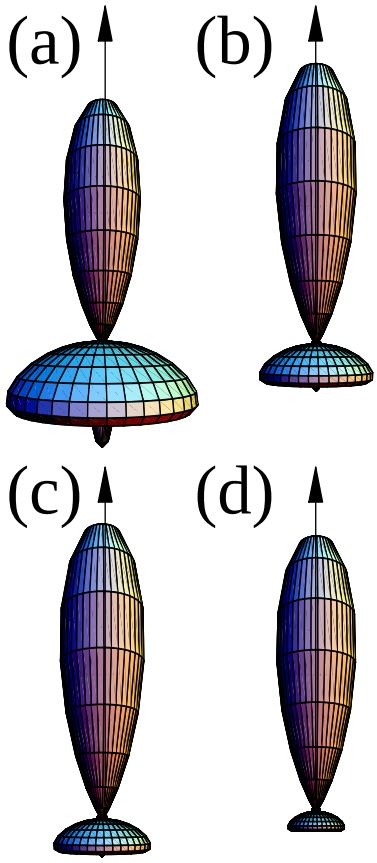

Figure 5.6: Same as in Figure 5.5 but with photon energy $\omega = 44.3$ eV and energy sharing as: (a) $\epsilon = 8.02$ eV, $\epsilon' = 2.17$ eV, (b) $\epsilon = 6.93$ eV, $\epsilon' = 3.26$ eV, (c) $\epsilon = 6.39$ eV, $\epsilon' = 3.81$ eV, (d) $\epsilon = 5.30$ eV, $\epsilon' = 4.90$ eV.

the same or in opposite directions depending on the time elapsed between the consecutive absorptions and the field period. As explained above, this process is not possible for 45 eV. We must then include the Coulomb interactions between the electrons, which will of course modify the angular distribution leading to a pattern very different from that imposed by the field alone. For a qualitative feeling, we plot (in Figure 5.7) the angular distribution resulting when retaining only $l, l' = 1$ (eq. (8)) contribution, next to the complete one:

$$P^{(2)}(l=1,l'=1) = \frac{3}{64\pi^2}\Big|2\cos\theta\cos\theta'[D^{(2)}(0,1,1) - \sqrt{10}D^{(2)}(2,1,1)] + [2D^{(2)}(0,1,1) + \sqrt{10}D^{(2)}(2,1,1)]\cos(\phi-\phi')\sin\theta\sin\theta'\Big|^2$$

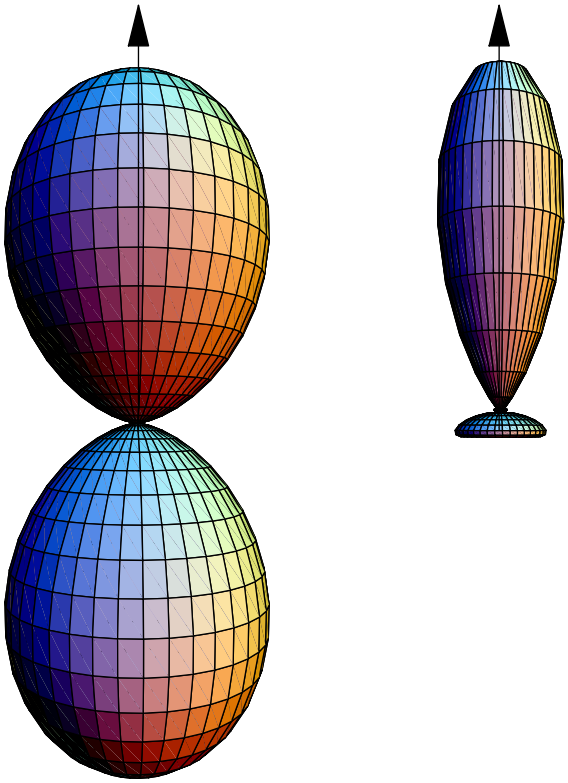

Figure 5.7: For photon energy $\omega = 44.9$ eV we have plotted the p^2 part (left plot) of the angular distribution (retaining contributions $l, l' = 1$) and the complete result (right plot). The left plot does not depend on energy sharing (in shape). For the right plot: $\epsilon = 5.30$ eV, $\epsilon' = 4.90$ eV.

From eq. (8) we see that fixing (θ', ϕ') corresponds to a "$p - lobe$" whose orientation in space depends on E, ϵ, and does not distinguish parallel from anti-parallel trajectories since it is invariant under $(\theta, \phi) \rightarrow (\pi - \theta, \pi + \theta)$, which is not the case for the PAD including all possible channels. This shape of PAD is independent of the energy sharing between the electrons and only its relative magnitude changes.

Next we show the dependence of the total ejection probability (see Figure. 5.8) of the second electron assuming the first to be emitted at $(\theta, \phi = 0)$. Note that this is not restrictive since the PAD depends only on $|\phi - \phi'|$ which is symmetric under both simultaneous rotation of both electrons around the

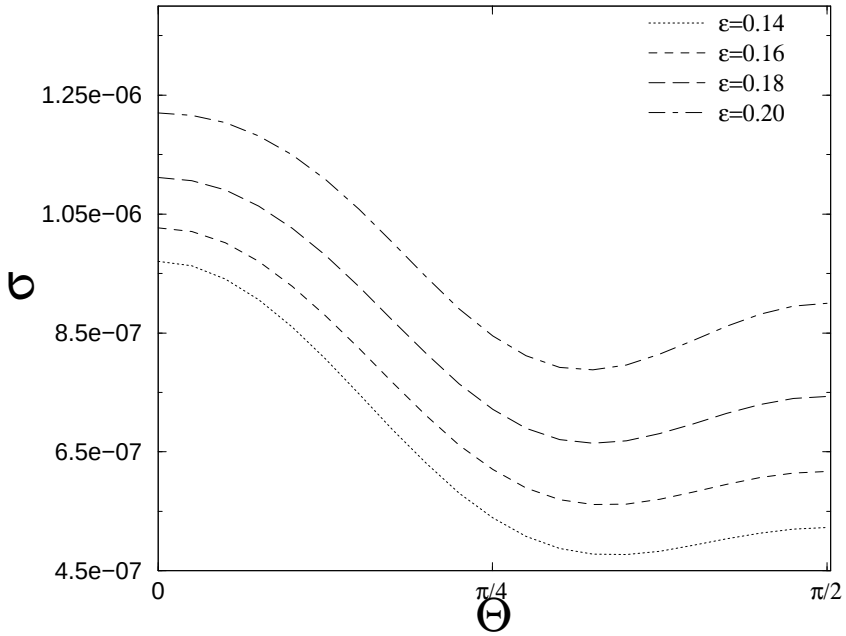

Figure 5.8: Total cross-section for the ejection of two electrons as a function of the angle θ' of one of them, for different energy sharing ($\epsilon + \epsilon' = E$) and photon energy $\omega = 44.9eV$.

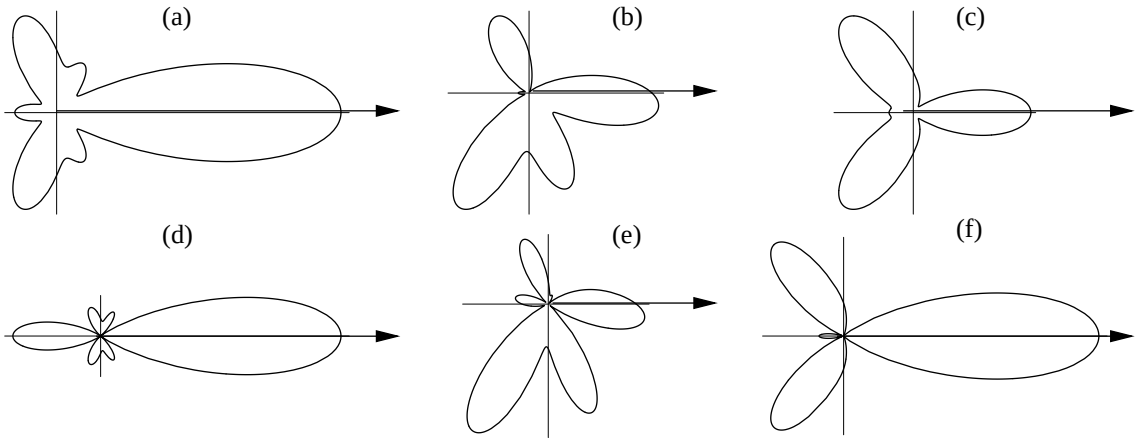

Figure 5.9: For total energy of the system 44.9 a.u. we plot the PAD as a function of $\theta' - \theta$ in the coplanar case ($\Delta\phi = 0$) and different energy sharing (first row $\epsilon = 3.26$ eV and second row $\epsilon = 5.44$ eV) and $\theta' = 0$ (a, d),$\pi/4$ (b, e),$\pi/2$ (c, f).

polarization axis and reflection from the plane defined by the polarization axis and the direction of one electron. The shape of the total ejection probability as a function of θ' is obtained by the integral

$$P(\theta') \sim \int_0^{\pi} \int_0^{2\pi} P(\theta', 0, \theta, \phi) \sin^2 \theta d\theta d\phi \tag{5.7}$$

In the last Figure (Fig. 5.9), we show the PAD for photon energy 44.9 eV as a function of $(\theta' - \theta)$ in the coplanar case ($\Delta\phi = 0$) for various energy sharing between the electrons. The angles presented are $\theta' = 0$ (a, d),$\theta' = \frac{\pi}{4}$ (b, e), $\theta' = \frac{\pi}{2}$ (c, f), while the first and the second row correspond to energies of one of the electrons $\epsilon = 3.26$ eV and $\epsilon = 5.44$ eV, respectively.

5.5 Conclusions

In summary, we have produced detailed results for photoelectron angular distributions of two-photon double ionization of helium at photon energies for which the direct process is easily distinguishable from the sequential one [48]. Exploring the influence of correlation on the form of the distribution, we have shown that the effect is most pronounced when the ejected electrons share the available energy nearly equally. The explanation has to do with the fact that, in that case, the electrons communicate more than when one is ejected with most of the energy, while the other is "left behind". We have also shown explicitly that, by turning correlation on, the electrons tend to be emitted more in the same direction instead of equally in the opposite direction, as would be the case for non-interacting, or weakly correlated particles. This tendency has been noted also by Taylor [49], in the data of Weber et al. [38, 39], as well as in the theory of Becker and Faisal [40, 41]. Whether the physical interpretation of the effect at different ranges of photon frequency and radiation intensity is exactly the same, in our opinion, remains an interesting question. The effects found in this paper for helium should be readily present in almost any atom, and particularly two valence-electron atoms, at much longer wavelength. For helium, the necessary intensity for photon frequencies around 40 to 45 eV is not available at synchrotrons. It is possible that further improvement of high-order harmonic sources might approach that intensity, namely, something like $10^{12} W/cm^2$. On the other hand, the

upcoming FEL-based short-wavelength sources, in their first phase, appear to be well suited for the observation of two-photon double ionization of He.

Bibliography

[1] *A Practical Guide to Splines*, Carl de Boor (Springer - Verlag, New York, 1978).

[2] *Use of boundary-condition wavefunctions for bound states, continuum states, and resonances*, Bruce W. Shore, J. Phys. B **7**, 2502 (1974).

[3] *Use of B-splines in theoretical atomic physics.*, J. Sapirstein and W.R. Johnson, J. Phys. B **29**, 5213 (1996).

[4] in *Many-body theory of Atomic Structure*, T.N. Chang (World Scientific, Singapore, 1993), Chap. B-spline based Configuration-Interaction Approach for Photoionization of Two-electron and Divalent Atoms.

[5] *Non-perturbative time-dependent theory and ATI in two-electron atoms*, Jian Zhang and P. Lambropoulos, J. Phys. B **28**, L101 (1995).

[6] *Nonperturbative time-dependent theory of two-electron atoms in in strong laser fields*, Jian Zhang and P. Lambropoulos, J. of Nonlinear Opt. & Materials **4**, 633 (1995).

[7] *Time-Dependent Calculation of Photoelectron Spectra in Mg Involving Multiple Continua.*, Jian Zhang and P. Lambropoulos, Phys. Rev. Lett. **77**, 2186 (1996).

[8] *Non-variatonal, spline-Galerkin calculations of resonance positions widths and photodetachment cross sections for H^- and He*, Tomas Brage and Charlotte Froese Fischer and Gregory Miecznick, J. Phys. B **25**, 5289 (1992).

[9] *The use of basis splines and non-orthogonal orbitals in R-matrix calculations: application to Li photoionization*, Oleg Zatsarinny and Charlotte Froese Fischer, J. Phys. B **33**, 313 (2000).

[10] *Two-Electron Atoms in Strong Fields*, P. Lambropoulos and P. Maragakis and Jian Zhang, Physics Report **305**, 203 (1998).

[11] A. Macias and F. Martin and A. Riera and M. Yarez, Int. J. Quantum Chem. **33**, 279 (1988).

[12] *Extrapolation method for the evaluation of above threshold ionization cross sections for the one- and two-electron systems*, E. Cormier and P. Lambropoulos, J. Phys. B **28**, 5043 (1995).

[13] *Free-Free Transitions Following Six-Photon Ionization of Xenon Atoms*, P. Agostini and F. Fabre and G. Mainfray and G. Petite and N. K. Rahman, Phys. Rev. Lett. **42**, 1127 (1979).

[14] P. Salieres and A. L'Huillier and P. Antoine and M. Lewenstein, Adv. At. Mol. Opt. Phys. **41**, 83 (1999).

[15] *Precision Measurement of Strong Field Double Ionization of Helium*, Barry Walker and B. Sheehy and L. F. DiMauro, Phys. Rev. Lett. **73**, 1227 (1994).

[16] M. Goeppert-Mayer, Ann. Phys. (N.Y.) **9**, 273 (1931).

[17] *Optimal gauge and gauge invariance in non-perturbative time-dependent calculation of above-threshold ionization*, E. Cormier and P. Lambropoulos, J. Phys. B **29**, 1667 (1996).

[18] in *Time-Dependent Studies of Multiphoton Processes*, , Kenneth C. Kulander, Kenneth J. Schafer, and Jeffrey L. Krauseedited by M.Gavrila (Academic Press, Inc, ADDRESS, 1992).

[19] *Negative Hydrogen in intense laser fields*, L. A.A. Nikolopoulos, Ph.D. thesis, U. of Crete, 1999.

[20] *Multichannel theory of two-photon single and double ionization of Helium*, L. A. A. Nikolopoulos and P. Lambropoulos, J. Phys. B **34**, 545 (2001).

[21] *Qunatum defect theory*, M J Seaton, Rep. Prog. Phys. **46**, 167 (1983).

[22] *Two-photon ionisation of atomic hydrogen in the presence of one-photon ionisation*, M Aymar and M Crance, J. Phys. B **13**, L287 (1980).

[23] *Multiphoton autoionization under strong laser radiation: Three-photon autoionization of strontium as a test case*, Young Soon Kim and P. Lambropoulos, Phys. Rev. A **29**, 3159 (1984).

[24] *Multichannel Rydberg spectroscopy of complex atoms*, Mireille Aymar and Chris H. Greene and Eliane Luc-Koenig, Rev. Mod. Phys. **68**, 1015 (1996).

[25] *Multiphoton ionization of hydrogen: A time-dependent theory*, Kenneth C. Kulander, Phys. Rev. A **35**, R445 (1987).

[26] *Calculation of photoemission from atoms subject to intense lase fields*, Jeffrey L. Krause and Kenneth J. Schafer and and Kenneth C. Kulander, Phys. Rev. A **45**, 4998 (1992).

[27] *Above-threshold ionization spectrum of hydrogen using B-spline functions*, E. Cormier and P. Lambropoulos, J. Phys. B **30**, 77 (1997).

[28] *Time-dependent calculation of ionization in potassium at midinfrared wavelengths*, P. Maragakis and E. Cormier and P. Lambropoulos, Phys. Rev. A **60**, 4718 (1999).

[29] *The time evolution of the hydrogen wavefunction in intense laser fields*, P.L. DeVries, Comp. Phys. Comm. **63**, 95 (1991).

[30] *Energy analysis of time-dependent wave functions: Application to above-threshold ionization*, K. J. Schafer and K. C. Kulander, Phys. Rev. A **42**, 5794 (1990).

[31] *Probing attosecond pulse trains using "phase-control" techniques*, E. Hertz and N. A. Papadogiannis and G. Nersisyan and C. Kalpouzos and T. Halfmann and D. Charalambidis and G. D. Tsakiris, Phys. Rev. A **64**, 051801 (2001).

[32] *Effect of a strong dressing field on the polarizability of atomic helium at harmonic frequencies*, E. Cormier and P. Lambropoulos, J. Phys. B **30**, 3095 (1997).

[33] *Non-perturbative theory of harmonic generation under a high-intensity laser field*, Huale Xu, Zeitscrift für Physic D **28**, 27 (1993).

[34] *Coherent control of extreme uv absorption and photoemission by the simultaneous irradiation of ultrashort extreme uv and laser pulses*, Kenichi Ishikawa and Katsumi Midorikawa, Phys. Rev. A **65**, 031403 (2002).

[35] *Threshold-related effects in high-order harmonic generation*, Bogdan Borca and Anthony F. Starace and A. V. Flegel and M. V. Frolov and N. L. Manakov, Phys. Rev. A **65**, 051402 (2002).

[36] *Multiphoton ionization from a short-range potential by short-pulse lasers*, J.N. Bardsley and A. Szöke and M. J. Comella, J. Phys. B **21**, 3899 (1988).

[37] *Theory of phase characterization of harmonics through interference with the fundamental*, M.G. Makris and L.A.A. Nikolopoulos and P. Lambropoulos, Phys. Rev. A **66**, 053414 (2002).

[38] *Recoil-Ion Momentum Distribution for Single and Double Ionization of Helium in Strong Laser Fields*, Th. Weber and M. Weckenbrock and A. Staudte and L. Spielberger and O. Jagutzki and V. Mergel and F. Afaneh and G. Urbasch and M. Vollmer and H. Giessen and R. Dorner, Phys. Rev. Lett. **84**, 443 (2000).

[39] *Correlated Electron Emission in Multiphoton Double Ionization*, Th. Weber and H. Giessen and M. Weckenbrock and G. Urbasch and A. Staudte and L. Spielberger and O. Jagutzki and V. Mergel and M. Vollmer and R. Dorner, Nature **405**, 6787 (2000).

[40] *Interplay of electron correlation and intense field dynamics in the double ionization of helium*, A. Becker and F. H. M. Faisal, Phys. Rev. A **59**, R1742 (1999).

[41] *Interpretation of Momentum Distribution of Recoil Ions from Laser Induced Nonsequential Double Ionization*, A. Becker and F. H. M. Faisal, Phys. Rev. Lett. **84**, 3546 (2000).

[42] *Photoelectron energy spectrum in 'direct' two-photon double ionization of helium*, M. A. Kornberg and P. Lambropoulos, J. Phys. B **32**, L603 (1999).

[43] *Intense-field multiphoton ionization of a two-electron atom*, Jonathan Parker and K. T. Taylor and Charles W. Clark and Sayoko Blodgett-Ford, J. Phys. B **29**, L33 (1996).

[44] *Double ionization of helium at 390 nm*, Jonathan S. Parker and L. R. Moore and Daniel Dundas and K. T. Taylor, J. Phys. B **33**, L691 (2000).

[45] $1.^1S, 2.^1S$ *and* $2.^3S$ *state of* H^- *and of He*, C.L. Pekeris, Phys. Rev. **126**, 1470 (1962).

[46] *The angular distribution of equal-energy sharing following double photoionization*, F. Maulbetsch and J. S. Briggs, J. Phys. B **26**, L647 (1993).

[47] *Differential cross sections for photo-double-ionization of the helium atom*, J. S. Briggs and V. Schmidt, J. Phys. B **33**, R1 (2000).

[48] *Electron angular distributions in two-photon double ionization of Helium*, M. G. Makris and L. A. A. Nikolopoulos and P. Lambropoulos, Europhys. Lett. **54**, 722 (2001).

[49] Taylor K. T., private communication (unpublished).